Lviv Polytechnic National University

RADIATION-RESISTANT HALL MAGNETIC FIELD SENSORS AND INSTRUMENTATIONS

Inessa Bolshakova
Roman Holyaka
Tetyana Marusenkova
Fedir Shurygin

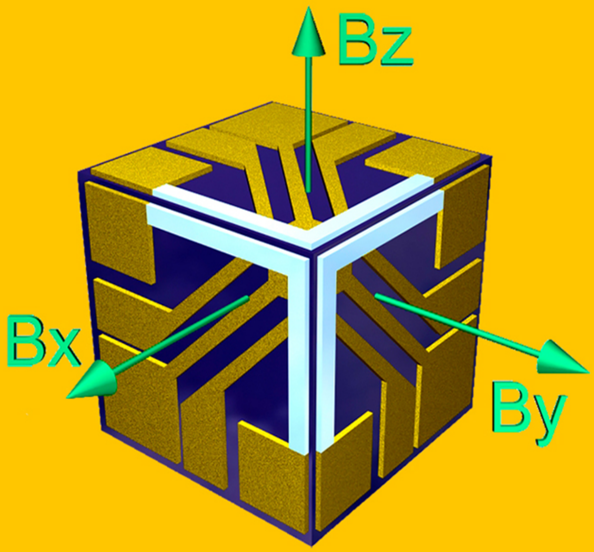

2022

Primedia eLaunch

Lviv Polytechnic National University
Institute of Telecommunications, Radioelectronics
and Electronic Engineering

Inessa Bolshakova
Roman Holyaka
Tetyana Marusenkova
Fedir Shurygin

RADIATION-RESISTANT HALL MAGNETIC FIELD SENSORS AND INSTRUMENTATIONS

Monograph

Dallas, USA
Primedia eLaunch LLC
2022

UDC 62-9:539.16
B 74

Reviewers:

Bohdan Pavlyk,
D.Sc., Prof., Head of the Department of Sensory and semiconductor electronics Faculty
of Electronics and Computer Technologies of the
Ivan Franko National University of Lviv, Ukraine

Yurii Romanyshyn,
D.Sc., Prof., Head of the Department of Electronic Devices
information and computer technologies of Institute of Telecommunications,
Radioelectronics and Electronic Engineering of the
Lviv Polytechnic National University, Ukraine

B 74 **Bolshakova I., Holyaka R., Marusenkova T. & Shurygin F.** Radiation-resistant Hall Magnetic Field Sensors and Instrumentations: Monograph. // Lviv Polytechnic National University Institute of Telecommunications, Radioelectronics and Electronic Engineering. Dallas, USA: Primedia eLaunch LLC, 2022. 148 p.

ISBN 979-8-88796-802-5
DOI 10.36074/rrhmfsai-monograph.2022

The book is devoted to the development of radiation-resistant Hall magnetic field sensors and instrumentations for harsh radiation conditions in nuclear fusion reactors and charge particle accelerators.

Designed for scientists in the field of sensorics, radio physics, nuclear energy, as well as for lecturers, graduate and Ph.D. students.

UDC 62-9:539.16

ISBN 979-8-88796-802-5

CONTENTS

Introduction

The book is devoted to the development of radiation-resistant Hall magnetic field sensors and instrumentations for harsh radiation conditions in nuclear fusion reactors and charge particle accelerators.

The book contains four chapters presenting the problems of technology, design, in-situ self-calibration of magnetic sensors and the development of measuring devices based on them. Each chapter provides an overview of the current literary sources of these problems and the results of the authors' research in these areas.

The technology of radiation-resistant semiconductor sensors is presented in the first chapter. A wide range of radiation-resistant semiconductors for Hall magnetic sensors has been developed based on the technology of InSb, InAs, and GaAs microcrystals. The technology of InSb, InAs, and GaAs semiconductor microcrystals growth being doped by donor, isovalent, rare-earth impurities and based-on impurity complexes has been developed.

The radiation-resistant semiconductor 3-Dimensions (3-D) magnetic thin-film sensors able to measure three mutually orthogonal components BX, BY and BZ of the magnetic field induction are presented in the second chapter. Such 3-D sensors use an integrated structure of horizontal and vertical Hall sensors. In contrast to known solutions, the vertical sensor structures are formed in the intermediate area between the semiconductor layer and the dielectric substrate. Due to this solution, such structures are manufactured on thin-film technology of radiation-resistant sensors.

In-situ calibration methods for magnetic field sensors in harsh radiation conditions are presented in the third chapter. Based on these methods and the data fusion concept, a new type of magnetic field measurement unit, namely, Integrated Magnetometric Transducer, has been developed. It comprises a Hall sensor and an induction transducer. An increase in the measurement accuracy with in-situ calibration is achieved by the formation and use of test signals that are formed by induction transducers.

Based on the previously mentioned technique a set of magnetic field measuring instrumentation on Hall sensors for harsh radiation conditions is described in the fourth chapter. The set includes instrumentations for plasma magnetic field monitoring in nuclear fusion reactors, instrumentation for permanent cyclotron magnet magnetic field high precision mapping in charge particle accelerators, and instrumentation for investigating sensors directly during their irradiation in nuclear fusion reactors.

1. RADIATION-RESISTANT SEMICONDUCTORS FOR HALL MAGNETIC SENSORS

1.1. Overview of topics on semiconductors for Hall magnetic sensors

During the last decades, the magnetic field sensors and especially the Hall sensors (Hall-plate sensors, Hall effect transducers) attracted significant academic and industrial interest. The magnetic field sensors are the basis of many high-technology products, such as apparatus for linear and angular displacements, position change, non-contact measurement of AC and DC current and electrical power, signal amplifiers in telecommunication, spatial detectors of metal objects, three-dimensional vector magnetometers, compasses, etc. [1, 2].

Most recent results in Hall sensors developments and applications may be shown by the following topics: weak magnetic field detectors based on Hall-effect sensors [3], fabrication and characterization of InAs/AlSb based magnetic Hall sensors [4], field modulation for precise weak magnetic field measurement with a Hall-plate [5], room and cryogenic temperature behaviour of magnetic sensors based on GaN/Si single saw resonators [6], detection of a micron-sized magnetic particle using InSb Hall sensor [7], submicrometer Hall sensors for superparamagnetic nanoparticle detection [8], high-sensitivity InSb thin-film micro-Hall sensor arrays for simultaneous multiple detection of magnetic beads for biomedical applications [9], low magnetic field mapping using an InGaAs-AlGaAs-GaAs 2 DEG Hall sensor [10], temperature-stable Hall effect sensors [11].

This chapter addresses the problems of radiation-resistant semiconductors technology for Hall magnetic sensors. Such problems are discussed in the following recent publications: robust Hall effect magnetic field sensors for operation at high temperatures and in harsh radiation environments [12], electron, neutron, and proton irradiation effects on SiC radiation detectors [13], radiation test results in newly developed super-junction power MOSFETs [14], neutron radiation effects on the electrical characteristics of InAs/GaAs quantum dot-in-a-well structures

[15], effects of gamma irradiation on silicon carbide semiconductor radiation detector [16], radiation effects on high performance spaceborne electronics [17], characterisation of silicon diode arrays for dosimetry in external beam radiation therapy [18], proton radiation effects on Hamamatsu InGaAs PIN photodiodes [19], space radiation effects on SiC power device reliability [20], compact modeling of radiation effects in thin-layer SOI-MOSFET [21], feasibility analysis of establishing a physical model of radiation effects from SiC to device [22], evaluation of the radiation hardness of GaSb-based laser diodes for space applications [23], investigation of transient radiation effects in GaAs field effect transistors under pulse ionization [24], radiation damage effects on p-type silicon detectors for high-luminosity operations: test and modeling [25], application of isotope radiation sources for radiation effects simulation in semiconductor devices [26].

Significant progress has been done in the development of radiation-resistant technology on semiconductor III–V compounds ($A^{III}B^{V}$ group semiconductors). Semiconductor III–V compounds, those made from columns three and five elements of the periodic table, are important for a wide range of electronic devices [27, 28]. For example, optical devices from these materials span across multiple areas including optic telecommunications, chemical sensing, cutting tools, light-emitting diodes, such as those used for lighting, and solar cells.

While the success of Si-related devices in electronics is partly due to the high-quality interface between Si and its insulating oxides, III-V devices owe their success in optoelectronics to high-quality interfaces with compounds of different band-gap energies, for example, AlGaAs and GaAs, and InGaAsP-InP. These defect-free, high-quality interfaces allow for quantum confinement, high-efficiency carrier transport through multiple interfaces, and relatively low non-radiative recombination rates [29, 30].

The authors’ main results in technology and technique of parameters stabilization for Hall magnetic sensors on radiation-resistant semiconductors III–V compounds are presented in our publication [31-35]. A wide range of radiation-resistant semiconductors for Hall magnetic sensors has been developed based on the technology of InSb, InAs and GaAs microcrystals. The technological processes of microcrystal growing and doping were performed both in sealed quartz ampoules using iodine and hydrogen chloride as the carrier agents, and in chemical vapor deposition (CVD) flow systems using iodine and hydrogen chloride as gas carriers. For the development of the semiconductor microcrystals growth technique the modeling of technological processes of their growth from the gas phase using methods of equilibrium thermodynamics was performed. The calculated parameters of the technological processes were specified in the experiments on crystal growth from the gas phase by the chemical transport reactions method. For the increase in semiconductor materials' radiation stability we have developed the method of metallurgical doping by the impurities and by the doping complexes in the process of its growth with the following nuclear doping for the modification of microcrystal properties. This chapter briefly summarizes all these results.

1.2. Semiconductor materials and methods of their production

According to the condition of electroneutrality, all semiconductors can be divided into three groups. The first group consists of wide-gap materials (Si, GaAs, AlAs), for which the condition $n_{lim} \approx p_{lim}$ is fulfilled, which corresponds to the case of a fully compensated high-resistive semiconductor. For the second group of materials (InAs, InP) the ratio $n_{lim} >> p_{lim}$ is met, which corresponds to the material formation of n^+-type conductivity. The Fermi level in InAs during irradiation is shifted into the zone of allowed energies of conductivity zone, which corresponds to n^+-type conductivity material formation (with $n_{lim} \approx 3\cdot10^{18}$cm^{-3}) and the fixation of Fermi level at about $F_{lim} = EV + 0.52\ eV$. The third group consists of (Ge, InSb, GaSb, AlSb) semiconductors, for which the ratio $n_{lim} << p_{lim}$ holds, which should lead to the material formation of p^+-type conductivity as a result of irradiation.

Among the above-mentioned $A^{III}B^V$ group semiconductors, such compounds as GaAs, InAs, and InSb, according to their electrophysical characteristics, are the most convenient for magnetic field sensors because of their rather high charge carriers' mobility. However, only two of them – InAs and InSb – can be used in the radiation environment because GaAs becomes high-resistive material under high neutron doses irradiation.

Thus, such semiconductor materials as InAs and InSb can be recommended for the magnetic field sensors, which are to be operable in the radiation environment under normal temperatures. Along with this, it is necessary to develop the doping technology of these materials by appropriate chemical impurities up to such concentrations, which would provide the highest stability of the characteristics during irradiation by high doses of high-energy particles.

The selection among types of doping impurities was determined as follows. Reasoning from the above-mentioned predictions concerning InAs, the optimal concentration of charge carriers for getting highly stable InAs is the concentration of electrons, the value of which is close to the boundary value of the concentration of $n_{lim} = 3 \cdot 1018\ cm^{-3}$ and corresponds to the boundary position of the Fermi level $F_{lim} = EV+0{,}52$ eV in this irradiated material rich of radiation defects. So far as the band-gap energy of InAs is equal to Eg = 0,42 eV, the boundary position of the Fermi level Flim will be located in the conductivity zone. Therefore such a material is a semiconductor of n^+-type conductivity.

One can obtain the material with such optimal characteristics by doping it with donor impurities. The most appropriate donor impurity is Sn because, as the result of possible nuclear transformations when interacting with thermal and intermediate neutrons, tin is transformed into indium, which is one of the main elements of the crystal lattice. This transformation in the high doped ($n = 3 \cdot 10^{18} cm^{-3}$) InAs will not lead to visible changes in the material characteristics, charge carriers concentration in particular.

As for InSb, the problem of the creation of the material stable in radiation conditions is much more complicated. It is connected with the fact, that the material of n^+-type conductivity is needed for the development of magnetic field sensors with appropriately high charge carriers' mobility ($10^4 \div 10^5$ $cm^2 \cdot V^{-1} \cdot s^{-1}$). At the same time, the prognoses of the stability of this material show that fixation of the Fermi level Flim in the irradiated InSb rich in radiation defects leads to the formation of p^+-type conductivity with slow charge carriers' mobility of 10^2 $cm^2 \cdot V^{-1} \cdot s^{-1}$. So, for the creation of the high stabile InSb of n-type conductivity, which is appropriate for the magnetic field sensors, one should take measures to "delay" the shift of the Fermi level to its boundary Flim, which is characteristic for the irradiated material of p-type conductivity with slow mobility.

It can be simultaneous doping of the initial material InSb with several impurities of different properties, each of which fulfills certain functions when solving the problem of stabilization of characteristics of irradiated material along with saving of electronic type conductivity and proper charge carriers' mobility. The main donor impurity, which provides the necessary level of the charge carriers concentration of the material of n-type conductivity in such a compound impurity complex, must be Sn, upon the same reasoning as for InAs: as a result of nuclear transformations tin when interacting with thermal and intermediate neutrons in the fast neutrons fluxes, transforms into indium [8], which is one of the main elements of the crystal lattice.

Isovalent impurities (Al, Bi), which are the substitutional impurities in InSb, can contribute to the stabilization of electrophysical characteristics of InSb in the fields of high-energy radiations and when substituting the atoms in indium sublattice can create drains for radiation defects due to the difference of atom radii and appearance of the fields of elastic deformations, which lead to the deformations of the lattice potential. The rare-earth elements (Gd, Yb), which are able to form clusters in the material, can be effective getters of radiation defects. Moreover, introducing the deep impurity levels by such impurities as, e.g. Cr, can also stabilize electrophysical characteristics of InSb under irradiation exposure. The optimal ratio of the doping elements in compound impurity complexes is determined by experimental research.

Thus, for the creation of radiation-stable magnetic field sensors based on InSb, it is necessary to develop the technology of its doping by impurity complexes that consist of not only main donor impurity Sn, which provides n-type conductivity with the necessary concentration of free electrons, but also several other additional impurities e.g. Al, Bi, Cr, Gd, Yb that are favorable for the stabilization of material characteristics under harsh radiation conditions.

When choosing between the methods of obtaining high stable semiconductor materials, one should take into account that, firstly, the creation of radiation-stable materials assumes experimental research of the radiation effect on the characteristics of the material. The radiation exposure effect manifests itself in the appearance of defects, which leads to a change in material characteristics. Thus, the influence of the created radiation defects will be more visible in the material with less own structural defects, which appeared during this material manufacturing.

Besides, the quality of microelectronic devices considerably depends upon the perfection of initial materials. Modern semiconductor materials for electronic devices are obtained in the form of bulk monocrystals of big diameters, thin epitaxial layers, and also of microcrystals being grown from the gas phase. Their perfection is first connected with the number of dislocations, uniformity of doping and residual impurities distribution, with the number of intrinsic point defects, which include the vacancy defects, internodal atoms, and their complexes with impurity atoms.

These criteria of perfection are shown with the best correlation by microcrystals, which are obtained by free crystallization from the gas phase. They have the form of whiskers or thin films. Thin microcrystals with a thickness of only a few microns have the best structure: they are mostly dislocation-free or have one longitudinal dislocation. Thin crystals have an almost perfect surface.

In contrast to microcrystals, massive monocrystals of big diameters have a number of defects that may influence their properties. Among them, the most common are thermal stress, dislocations, impurity non-uniformity, and intrinsic defects.

Epitaxial thin film structures are naturally featured with the defect formation in the technological process, caused by the stresses that always appear in the process of crystallization and the following cooling. They are caused by the difference in lattice spacing and coefficients of substrate’s and epitaxial layer’s thermal expansion, accompanied by the appearance of composition gradient along the thickness of the epitaxial layer and increased concentration of structure defects on the grain boundaries, and also by the appearance of surface tension forces in the thin layers, which may cause the contraction or the stretching of the epitaxial layer.

Thus, of all the known forms of semiconductor materials, the most structurally perfect ones are microcrystals (whiskers or thin films) obtained from the gas phase. The creation of microcrystals with a small number of defects is facilitated also by the process of their growth, which occurs, as a rule, at temperatures considerably lower than the crystallization temperatures. The microcrystals’ structure is so perfect that their mechanical strength approaches the theoretical values resulting from interatomic forces.

Such structurally perfect defect-free microcrystals are the best model samples for investigation of the influence of external factors, which cause the defect formation in the semiconductor materials, for example, for the investigation of the influence of high-energy particle flux irradiation. Besides, microcrystals of semiconductor compounds AшBv can be effectively used as the sensor’s sensitive elements of various physical quantities, including magnetic field sensors.

In this chapter, a wide range of radiation-resistant semiconductors for Hall magnetic sensors based on the technology of InSb, InAs, and GaAs microcrystals is presented. The technological processes of microcrystal growing and doping are based on sealed quartz ampoules using iodine and hydrogen chloride as the carrier agents and chemical vapor deposition (CVD) flow systems using iodine and hydrogen chloride as gas carriers. Some examples of microcrystals being developed and described in this chapter are presented in Fig. 1.1.

a) b) c)

Fig. 1.1. Photographs of the microcrystals InSb (a), InAs (b), GaAs (c).

1.3. $A^{III}B^{V}$ group semiconductor material microcrystals growth from the gas phase

The first stage of the development of microcrystal growth from the gas phase is modeling physical-chemical processes, which occur in the gas phase of the systems under investigation. The thermodynamic analysis of the processes allows a considerable decrease in time consumption for determining the optimal parameters of semiconductor materials growth.

The process of obtaining semiconductor materials by chemical transport reactions, like any other technological process, is practically a non-equilibrium process. However, when using the sealed containers (in our case these were previously de-aired quartz ampoules), in which the withdrawal of reaction products out of reactionary volume is absent, the application of equilibrium thermodynamics apparatus is allowable, as some stages of the sedimentation process from the gas phase just slightly differ from the equilibrium state.

The obtaining of the equilibrium characteristics of chemical reactions' complex, which provide the basis for the technological process of semiconductor material obtaining from the gas phase allows drawing a conclusion about the most important characteristics of this process. These include some reactions' influence on the entire process, the determination of the leading stages and reaction of the given process, the validity of some reactions and components neglecting, the directedness of the reactions depending on the environment, etc.

Due to this reasoning, physical-chemical processes were modeled in sealed systems. In addition, experimental investigations in sealed quartz ampoules are quite convenient and considerably more energy-efficient in comparison with flow systems and allow performing a great number of experiments quite quickly. The determined basic technological solution has formed the basis for finalizing the technique of semiconductor crystal growth in the CVD flow systems, which allow controlling the technological process of growth and doping more flexibly.

In the course of the chemical transport reaction there occurs the transfer of a material, which is grown via the intermediate (gas) phase in the form of chemical compounds with the carrier agent. For the growth of the selected semiconductor compounds InSb, InAs and GaAs, J_2 and HCl were used. At that, the process passed through the following stages: chemical reactions of the basic material with the carrier agent in the source zone; the transfer of the reaction gaseous products into the sedimentation zone (crystallization zone); chemical reactions in the crystallization zone with the basic material release and the processes on the surface of the material which is under precipitation; the last stage is the withdrawal of the released reaction gaseous products and their transfer owing to the concentration gradient into the source zone.

The main results of the thermodynamic analysis are the data about the partial equilibrium pressures of the components at the given temperatures, total pressure, initial and equilibrium concentrations of system components, etc.

A minimum number of parameters, sufficient for the determination of the equilibrium system, is determined with the help of Gibbs' phase rule:

$$f = n + 2 - \Phi, \tag{1.1}$$

where f is the number of degrees of freedom (the number of independent parameters) of the system, n is the number of independent components, which is equal to the number of atoms (or atomic groups) comprising the system; Φ is the number of phases.

The total system of equations that describes the complex of chemical reactions of the technological process of obtaining semiconductor materials consists firstly of material balance equations, which are described in the form of equation (1.2) for the sealed systems, and secondly of the equilibrium equation (1.3):

$$P_{j\text{вих}} = \sum_{i=1}^{f} m_{ij} \cdot P_j, \tag{1.2}$$

$$K_i \sum_{i=1}^{r} \prod_i^q P_j^{\vartheta_{ij}}, \tag{1.3}$$

where f is the number of independent parameters of the system; is the number of i-type atoms in a j-type molecule; n is the partial pressure of the j-type component; is the stoichiometric reaction coefficient; q is the number of types of chemical reactions.

So, to find the solution for such systems of transcendental equations, some parts of gas phase components are usually neglected, as the general solution for such systems does not exist. Upon the analysis of the thermodynamic data of the system components, some parts of them may be excluded from the consideration in the temperature range studied before starting calculations. The calculation of the reaction equilibrium constants, which include those gas phase components that remained unconsidered, provides the possibility to determine the equation system that describes the equilibrium of the thermodynamic system studied.

For the calculation of the equilibrium constants of reactions that occur in the studied systems InSb-J_2, InAs-HCl and GaAs-HCl, the Ulich equation was used to a first approximation (i.e., using the values of specific heat capacity of the substances-reaction participants):

$$ln(K) = \frac{\Delta H_{298}^{0}}{R \cdot T} + \frac{\Delta S_{298}^{0}}{R} + \frac{\Delta C_{P298}^{0}}{R} \cdot \left(ln \left(\frac{T}{298} \right) + \frac{298}{T} - 1 \right), \qquad (1.4)$$

Where lnK – logarithmic reaction equilibrium constants; ΔH_{298}^{0} – total reaction enthalpy at the temperature T = 298 K, kJ·mol^{-1}; ΔS_{298}^{0} – total reaction entropy at the temperature of T = 298 K, J·mol^{-1}·K^{-1}; $\Delta \mathrm{C}_{298}^{0}$ – total heat capacity of the reaction at the temperature of T = 298 K, J·mol^{-1}·K^{-1}, T – temperature, K; R – gas constant, R=8,314 J·mol^{-1}·K^{-1}.

The calculations of reaction equilibrium constants and the partial pressures of gas phase components were performed in a wide temperature range, which was equal to T_{mel} ± 250 °C for each of the studied semiconductors.

1.4. Indium antimonide microcrystals growing and doping in the iodide system

InSb microcrystals were obtained from the gas phase using chemical transport reactions in the iodide system. The basic technological modes of InSb microcrystal growing were determined by modeling physicochemical processes, which occur in a sealed quartz container. It was determined from the performed thermodynamic analysis that the composition of the InSb-J2 system gas phase in the temperature range of 560÷1200K is determined by the components of InJ, InJ3, Sb4 and Sb2; and the reactions that are responsible for the indium antimonide transportation are the reaction of indium iodides disproportionation and the reaction of stibium dissociation:

$$2InSb_{(s,l)} + InJ_{3_{(g)}} \leftrightarrow 3InJ_{(g)} + 1/2Sb_{4_{(g)}} \qquad (1.5)$$

$$1/2Sb_{4_{(g)}} \leftrightarrow Sb_{2_{(g)}} \qquad (1.6)$$

The temperature dependence of partial pressures of InSb-J_2 system gas phase components is presented in Fig. 1.2.

The technological parameters of obtaining InSb microcrystals were determined from the data obtained and temperature dependence of reaction equilibrium constants: the initial pressure of iodide in the ampoule $P_{J_2}^0 = 5 \cdot 10^4 Pa$, the temperature of crystallization zone and source zone T_{cr} = (740 ± 20) K and T_s = (1020 ± 20) K, correspondingly. Here the approximation ± 20K when determining the temperature mode of the process corresponds to the degree of distinction in the initial thermodynamic data taken from the different reference sources.

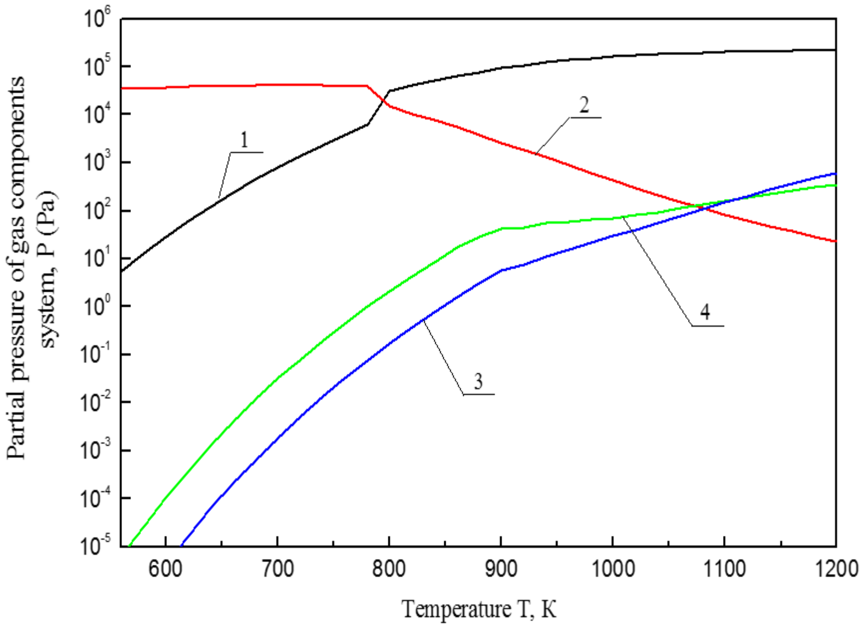

Fig. 1.2. Temperature dependence of partial pressures of system gas phase components at

$P_{J_2}^0 = 10^4 Pa$: 1 – P_{InJ} , 2 – P_{InJ_3} , 3 – P_{Sb_2} , 4 – P_{Sb_4}.

The doping impurities were introduced during the growing process. The introduction of doping impurity Sn for obtaining the microcrystals with the requisite electrophysical properties leads to the appearance of halides of tin SnJ_2 and SnJ_4 in the gas phase of the InSb<Sn>-J_2 system. The transfer of the doping impurity is primarily contributed by SnJ_2, the partial pressure of which is several orders higher than the partial pressure of SnJ_4 in the entire temperature range studied.

When introducing the doping impurity A1 into the gas phase of the InSb<Al>-J_2 system, aluminium monoiodide AlJ plays the key role in the transfer of this impurity to the crystallization zone, as the partial pressure of aluminium triiodide AlJ_3 is incommensurably lower. Here we should admit that the partial pressure of aluminium iodide relatively to the partial pressures of tin iodides is not large in the entire temperature range studied, which may result from the creation of a certain amount of solid solution AlSb when aluminium interacts with Sb_4 present in the gas phase.

Finding reliable thermodynamic data on Cr impurity in the existing reference literature appeared to be problematic. As the use of discrepant and inaccurate data leads to considerable errors in calculations, such calculations are of no use. By means of experimental investigations, the values of the crystallization zone temperatures for the growth of InSb doped crystals were specified. It was found out that the temperature of the crystallization zone differs by 3-5 K from that for undoped crystals when introducing a small quantity of doping impurities, while the error of calculated values of crystallization temperature is considerably higher (± 20К). Having taken these specifications into account, we experimentally specified the temperature of the crystallization zone of doped crystals for each type and quantity of impurity.

The introduction of rare-earth impurities Gd and Yb was performed in the form of these elements iodides GdJ_3 and YbJ_3. The preliminary calculations have determined the composition of the system gas phase with these impurities and the partial pressures of the main components.

The obtained InSb microcrystals have the shape of whiskers with the growth direction along one of the crystallographic axis <111>, <110>, <211> and the following dimensions: length (5 ÷ 10) mm; width (0,05 ÷ 0,07) mm, thickness (0,01 ÷ 0,03) mm (Fig. 1.1, a). They have a high degree of structural perfection, which is confirmed by high mechanical strength: the rupture strength is equal to approximately 1200 kG·mm-2 and tends to one calculated for the perfect lattice.

1.5. Indium arsenide and gallium arsenide growth in the chloride system

For determining technical conditions of InAs and GaAs microcrystals, physico-chemical processes for the InAs – HCl and GaAs – HCl systems were modeled, in the result of which the temperature modes of growth were defined.

When accomplishing the set task, we used the standard approaches, namely: the formation of an equation system of independent chemical reactions with the calculation of their equilibrium constants and temperature dependences of partial pressures of gas phase components. When calculating, it was assumed that the substances in the gas phase are subjected to the ideal gas law. The calculations were performed at the initial quantity of HCl in the ampoule of $1{,}23 \cdot 10^{-5}$ mol·cm^{-3} in the temperature range of 600¸950 K and 800¸1100 K for the InAs – HCl and GaAs – HCl systems correspondingly.

The analysis of thermodynamic parameters of all the gas phase components of the InAs – HCl system and the equilibrium constants of possible reactions in this system allowed us to single out the basic components that determine the transport of InAs: InCl, $InCl_2$, $InCl_3$, As_2 and As_4. It also allowed us to conclude that the basic reactions, which are responsible for the process performance in the system, are the reaction of indium chloride disproportionation and the reaction of arsenic dissociation:

$$2InAs_{(s)} + 2HCl_{(g)} \leftrightarrow 3InCl_g + 1/2As_{4_{(g)}}; \tag{1.7}$$

$$InAs_{(s)} + InCl_{2_{(g)}} \leftrightarrow 2InCl_{(g)} + 1/4As_{4_{(g)}}; \tag{1.8}$$

$$2As_{2_{(g)}} \leftrightarrow As_{4_{(g)}}. \tag{1.9}$$

As could be seen from Fig. 1.3, arsenic in the gas phase of the InAs – HCl system is represented mostly by the modification of As_4, as the partial pressure of this component in the entire temperature range is considerably higher than the partial pressure of As_2. The calculations of reaction equilibrium constants (1.7) and (1.8) have shown that the role of these reactions in the transport processes is almost equal. From these calculations the recommended temperature mode for InAs growing from the gas phase in the chloride system was determined: crystallization zone temperature (750 ± 20) К, source zone temperature (875 ± 20) K at the initial concentration HCl in the ampoule of $1{,}23\cdot10^{-5}$ mol·cm^{-3}.

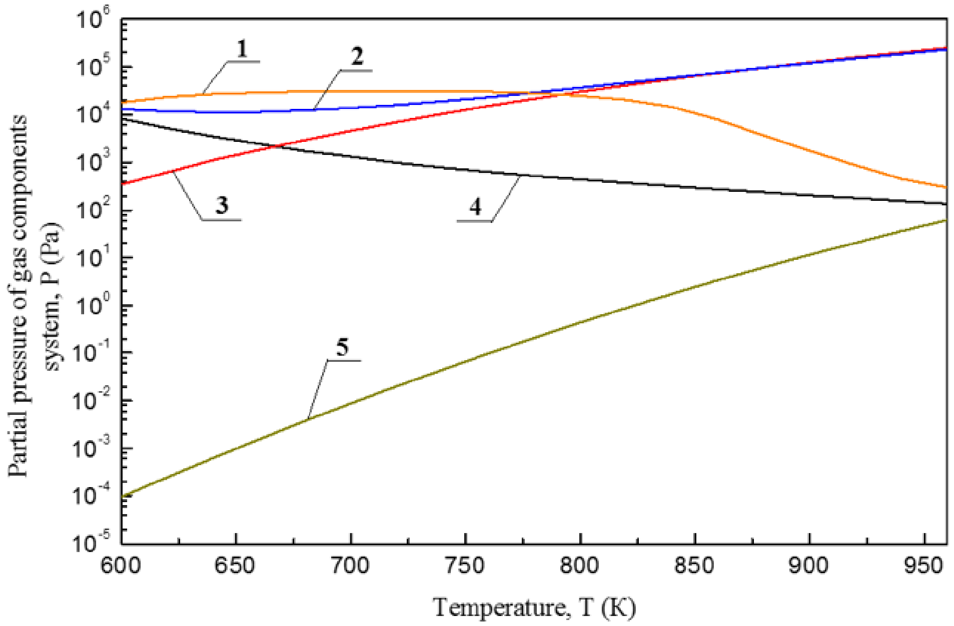

Fig. 1.3. Temperature dependence of partial pressures of gas components of the InAs-HCl system (at the initial pressure of HCl $P_{HCl}^{0} = 3 \cdot 10^{4}$ Pa):
$1 – P_{InCl_2}$, $2 – P_{As_4}$, $3 – P_{InCl}$, $4 – P_{InCl_3}$, $5 – P_{As_2}$.

InAs microcrystals were grown by the vapor–liquid–solid (VLS) mechanism using the eutectic of Au – InAs, whose melting temperature is somewhat lower than that of InAs and is equal to 720 K. The calculations performed for the process of InAs microcrystals growing with the introduction of doping impurity Sn have shown that the introduction of Sn into the system somewhat slows down the mass transfer of basic components, but does not distinctly affect the temperature mode of the growing process chosen earlier for the undoped crystals. The grown InAs microcrystals normally have the cross-section shaped as a triangle or trapezium with mirror edges and the following geometrical dimensions: width – 80¸120 µm, length – 5¸10 mm (Fig. 1.1, b).

During the thermodynamic calculations of the GaAs – HCl system, a technique similar to the analogous calculations of the InAs – HCl system was used. The basic components of the gas phase of this system are three gallium halides – GaCl, $GaCl_2$, $GaCl_3$ – and two modifications of arsenic: As_4 and As_2. The basic reactions which determined the transportation of GaAs in this system were the reaction of gallium chloride disproportionation and the reaction of arsenic dissociation:

$$2As_{2_{(g)}} \leftrightarrow As_{4_{(g)}}, \tag{1.9}$$

$$2GaAs_{(s)} + GaCl_{3_{(g)}} \leftrightarrow 3GaCl_{(g)} + 1/2\,As_{4_{(g)}}, \tag{1.10}$$

$$GaAs_{(s)} + GaCl_{2_{(g)}} \leftrightarrow 2GaCl_{(g)} + 1/4As_{4_{(g)}}, \tag{1.11}$$

In Fig. 1.4 one can see the computational results of partial pressures of these reactions in the studied temperature range, which is equal to 800¸1200 K for the GaAs – HCl system.

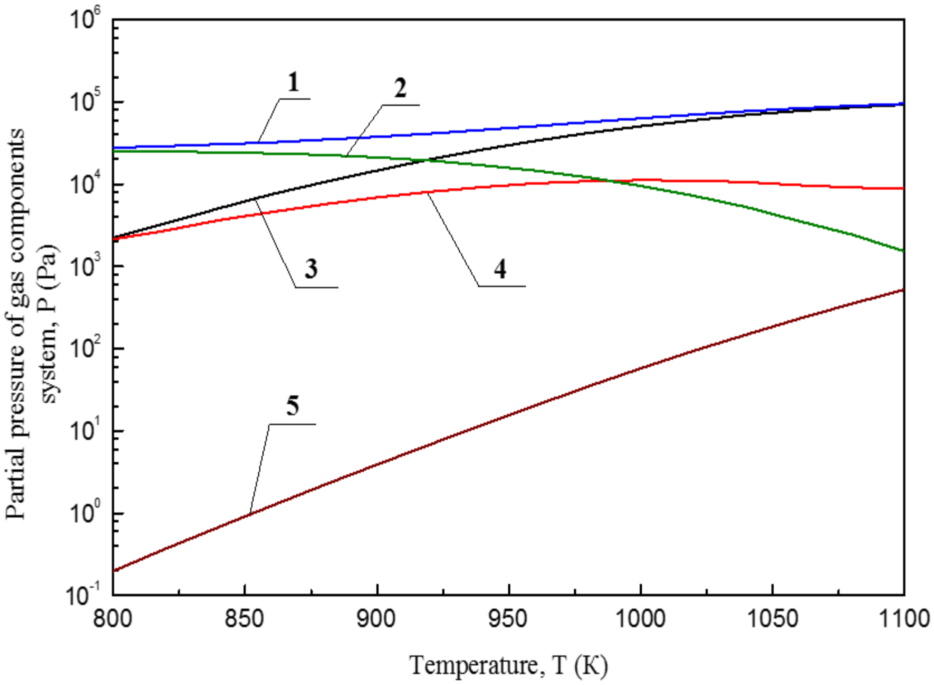

Fig. 1.4. Temperature dependence of the partial pressures of gas components of the GaAs-HCl system (at the initial pressure of HCl $P^0_{HCl} = 3 \cdot 10^4\ Pa$):

1 – P_{As_4}, 2 – P_{gaCl_3}, 3 – P_{GaCl}, 4 – P_{gaCl_2}, 5 – P_{As_2}.

Based on these calculations and the temperature dependence of equilibrium constants of basic reactions, the recommended temperature mode of the process of GaAs microcrystals growing was determined: the temperature of the crystallization zone is equal to (880 ± 25) K, the temperature of the source zone – to (1025 ± 25) K. GaAs microcrystals being grown at the initial concentration of HCl in the ampoule of $1{,}2\cdot10^{-5}$ $mol\cdot cm^{-3}$ have the shape of thin semitransparent films up to 5 mm long, 100 μm wide and 7 μm thick (Fig. 1.1, c).

1.6. Characteristics of the semiconductor microcrystals

The technology of growing and doping $A^{III}B^{V}$ semiconductor compounds in the process of growth was used for obtaining the samples of InAs, InSb, and GaAs microcrystals with the different composition of doping impurities and in a wide range of concentrations of 10^{15} cm^{-3} to 10^{18} cm^{-3}.

The investigation of temperature dependences of basic electrophysical parameters (charge carriers concentration, conductivity, Hall constant and carriers' mobility) in the obtained crystals was aimed, apart from parameters' controlling, to define the behavior of compound doping complexes in the microcrystals and their effect on the radiation stability of materials and sensors.

For the growing of InSb microcrystals, the undoped InSb as the initial material was taken with some quantity of uncontrolled impurities and charge carrier concentration of $n = 4\cdot10^{15}$ cm^{-3} at $T = 77$ K. The doping of InSb microcrystals was performed in the process of the growth by separate impurities Sn and Al, by the binary combinations of these impurities Sn:Al and Sn:Cr, by the combination of the basic doping impurity Sn with rare-earth impurity of Yb, as well as by the doping complexes Sn:Al:Cr. All InSb microcrystals obtained are featured by electronic conductivity.

The temperature dependencies of Hall constant R_H, specific conductivity σ, and charge carrier mobility μ are represented in Fig. 1.5 – Fig. 1.7. Curve A is the theoretically calculated temperature dependence of the Hall constant for pure InSb. The numbers of curves 1-9 correspond to the numbers of samples in Table 1.1.

Table 1.1

Basic electrophysical parameters of InSb microcrystals at T=77 K

№	Material	Charge carrier concentration n, cm^{-3}	Hall constant R_H, cm^3·C^{-1}	Conductivity σ, cm^{-1}·Ohm^{-1}	Mobility μ, cm^2·V^{-1}·s^{-1}
1	InSb	$4\cdot10^{15}$	1553	92	142900
2	InSb<Al>	$6\cdot10^{15}$	1034	104	107000
3	InSb<Sn>	$2\cdot10^{16}$	300	264	79000
4	InSb<Sn >	$6\cdot10^{16}$	98	605	58800
5	InSb<Sn:Yb>	$1\cdot10^{17}$	54	850	44400
6	InSb<Sn:Al>	$4\cdot10^{16}$	181	431	78000
7	InSb<Sn:Cr>	$9\cdot10^{16}$	70	776	53600
8	InSb<Sn:Al:Cr>	$5\cdot10^{16}$	125	346	43200
9	InSb<Sn:Al:Cr>	$1\cdot10^{17}$	60	465	28000

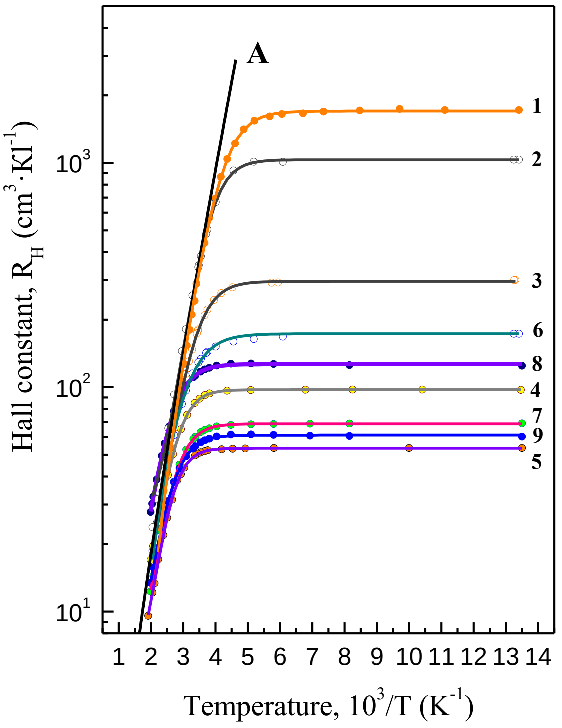

Fig. 1.5. Temperature dependence of InSb microcrystals' Hall constant.

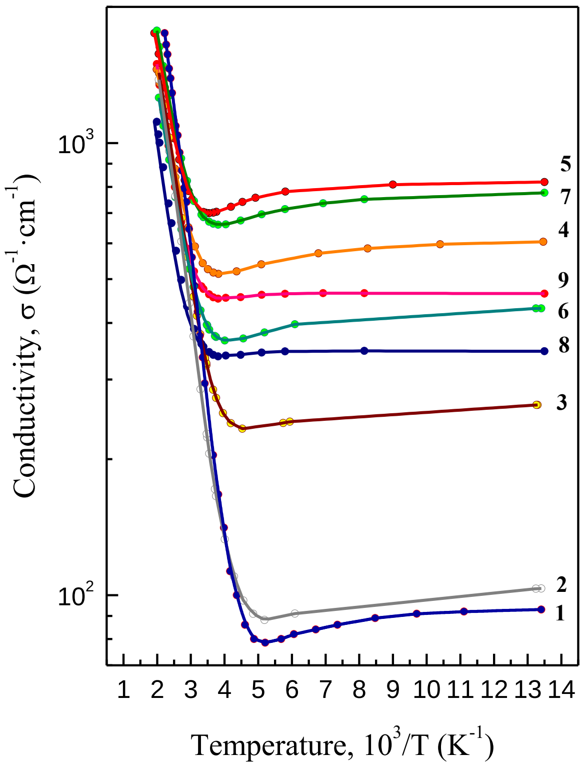

Fig. 1.6. Temperature dependence of InSb microcrystals' conductivity.

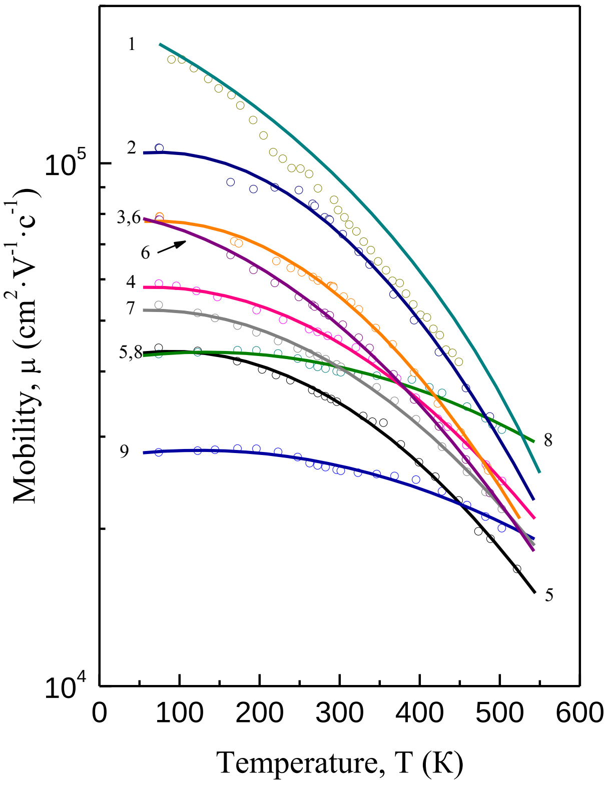

Fig. 1.7. Temperature dependence of InSb microcrystals' charge carriers mobility.

Temperature dependencies of the kinetic coefficient for all the studied samples are as expected for indium antimonide. Namely, in the zone of low temperatures up to 300 K the Hall factor remains unchanging, and the specific conductivity somewhat decreases in the way it is supposed to be in the zone of impurity conductivity up to the entire impurity exhaustion. In the zone of high temperatures, the change in RH and σ shows the transfer into the zone of mixed and inherent conductivity. The mobility of charge carriers in the whole temperature range studied steadily decreases with the temperature increase.

However, at the properties of all the temperature dependencies of kinetic coefficients in samples 8 and 9 doped by the impurity complexes of Sn:Al:Cr, one can observe some peculiarities that distinguish them from the other. Experimentally the curves of Hall constant dependence in the high temperatures zone for these samples (8 and 9) go beyond the approximated calculated straight line A for pure InSb, specific conductivity is as well somewhat lower compared to the other samples (3 and 4) with similar concentrations, and the temperature dependence of mobility is much weaker in the entire temperature interval. At high temperatures, where the conductivity of the studied samples is close to the inherent one, the Hall constant is determined first by the charge carrier concentration.

The calculation of band-gap energy has revealed that all the studied samples may be divided into two unequal groups by the value of band-gap energy Eg. In the first group, 7 samples are given (1…7), the band-gap energy of which is Eg = (0,23 ± 0,1) eV, which well coincides with the values of Eg for InSb. Among these samples there are undoped samples of InSb and doped separately by stannum, aluminium or chromium, as well as by their binary complexes. To the other group belong two samples (8 and 9), whose band-gap energy noticeably differs from the previous group: Eg = 0,28 eV, which exceeds the value of band-gap energy in the samples of the first group by 0,05 eV (i.e. 22%).

The results obtained for the kinetic coefficients and band-gap energy for samples 8 and 9 allow supposing that the presence of Cr in the vapor phase stimulates more effective entering of Al into the crystal lattice in the growing process compared to the doping of microcrystal separately by alumimium or aluminium with stannum. It may be supposed that when Al is entering into the InSb lattice the diluted solid solution $Al_xIn_{1-x}Sb$ is formed, whose band-gap energy is larger than in the initial InSb (the band-gap energy of AlSb is equal to 1,6 eV, the band-gap energy of InSb is 0,23 eV). Having taken the places in the indium sub-lattice, aluminium decreases the possibility of stannum basic donor impurity entering into this sub-lattice. Therefore, stannum starts taking the places in the Sb sub-lattice, where it shows its acceptor properties. This results in the degree of samples' compensation, which should lead to the decrease of charge carriers' mobility in the temperature range studied, which can be observed from the data in Table 1.1 that were obtained experimentally (samples 8, 9).

Besides, when introducing the rare-earth impurity Yb simultaneously with the basic impurity Sn we can observe a noticeable decrease in charge carrier concentration (sample 5 in Table 1.1). Obviously, the rare-earth impurity Yb interacts with shallow donors in InSb, creating the effect of basic material's "purification" which is typical for lanthanide-type elements.

For InAs microcrystals grown, being doped by stannum in the growing process, the character of change in Hall constant depending on temperature, conductivity and charge carrier mobility corresponds to the behavior of these parameters in the bulk crystal of electronic type. The temperature dependence of the Hall constant and conductivity for four samples 1 – $n=4{,}6\cdot10^{16}$ cm^{-3}; 2 – $n=9{,}2\cdot10^{16}$ cm^{-3}; 3 – $n=1{,}6\cdot10^{17}$ cm^{-3}; 4 – $n=1{,}4\cdot10^{18}$ cm^{-3} at T=77K with the different charge carrier concentration is represented in Fig. 1.8 and Fig. 1.9.

The electron mobility in n-InAs microcrystals in the zone of high temperatures (T = 300 K) is determined by the scattering mechanism on acoustic vibrations of the lattice, in the zone of low temperatures (T < 300 K) – by the scattering on acoustic vibrations and ionizing impurities.

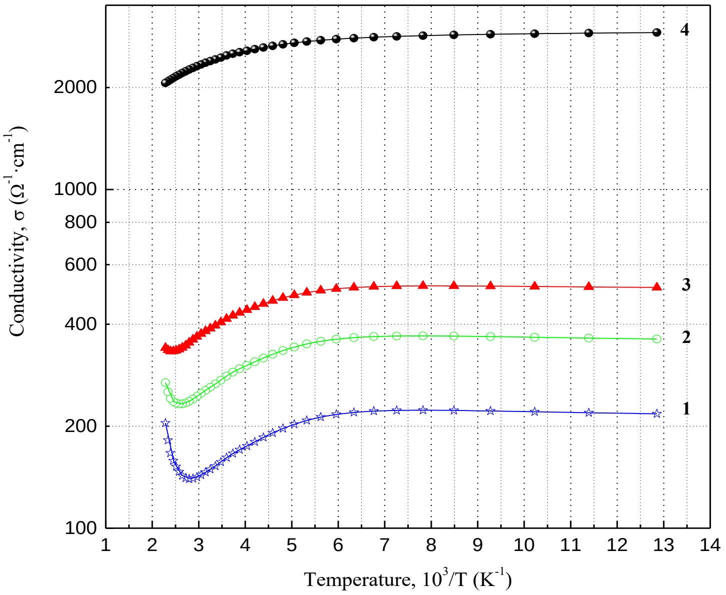

Fig. 1.8. Hall constant temperature dependence of InAs<Sn> microcrystals.

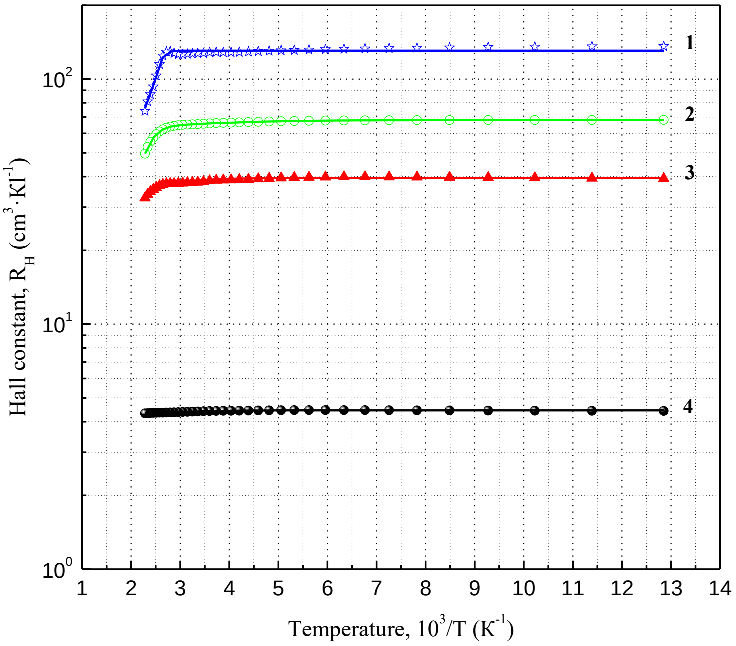

Fig. 1.9. Conductivity temperature dependence of InAs<Sn> microcrystals.

1.7. Characteristics stabilization technique for radiation-stable Hall sensors

In high-energy particle irradiation, the radiation defects in semiconductors are accumulated in the crystalline lattice, which causes the change of the Fermi level position, which leads to considerable changes in the material's electrophysical properties. The nature and properties of the radiation defects, especially in the compound semiconductor, are not known enough even nowadays, despite numerous investigations. Thus the development of the irradiation semiconductor's model, which does not require detailed information about the nature and the parameters of the radiation defects, is effective for the quantitative evaluation of the electrophysical parameters of the irradiated semiconductor.

Thus, the calculation of the irradiated semiconductor's theoretical model and the results of the experimental investigations show that Fermi level fixation in the defective bulk semiconductor, being exposed to high energy particle irradiation, occurs near the deepest defective level of the crystal in the semiconductor's band-gap zone. As this level is invariant relatively to the types of radiation damage in the crystal lattice, the model of Fermi level fixation is universal, as they depend upon the energy-band structure of bulk semiconductor only.

The electronic properties of the irradiated semiconductor (for example, the Hall effect) are determined by the peculiarities of the crystal's band spectrum near the band gap. Thus, owing to the peculiarities of GaAs energy spectrum Flim level is located near the middle of the band-gap, which causes a high resistivity of irradiated GaAs ($10^8 \div 10^{19}$) Ohm·cm at 300K, which makes it unusable for such devices as Hall magnetic field sensors.

At the same time, the Flim level for InAs is fixed in the conductivity band and provides n+-type conductivity of irradiated InAs, which is caused by the “low” position of G_{6C}, being formed by In cation, relatively to the Flim level energy. As for the irradiated InSb, the fixation of the Fermi level for it, like for the other binary antimonides, leads to a p-type conductivity resulting from a considerable spin-orbit split of the valence band.

From the theoretical presentation of the Fermi level fixation model and calculations performed, the following recommendations are given for using $A^{III}B^{V}$

semiconductor compounds for magnetic field sensors, being assigned for the operation under irradiation exposure. From the binary semiconductors GaAs, InAs and InSb, which are the most widely used by well-known companies (Lake Shore Corporation, Inc., FW Bell, etc.) for the development of Hall sensors, GaAs will be unusable for the operation under radiation exposure, as the boundary position of the Fermi level is equal to $F_{lim} \approx EV + 0.6\ eV$ and it is located near the middle of the band-gap, which for GaAs is equal to Eg = 1,51 eV, and makes GaAs high-resistive to irradiation.

For the irradiated InAs, the calculations determine the position of the Fermi boundary level as $F_{lim} \approx EV + 0.52\ eV$. In other words, it is located in the conductivity band (Eg = 0,39 eV). This position of the Fermi boundary level is in keeping with the value of boundary charge carrier concentration $n_{lim} \approx 3 \cdot 10^{18}$ cm^{-3}, at which this material is supposed to be high-stable in the radiation environment.

As for InSb, the problem of creating a radiation-stable material is much more complex. The point is that the theoretical calculations and experimental data indicate that the boundary level in irradiated InSb is equal to $F_{lim} \approx E_V$, which corresponds to the p+-type conductivity. However, for magnetic field sensors, InSb of n-type conductivity with high charge carrier concentration is used. Therefore to use it in the radiation environment, one should solve the problem of Fermi level shift “inhibit” before it reaches the boundary position F_{lim}. This problem can be solved by different technological methods, among which a method of InSb crystals doping by chemical complexes of certain compositions (Sn:Al:Cr) in the process of their growth with the following radiation modification of their properties proved to be effective.

The technique of semiconductor electrophysical characteristics stabilization by doping with chemical impurities in the process of growing semiconductor materials InAs and InSb was developed. It is necessary to take into consideration the possible nuclear reactions, which occur during neutron irradiation, in the fluxes of which there is always a part of thermal and resonance neutrons. Under the effect of this very part of reactor neutron flux, the transmutation reactions of lattice's basic elements into different isotopes take place.

For the elements of InAs and InSb crystal lattice, the basic nuclear reactions which lead to the creation of impurities are:

$$^{113}In(n,\gamma),\, ^{114}In \ \rightarrow^{\beta}_{49days} \ ^{114}Sn, \tag{1.12}$$

$$^{115}In(n,\gamma),\, ^{116}In \ \rightarrow^{\beta}_{54min} \ ^{116}Sn, \tag{1.13}$$

$$^{75}As(n,\gamma),\, ^{76}As \ \rightarrow^{\beta}_{26,4days} \ ^{76}Se, \tag{1.14}$$

$$^{121}Sb(n,\gamma),\, ^{122}Sb \ \rightarrow^{\beta,\gamma}_{2,8days} \ ^{122}Te, \tag{1.15}$$

$$^{123}Sb(n,\gamma),\, ^{124}Sb \ \rightarrow^{\beta,\gamma}_{21days} \ ^{124}Te. \tag{1.16}$$

In both selected materials InAs and InSb stannum is a basic (97%) final product of the reactions (1.12) and (1.13), and the concentrations of isotopes Se and Te created by the reactions (1.14) - (1.16) do not exceed 2,7 % and 2% respectively.

Thus, the basic impurity which will be additionally introduced at the neutron irradiation and will influence the properties of the selected materials is stannum. This reasoning became the ground for stannum selections as the basic donor impurity at the doping of InAs and InSb to provide the required level of charge carrier concentration in the material of n-type conductivity.

As it was already stated, stannum should be introduced in the process of crystal growing up to the boundary value of intrinsic carrier concentration, which is equal to $n_{lim} \approx 3 \cdot 10^{18}$ cm^{-3}, so that to grow InAs high-stable in the radiation fields.

So that to grow high-stable InSb of n-type conductivity, suitable for magnetic field sensors, a technology of InSb initial material doping by the impurity complex which consists of several impurities with different purposes (Sn:Al:Cr), each of which performs some functions in the irradiated material's characteristics stabilization having kept the electronic type of conductivity and sufficient charge carrier mobility, was developed. Due to the reasoning above, stannum was selected as a basic donor impurity, which provides for the required level of the material's charge carrier concentration of n-type conductivity material in such a compound impurity complex. The rest of the impurities in this impurity complex are intended to stabilize the electrophysical characteristics of InSb in the fields of high-energy irradiation. Isovalent impurity of aluminium, having replaced the atoms in the In sublattice, is intended to create drains for the radiation defects owing to the difference of atomic radii and the appearance of the elastic fields, which lead to the deformation of lattice potential. Chromium, having created a deep level in InSb, contributes to the "inhibit" of Fermi level near deep level and therefore stabilizes the materials' characteristics. The optimal ratio of doping impurities in the compound impurity complex is determined by experimental investigations.

Radiation modification of characteristics is applied in the complex technique after the stabilization of grown crystals' properties by their doping with chemical impurities in the process of growth.

Microcrystals of InAs among the investigated materials do not require the application of radiation modification technology, as their properties when doped to the boundary level of charge carrier concentration $n_{lim} = (2 \div 3) \cdot 10^{18}$ cm^{-3}, being determined from the theoretical predictions, are usable for manufacturing magnetic field sensors and stable under the conditions of high energy irradiation. The tests of the grown microcrystals have shown that their basic parameter, which is charge carrier concentration, does not change by more than 0,5% at the neutron irradiation up to the fluences of $F = 1 \cdot 10^{15}$ n·cm^{-2}. On the basis of such high stable microcrystals, radiation hard Hall magnetic sensors are manufactured.

Radiation modification is a necessary stage in high-stable microcrystals' creating technology for the other material investigated, which is InSb. It was performed after InSb microcrystals growth, being doped by the impurity complex (Sn:Al:Cr) up to the optimal charge carrier concentration, being determined by the experimental investigations of radiation stability of microcrystals with the different composition and ratio of doping impurities. The radiation modification consists in the technology of irradiation of InSb microcrystal by the neutron flux with a certain ratio of thermal, intermediate and fast neutrons in the total flux. Under the effect of neutron of the energetic spectrum composition specified, two competitive processes take place in InSb microcrystals: 1) nuclear doping with stannum due to the transformation of In lattice atoms into Sn with the participation of thermal and intermediate neutrons and 2) partial compensation of the electron material due to the introduction of radiation defects of acceptor type with the participation of fast neutrons. The amphoteric properties of the stannum basic doping impurity are taken into account in the process of radiation modification. According to these properties, when a certain level of stannum atoms concentration is achieved, the redistribution of stannum takes place between the sub-lattices of indium and antimonide.

The whole complex of the technological methods performed (complex doping with chemical impurities and radiation modification subject to amphoterism of the primary donor impurity) allowed obtaining high stable microcrystals of InSb, whose charge carrier concentration does not change by more than 0,05% at the tests under neutron irradiation up to the fluences of $F = 1 \cdot 10^{15}$ $n \cdot cm^{-2}$. The optimal charge carrier concentration in such high-stable microcrystals is equal to $n = 6{,}4 \cdot 10^{17}$ cm^{-3}. Such high stable microcrystals of InSb have formed the basis for radiation hard magnetic field sensors.

1.8. The investigation of nuclear-doped crystals’ radiation stability

According to modern theoretical models and experimental investigation, the parameters of the irradiated semiconductor depend primarily on the intrinsic fundamental characteristics of the materials (e.g., energy-band structure) and somewhat on the conditions of irradiation and materials’ prehistory.

A range of investigations was performed for the experimental verification of the basic principle of irradiated semiconductor’s theoretical model, which is a slight dependence of characteristics of the materials investigated InSb and InAs upon the prehistory of the materials, which is a method of obtaining and doping.

For the investigation, the crystals obtained by different methods were selected:

- Bulk InSb crystals obtained by the Czochralski melt method and doped by nuclear doping by neutron irradiation up to the fluence of $F \approx 1 \cdot 10^{17}$ $n \cdot cm^{-2}$, in the neutron reactor, in which the part of thermal neutrons is equal to 80%;
- InSb microcrystals obtained from the gas phase and doped by chemical impurities in the growing process;
- InSb microcrystals obtained from the gas-phase and nuclear-doped in a reactor by the technology being similar to those of bulk crystals;
- Bulk InAs monocrystals obtained by the Czochralski melt method and doped by nuclear doping;
- InAs microcrystals obtained from the gas phase and doped by chemical impurities in the growing process.

The performed investigation has shown that for both InAs and InSb the stability of characteristics at the testing in neutron fluxes depends on the value of charge carrier concentration only and does not depend on the material's prehistory, i.e., the method of growing and doping impurity introduction. Fig. 1.10 and Fig. 1.11 show the results of the test of InSb<Sn> and InAs<Sn> crystals irradiated in the neutron flux up to the fluence of $F = 1 \cdot 10^{15}$ $n \cdot cm^{-2}$ and obtained by the different methods. The obtained results are represented on the dependence curves of relative charge carrier concentration vs. initial concentration in crystals. These changes have the minimum values at the initial concentration for InSb of $n_0 = (6 \div 7) \cdot 10^{17}$ cm^{-3}, and for InAs – $n_0 = (2 \div 3) \cdot 10^{18}$ cm^{-3}, which are in good agreement with the results of the previous investigations for InSb and InAs microcrystals. Thus, the performed experimental investigations confirmed the principle of the theoretical model of irradiated semiconductors about the independence of

InSb and InAs irradiated materials' properties of the materials' prehistory, which is the method of obtaining and crystal doping.

However, the difference in the quality of the obtained materials when comparing the methods of nuclear doping and metallurgical doping in the growing process with the following radiation modification is considerable. It is represented in the degradation of basic electrophysical properties of nuclear-doped samples compared to the samples doped metallurgically in the growing process. This difference is especially notable in structurally perfect microcrystals of InSb and InAs, obtained from the gas phase.

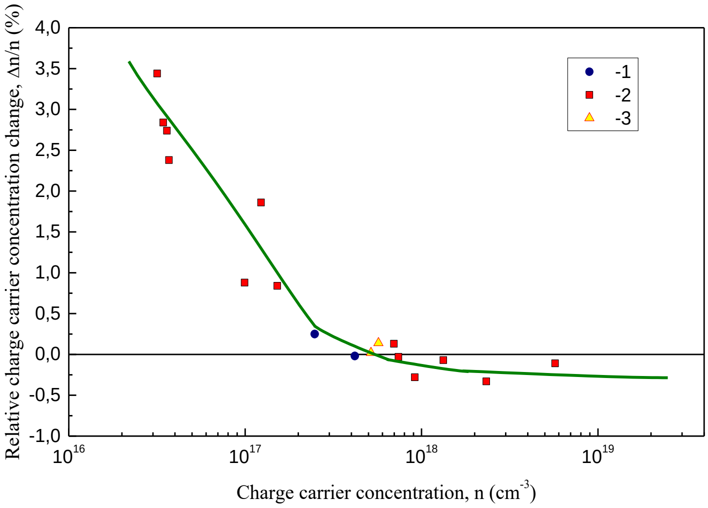

Fig. 1.10. Concentration dependence of relative change of charge carrier concentration for the samples of InSb<Sn>.

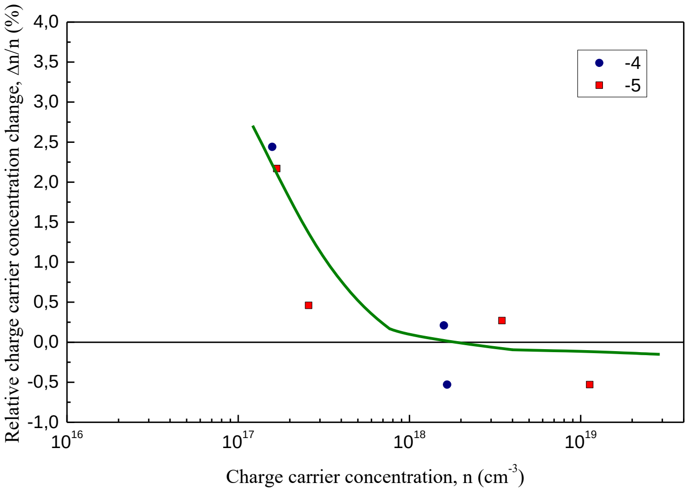

Fig 1.11. Concentration dependence of relative change of charge carrier concentration for the samples of InAs<Sn>.

The reason for these negative changes in nuclear-doped materials' characteristics consists in the fact, that the process of nuclear doping is not finished by the samples' doping only under the effect of neutron irradiation. The presence of so-called "fast" neutrons in the reactor spectrum, which feature high energy, causes the appearance of radiation defects and even the disordered areas in the irradiated material. Directly after the nuclear doping, if it was not performed at the increased temperatures, the density of the radiation defects greatly exceeds the concentration of the chemical impurity introduced at the nuclear doping, and the properties of the irradiated unannealed materials are determined primarily by the properties of defects introduced at the irradiation. The removal of radiation defects is one of the most important technological operations, and the quality of nuclear-doped materials depends on the completeness of such defects' annealing.

The annealing of the radiation defects is a complex technological task, as they form the complexes with impurities in the initial material, which results in the necessity for the development of different annealing modes (temperature, duration, atmosphere) for different semiconductor materials and even for the same material with the different composition of some deep residual impurity. The experimental results proved that the annealing of basic bulk of radiation defects in the irradiated semiconductors takes place in the temperature range up to the order (0,5 ÷ 0,7) of the material melting temperature T_{liq}. In highly irradiated semiconductors the annealing of the residual radiation defects continues up to the T_{liq}, and here the entire parameters' regeneration does not occur. This is caused basically by two factors – the creation of high stable radiation defects at high neutron fluences; and by the effect of impurities' polytropy in highly doped semiconductors.

So that to introduce a required quantity of doping impurity Sn into a material by the nuclear doping, the crystals should be irradiated up to much higher fluences compared to the fluences required for the radiation modification of crystals' properties.

The necessity of application of high fluences (F = 10^{17} n·cm^{-2}) for the introductions of impurities by the way of nuclear doping leads to a considerable decrease (1,5-2 times) of the charge carrier mobility due to the sputtering of a great amount of the simultaneously introduced radiation defects. For example, the charge carrier mobility of nuclear doped InSb crystals with no annealing is sinking to 9300 cm^{2}·V^{-1}·s^{-1} compared to 18700 cm^{2}·V^{-1}·s^{-1} in InSb microcrystals doped by chemical impurities in the growing process with the same charge carrier concentration of $n=6\cdot10^{17}$ cm^{-3}. For InAs, the ratio of mobility values in similar samples is equal to 12700 cm^{2}·V^{-1}·s^{-1} and 18400 cm^{2}·V^{-1}·s^{-1} respectively at the same charge carrier concentration for both samples of $n = 2\cdot10^{17}$ cm^{-3}. Thermoannealing, which is obliged to be performed at rather high temperatures, the whole regeneration of charge carrier mobility value in nuclear-doped samples is not achieved.

From the results of the investigations stated it follows that to obtain high-stable InSb and InAs semiconductor microcrystals for magnetic field sensors, for which the value of charge carrier mobility is vital, the preference should be given to the method of metallurgical doping for InAs and of metallurgical doping with the following radiation modification for InSb.

1.9. Summary for Chapter 1

The technology of InSb, InAs and GaAs semiconductor microcrystals growth being doped by donor, isovalent, rare-earth impurities and based-on impurity complexes has been developed. The technology uses a CVD flow system. The shape of whiskers and thin films have a very high level of structure perfection. They are effective prototype samples for the investigation of radiation stability and prototyping magnetic field sensors.

Experimental investigations have determined the effect of separate impurities and impurity complexes on the electro-physical properties of crystals grown. By the basic donor impurity Sn the microcrystals of InSb and InAs were obtained in a wide range of charge carrier concentrations of 10^{15} cm^{-3} to 10^{18} cm^{-3}. The introduction of rare-earth impurity of Yb into InSb shows itself in the decrease of charge carriers concentration and increase of their mobility when interacting with atoms of Yb with shallow donors in the basic materials. The use of impurity complexes Sn:Al:Cr leads to the increase of band-gap energy by 22% compared to the undoped crystals. The optimal ratio of doping elements in the compound impurity complexes, which leads to the stabilization of the material's parameters, is determined in the experiments on the investigation of radiation exposure effect on the crystals' characteristics.

The complex technique of high stable InAs and InSb microcrystals obtaining, which consists of theoretical prediction of irradiated $A^{III}B^{V}$ semiconductors' properties and recommendations regarding the initial parameters of high-stable materials InSb, InAs, GaAs for magnetic field sensors, technological methods of growing and the stabilization of doped microcrystals' characteristics, and methods of radiation modification of semiconductor crystals' properties were created.

The realization of the developed technique has allowed obtaining high-stable microcrystals InAs and InSb for radiation hard magnetic field sensors, the characteristics of which remain stable at the level of 0,5% та 0,05% respectively at the neutron irradiation up to the fluence of $F = 1 \cdot 10^{15}$ $n \cdot cm^{-2}$.

The experimental investigation of InSb and InAs crystals' radiation stability verified and confirmed one of the basic principles of irradiated semiconductors' theoretical model about the independence of irradiated materials' properties of the materials' prehistory, which is the method of crystal's obtaining and doping.

2. STRUCTURES AND MODELS OF 3-D THIN-FILM MAGNETIC SENSORS

2.1. Overview of topics on 3-D thin film magnetic sensors

Nowadays 3-Dimensions (3-D) magnetic sensors able to measure three mutually orthogonal components B_X, B_Y and B_Z of the magnetic flux density are of high interest. Such 3-D sensors use a specific combination of horizontal (normal) Hall sensors with vertical (tangential) Hall sensors, Split Hall Structures (SHS), or magnetotransistors. Typically, vector 3-D magnetic sensors form the basis of measurement devices for magnetic field mapping and defining the spatial position of objects in a reference magnetic field in different application areas including magnetic tracking [1].

An SHS-based 3-D magnetic sensor is designed as a bulk semiconductor integrated structure with 8 or more electrodes. Combining current flows through these electrodes and measuring the corresponding voltages, one defines projections B_X, B_Y, B_Z of the magnetic flux density vector. Typically, such an integrated 3-D sensor incorporates one component that serves as a traditional SHS whose sensitive axis (Z) is perpendicular to the semiconductor layer plane and two other components whose sensitive axes (X and Y) are parallel to the semiconductor layer plane. The latter two components are called vertical SHSs. Magnetotransistors are a bulk semiconductor integrated structure built upon dual-collector lateral transistors whose geometry is optimized in order to achieve high sensitivity of collector currents to the magnetic field.

It should be emphasized that fabrication of both SHS-based and magnetotransistor-based 3-D sensors requires structures that can only be obtained by solid-state silicon integrated circuit technology. However, such structures and, first of all, their p-n junctions, can boast neither high radiation nor thermal stability, which narrows the application area of most available 3-D sensors. So, a new generation of vector 3-D magnetic sensors is in high demand, primarily for usage in space, particle accelerators, and thermonuclear fusion reactors.

This chapter addresses the problems of developing a series of new SHS-based 3-D magnetic sensors that can dispense with p-n junctions and be implemented by thin-film technology traditionally used for manufacturing Hall sensors, including those based on InSb films. Due to this one can create 3-D sensors resistant to harsh environments, for instance, for magnetic field diagnostics in thermonuclear fusion reactors or increased radiation in industrial disaster management devices. Besides, the work proposes a SPICE model of a 3-D magnetic sensor which can be used when designing the proposed sensor and refining its calibration technique.

Let us consider typical problems of 3-D magnetic sensor design, research, and usage by examples of the newest scientific literature sources. Magnetic vector field sensor using magnetoelectric thin-film composites was proposed in [2], monolithic integrated 3-D magnetic field sensor based on MEMS technology – in [3], single-chip integrated 3-D Hall sensor – in [4], three-dimensional field sensing with magnetotransistors – in [5], low power 3-D-magnetotransistor based on CMOS (Complementary Metal-Oxide-Semiconductor) technology – in [6].

In [7] measurement characteristics of different integrated 3-D magnetic field sensors were studied, whereas [8] discussed planarization, fabrication, and characterization. Crosstalk analysis and current measurement correction in circular 3-D magnetic sensor arrays were given in [9]. In [10] misalignment and magnetic cross-sensitivity of integrated vertical Hall sensors were considered.

The literature covers problems of integrating 3-D magnetic sensors with other sensor technologies, including functionally integrated sensors on magnetic and thermal methods [11] and a soft magnetic 3-D Force sensor [12]. In [13] a 3-D magnetic field sensor concept for use in inertial measurement units was presented. Implementation of 3-D magnetic field sensors for magnetic tracking was presented in [14, 15] and for labs instrumentation – in [16]. Silicon on Insulator (SOI) 3-D structures for System-on-Chip Applications are presented in [17] whereas device-technological simulation of local 3-D SOI structures is covered in [18].

Problems of 3-D sensor simulation are discussed in the following publications: 3-D finite-element analysis of Giant magnetoimpedance thin-film magnetic sensors [19], a numerical methodology for a 6 DOF (Degrees Of Freedom) pose estimation with 3-D magnetic field sensors [20], spatial models of split Hall structures [21]. Key issues of 3-D sensor simulation are the detection of dependencies for further enhancement of sensor calibration techniques, including arbitrary rotation method for 3-D magnetic sensors calibration [22].

For the thin-film magnetic sensor presented in this work, SPICE (Simulation Program with Integrated Circuit Emphasis) modeling is used. SPICE includes many semiconductor device models, for example, resistors, capacitors, inductors, diodes, and transistors. Up-to-date versions of SPICE comprise independent voltage and current sources, ideal transmission lines, active components, and voltage and current controlled sources three levels of MOSFET (Metal-Oxide-Semiconductor Field Effect Transistor) model, a combined Ebers–Moll and Gummel–Poon bipolar model, etc.

Modern SPICE simulation concerns a wide range of scientific problems. To name a few, it includes developing models of organic light-emitting structures [23], ferroelectric transistors [24], and a thermoelectric module [25]. SPICE simulation of magnetic field sensors is covered in the following publications: Physical simulations of response time in Hall sensor devices [26], Behavioral model of magnetic sensors for SPICE simulations [27], Analysis and Modeling of One-Dimensional Folded Vertical Hall Sensor With Readout Circuit [28].

Upon the analysis of the above-mentioned literature sources, one can state that problems of 3-D magnetic sensor design and simulation are of current interest. The authors’ main results on the above-mentioned topics are presented in our publication [29, 30] and patents [31]. This chapter briefly summarizes these results.

2.2. Thin-film structure layers

The thin-film structure layers of presented further 3-D magnetic sensors and the main steps of their manufacturing are given in Fig. 2.1. The sensors' active area is the thin InSb films (1) of correspondent configuration formed at the semi-insulating GaAs substrate (2). Sensor contacts are formed by the metallization layer (3), which typically is the golden films together with other metals, for example, with a titanium sub-layer (Fig. 2.1, a). The common type of HG-sensors and MF-sensor presume InSb films with a thickness of about 1 µm. 3-D-sensors presume InSb films of thickness approximately 10 µm and require high precision etching of separate areas of these films, thinned to a few percent (2.. 10%) of their thickness. High radiation resistance of the sensors developed is provided by special InSb film doping methods.

For manufacturing the structures, three photolithographic processes are used. The first photolithography is intended for the creation of the contact system – Fig. 2.1, b; the second one is for etching InSb film into the whole depth – Fig. 2.1, c; and the third one is for etching the InSb film to 0.1 of their thickness – Fig. 2.1, d. The area of chips is about 1.5 mm×1.5 mm, and the dimensions of contact areas are 0.3 mm×0.3 mm. The general view of thin-film 3-D sensors is presented in Fig. 2.2, a piece of the manufactured wafer with sensor chips is depicted in Fig. 2.3 and separated sensor chips – in Fig. 2.4.

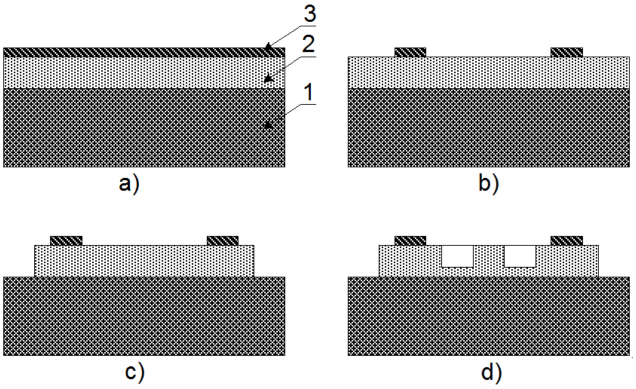

Fig. 2.1. The structure of film sensor layers.

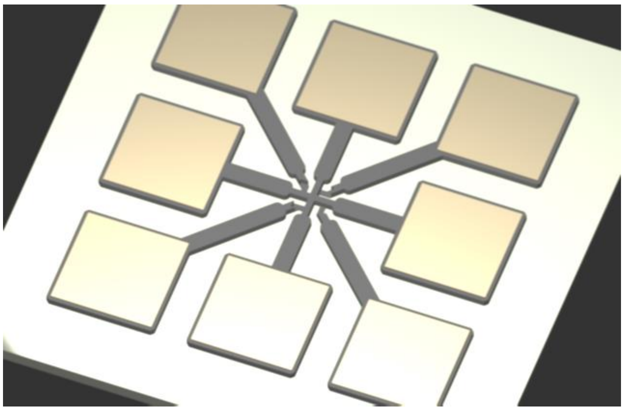

Fig. 2.2. General view of thin-film 3-D sensors.

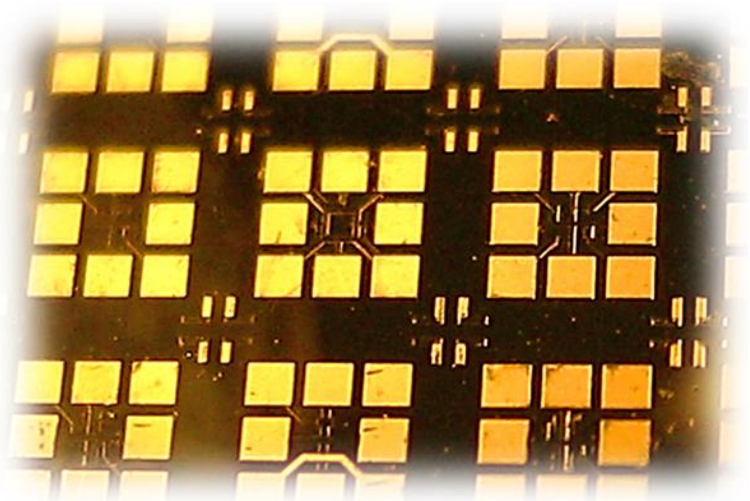

Fig. 2. 3. A piece of the manufactured wafer with sensor chips.

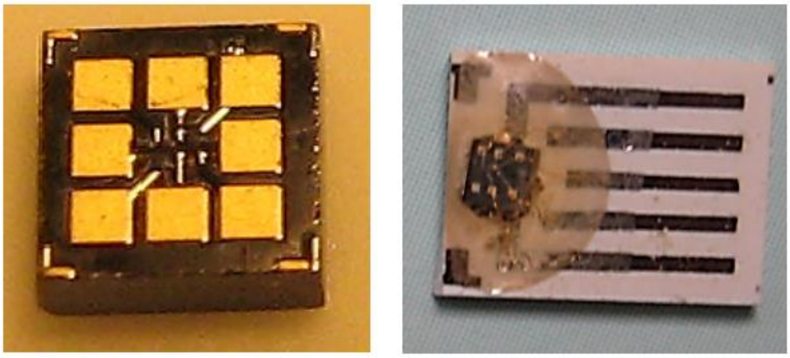

a) b)

Fig. 2.4. The separated chips of sensors (a) and a chip mounted on a substrate (b).

2.3. Sensor design #1

Sensor design #1 is the vertical Split Hall Structure (SHS) mentioned in the review. Its topology and intersection are shown in Fig. 2.5, where the following notations are used: 1 – substrate, 2 – semiconductor active area, 3 – central current electrode, 4 and 5 – lateral current electrodes, 6 and 7 – potential electrodes, 8 and 9 – auxiliary areas, 10 and 11 – intermediate areas. Intersection A-A of the vertical SHS and the directions of the magnetic flux density vector projections have been shown as well. Projections B_X and B_Y of the magnetic flux density vector lie in the plane of the transducer whereas projection B_Z is perpendicular to this plane. Such orientation of SHS is intended for measuring projection B_X of the vector.

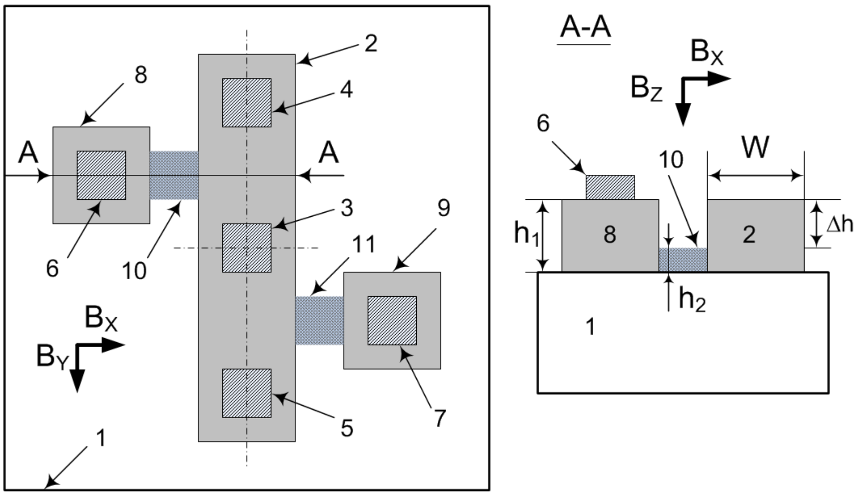

Fig. 2.5. Sensor design #1.

A simplified description of the SHS manufacturing process is as follows. A semiconductor InSb epitaxial film of thickness $h_1 = (7 \div 15)$ μm and doping concentration $N = (10^{16} \div 10^{17})$ cm^{-3} is grown on a high-resistance GaAs substrate. A contact system that provides a low-resistance ohmic contact to InSb and serves as contact areas is formed on the InSb epitaxial film by metallization with metals such as Au, Cu, etc.

As was mentioned before, the structure is manufactured in three stages. The first stage is aimed at etching the contact system. The second one is intended for etching an InSb film spanning across the whole thickness, h_1. During the third stage an InSb film spanning across nearly 90% of the film thickness, h_2, should be etched. Such incomplete etching of a semiconductor film in specific areas of the structure along with the corresponding structure geometry enables the implementation of a 3-D thin-film magnetic sensor. It is of key importance that the thickness h_2 of the intermediate areas, which are denoted 10 and 11, is much less than the thickness of the active area denoted 2.

A new solution is the principle of forming signals and the design of the basic component of such 3-D sensors – the vertical SHS. In contrast to known solutions, the potential (Hall) electrodes of the vertical SHS are formed inside the semiconductor layer rather than on its surface. Namely, the potential electrodes reside in the intermediate area Δh between the semiconductor layer and either dielectric or high-resistance semiconductor substrate. It enables the manufacturing of such sensors with no p-n junctions and no dielectric layer between the semiconductor and metallization layers.

The operation principle of a vertical thin-film SHS is as follows. The transducer is connected to a power supply, usually a current source. For this purpose, central current electrode 3 is connected to the first electrode of the power supply whereas lateral current electrodes 4 and 5 are connected together to the second electrode of the power supply. Thus, current in the working area is distributed equally and flows in two opposite directions with respect to the central current electrode.

Neglecting current in the circuits of two potential electrodes 6 and 7 one can assume that the potentials on these electrodes are equal to the corresponding potentials of intermediate areas 10 and 11. In this way, the design of the transducer enables forming of an output voltage on potential electrodes 6 and 7 that is equal to the voltage difference between the areas on the bottom surface of the active area near their contact with intermediate areas 10 and 11. As has been mentioned before, intermediate areas 10 and 11 are much thinner than active area 2, which ensures that the very potentials of the bottom surface of the active area are formed on potential electrodes 6 and 7.

In the general case, the voltages on potential electrodes 6 and 7 consist of three components. The first component, V_R, is caused by voltage drop at semiconductor active area 2. Taking into account that the active area is symmetric with respect to the first current electrode 3, the first components of the voltage on potential electrodes 6 and 7 are equal: $V_R(6) = V_R(7)$.

The second component, V_Z, is caused by projection B_Z of the magnetic flux density vector that is perpendicular to the transducer plane. Taking into account the transducer design and current flow directions in it, the second components of the voltage on potential electrodes 6 and 7 are equal as well, i.e., $V_Z(6) = V_Z(7)$.

The third component, V_X, is influenced by projection B_X of the magnetic flux density vector. In contrast to the previously mentioned two voltage components, this one has the opposite signs on potential electrodes 6 and 7: $V_X(6) = V_X(7)$. Particularly, under the influence of the Lorentz force in the top part (Fig. 2.5) of active area 2 charge carriers deflect to the top surface of the semiconductor layer whereas in the bottom part they deflect to the bottom surface, towards the substrate.

The difference in potentials that occurs due to such deflection of charge carriers is transmitted to potential electrodes 6 and 7 through intermediate areas 10 and 11. It is worth mentioning that projection B_Y of the magnetic flux density vector, which is parallel to the current flow direction in the active area, does not cause any charge carriers deflection and thus can be neglected: $V_Y(6) = V_Y(7)$. Thus, the voltage difference between potential electrodes 6 and 7 depends only on projection B_X of the magnetic flux density vector.

As has been said before, the proposed 3-D thin-film sensor includes two orthogonally placed vertical SHSs that provide sensitivity to projections B_X and B_Y of the magnetic flux density vector, and a horizontal Hall sensor sensitive to projection B_Z.

Fig. 2.6 shows the topology and a photo of the active area of a 3-D thin-film sensor on design #1. The active area of the horizontal Hall sensor is the central part of the 3-D sensor, i.e., the area where two orthogonally placed vertical SHSs intersect. Obviously, such a solution does not allow us to place current electrode 3, which has been shown in Fig. 2.4, in the central part of the sensor. This problem can be solved by an original approach to feeding the 3-D sensor.

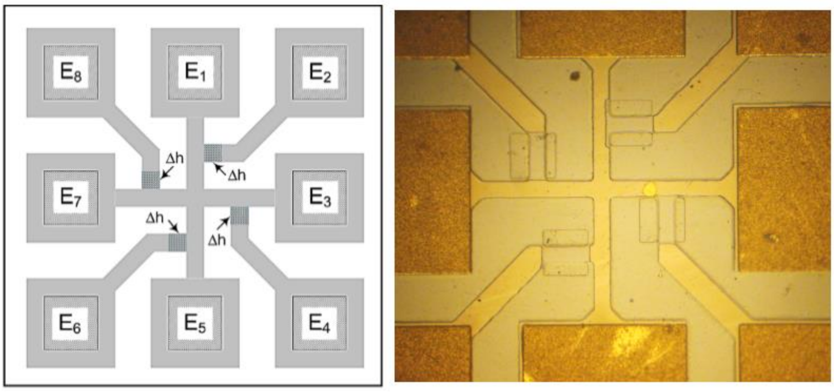

a) b)

Fig. 2.6. Topology (a) and a photo (b) of a 3-D thin-film sensor chip on design #1.

When measuring projections B_X and B_Y electrodes E_1 and E_5 of the 3-D sensor (Fig. 2.6) are connected to the positive electrode of the power supply whereas electrodes E_3 and E_7 are connected to its negative electrode. Thus two current flows with opposite directions are ensured: the current flows down from electrode E_1 to the structure center and up from electrode E_5 to the center. In the center of the structure these two current flows mix and then split again in two opposite directions – to the right, towards electrode E_3, and to the left, towards electrode E_7. These current flows with opposite directions in the proposed 3-D sensor are crucial for forming voltage differences $V(E_6) - V(e_2)$ and $V(E_8) - V(e_4)$ on the potential electrodes. The voltage differences are informative signals of projections B_X and B_Y of the magnetic flux density vector, correspondingly.

For the measurement of projection B_Z, which is perpendicular to the sensor plane, only four electrodes are used. Electrodes E_1 and E_5 serve as current electrodes whereas E_3 and E_7 – as potential ones, which is a typical way of operating horizontal Hall sensors.

To ensure the same sensitivity for the three SHSs inside a 3-D sensor one should take into account the following fact. In contrast to traditional horizontal Hall sensors whose sensitivity is inversely proportional to the thickness of the semiconductor active area layer, the sensitivity of vertical SHSs is inversely proportional to the width W of the semiconductor area. That is why it is recommended that the width W of the active area should be minimized and nearly equal to the thickness h_1 of the semiconductor layer.

Some modifications of a 3-D thin-film sensor on design #1 are presented in Fig. 2.7 and Fig. 2.8. The difference between these modifications is in the size and shape of intermediate areas 10 and 11 presented in Fig. 2.5.

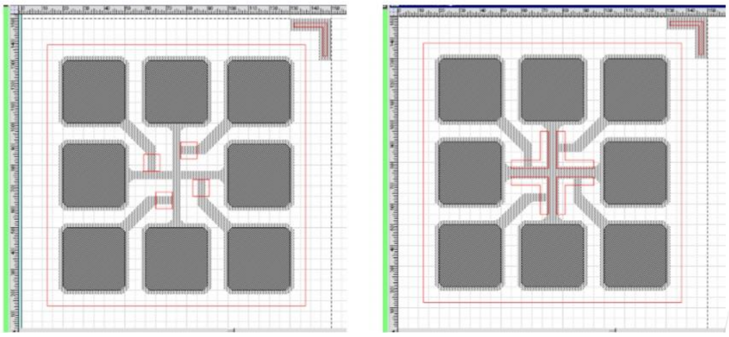

Fig. 2.7. Modifications of a 3-D thin-film sensor on design #1 (topology).

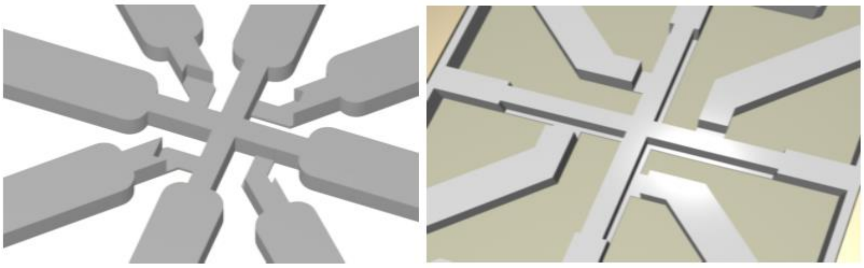

Fig. 2.8. Modifications of a 3-D thin-film sensor on design #1 (3-D view).

2.4. Sensor design #2

Sensor design #2 is shown in Fig. 2.9, where the following notations are used: 1 –semiconductor active area; 2 – outer insulating area; 3, 4, 5, 6 – four current contacts; 7, 8, 9, 10 – four voltage contacts; 11 – inner insulating area. The topology of a 3-D thin-film sensor on design #2 is shown in Fig. 2.10 and a photo of its chip – in Fig. 2.11.

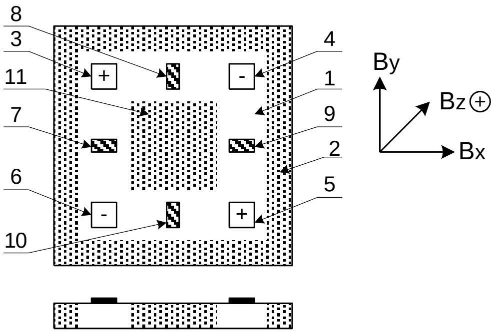

Fig. 2.9. Sensor design #2.

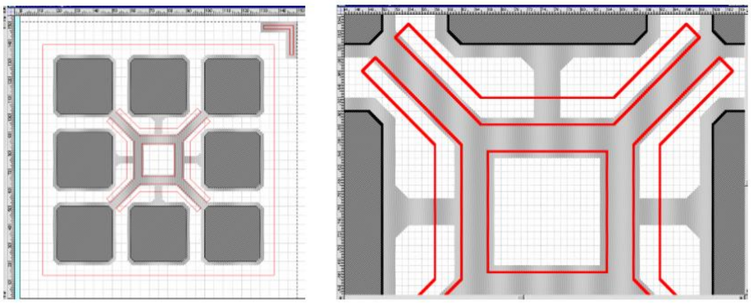

Fig. 2.10. 3-D thin-film sensor on design #2 (topology).

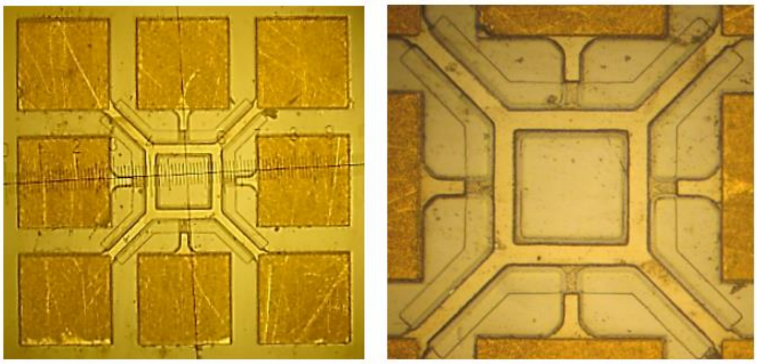

Fig. 2.11. 3-D thin-film sensor on design #2 (sensor chip).

The sensor design #2 transducer is fed by the current source, and one pair of mutually opposed current contacts (for example 3 and 5) is connected to one output of the power source (for example, positive), whereas another pair (4 and 6 correspondently) – to the other power source contact (negative, correspondently). According to this connection scheme, the four current flow circuits are formed: I_{34}, I_{36}, I_{54}, I_{56}, where the indexes in the marked currents correspond to the numbers of current contacts. These current flow circuits geometrically form the square sides.

The matter of principal importance is that the currents, that flow in opposed square sides are equal by value and opposed by sign: $\overrightarrow{I_{34}} = -\overrightarrow{I_{65}}$; $\overrightarrow{I_{36}} = -\overrightarrow{I_{45}}$. The output signal of the transducer is the voltage difference between the voltage contacts. The informative signals about the magnetic field vector projections B_X, B_Y, B_Z are the voltages V_X, V_Y, V_Z, which in first approximation are determined as:

$$V_X = V_8 - V_{10};\ V_Y = V_7 - V_9;\ V_Z = [(V_8 - V_9) + (V_{10} - V_7)]/2.$$

The novelty of sensor design #2 is the limitation of the area of current transition between the 2nd outer and 11 inner insulating areas. This provides an increase in the sensor sensitivity to the B_X and B_Y magnetic fields and decreases the cross-impact between the informative signals.

The increase in sensitivity is explained by reducing the active area size of the transducer. In contrast to the traditional Hall transducers (sensitive to the field B_Z perpendicular to the transducer plane), where the size that determines the sensitivity is the active area thickness, in the case of the B_X, B_Y field transducers the determinative size is the current scattering region area. The smaller the area occupied by the current scattering region, the higher the voltage difference between the two correspondent voltage contacts. As a result, sensor sensitivity is improved.

2.5. Sensor design #3

Sensor design #3 is shown in Fig. 2.12, where the following notations are used: I – the first Hall transducer; II – the second Hall transducer; III – electromagnetic compensation loop; IV – substrate. The topology of the sensor on design #3 is shown in Fig. 2.13 whereas a photo of its chip is given in Fig. 2.14.

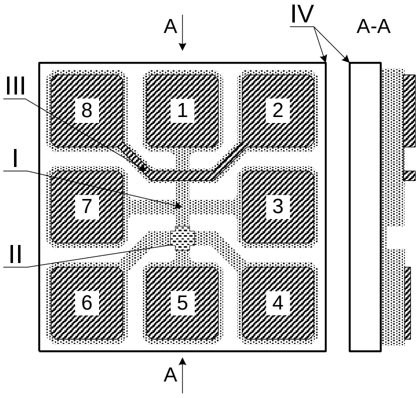

Fig. 2.12. Sensor design #3.

The type #3 transducer has 8 outputs, among which: 1, 5 – current outputs (common for the first and second Hall transducer); 3, 7 – voltage outputs of the first Hall transducer; 4, 6 – voltage outputs of the second Hall transducer; 2, 8 – outputs of electromagnetic compensation loop. The contact areas and electromagnetic compensation loop is formed in the metal film, which in its turn is deposited in the semiconductor material film. The manufacturing of the loop and its contact areas is performed in the same technological process as the Hall transducers' contact areas.

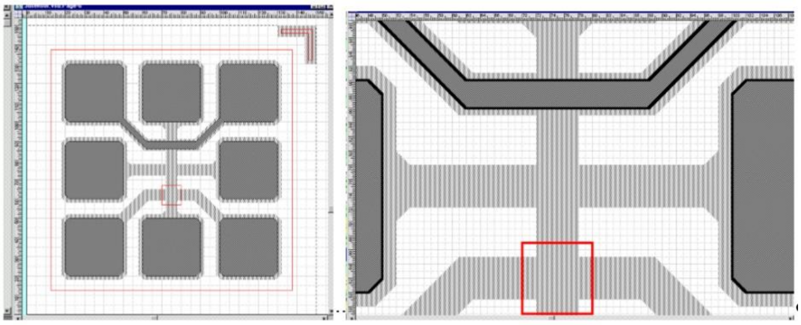

Fig. 2.13. Sensor design #3 (topology).

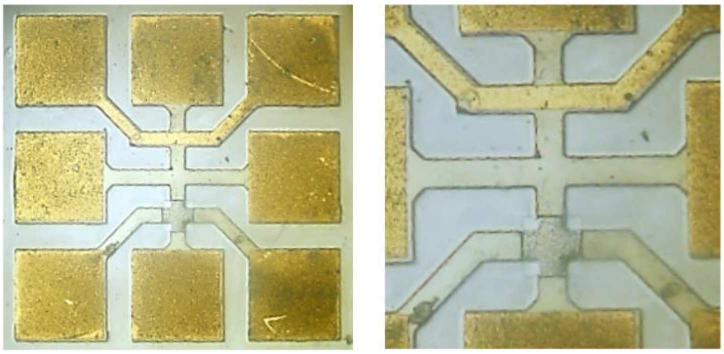

Fig. 2.14. Sensor design #3 (sensor chip).

The geometry of voltage outputs of the second Hall transducer II is mirror-symmetrical to the electromagnetic compensation loop III. The thickness of the active layer of the second Hall transducer II is smaller than the first one I.

Under the influence of the magnetic field the Hall voltages V_{H37} and V_{H46} are formed at the voltage outputs of the first I and the second II Hall transducers correspondently. In the first approximation, these voltages are determined as:

$$V_{H37} = \frac{R_H \cdot I_C \cdot B \cdot \cos\alpha}{d_I}, V_{H46} = \frac{R_H \cdot I_C \cdot B \cdot \cos\alpha}{d_{II}}$$

where R_H – is the Hall constant; I_C – Hall transducers supply current; B – magnetic field induction; $\cos\alpha$ – the angle between the magnetic field induction vector and the perpendicular to the Hall transducers plane; d_I and d_{II} – the thicknesses of the active layers of the first and the second Hall transducers.

When the transducer is under the influence of the magnetic field, there are also electromagnetic interference voltages V_{EM} formed at its outputs, whose values in the first approximation are proportional to the magnetic field change velocity and areas of closed circuits. These circuits are formed by the outputs of the transducer and signal transmission lines.

To provide the accurate measurement of alternate field induction values, electromagnetic interferences V_{EM} at the Hall transducers’ outputs should be considerably lower than in comparison to the Hall voltages V_H. It is obvious, that it is necessary to use the transducers with minimal circuit area, formed by the voltage outputs, and with maximal values of Hall voltages at these outputs. However, the practical realization of such transducers has its own restrictions.

First, decreasing the voltage outputs circuit area to the zero value is impossible. This area remains considerable, and mostly irreproducible by the value, even in case of a considerable decrease of Hall transducer dimensions. Besides, it is necessary to take into account that with the decreasing of the dimensions of the Hall transducers the irreproducibility of the dimensions increases considerably. This, in its turn, causes the increase of off-set voltage at voltage outputs. Thus, it is obvious that high-quality and high-stable Hall transducers may not have anyhow small dimensions.

Second, the increase of the Hall voltage i.e. the transducer sensitivity is possible only at the expense of decreasing the concentration of doping impurity of the active semiconductor layer or decreasing its thickness. However, the decrease in concentration worsens the transducer stability, whereas the decrease in the thickness deteriorates its time stability.

The positive effect of sensor design #3 is achieved by introducing the second Hall transducer with a smaller active layer thickness, and the geometry of the voltage outputs of the second Hall transducer is mirror-symmetrical to the electromagnetic compensation loop. The active layer of the first Hall transducer is formed by sufficiently thick (some micrometers) for providing high time stability of its parameters. On the contrary to this, the active layer of the second Hall transducer is formed as sufficiently thin (parts of micrometers) to provide the high values of Hall voltage, i.e. the high sensitivity of this transducer. The decreasing of the active layer thickness of the second Hall transducer is performed by selective removal (etching) of the semiconductor layer part. The electromagnetic compensation loop is contacted to the current flow circuit through the Hall transducers, which provides the stability of the co-phased voltage component at the outputs of this loop.

Thus, sensor design #3 contains a high-stable (the first) and a high-sensitivity (the second) Hall transducers, and the loop and voltage outputs of the high-sensitive transducer have equal sizes. The distances between the active parts of both Hall transducers, and between the Hall transducers and the loop are quite small (typically, not more than one millimeter). This allows assuming that first, magnetic field induction is equal in active parts of both Hall transducers, and second, that the electromagnetic interferences at the voltage outputs of the high sensitive Hall transducers and electromagnetic compensation loop are approximately equal by the value.

Using sensor design #3 in the high precision measurement devices for alternate magnetic fields presumes two operation modes. The first one is used for the direct purpose of the transducer, i.e. for measuring the field induction under the investigation, and the second mode is for transducer sensitivity control.

In the first operation mode, the second Hall transducer and electromagnetic compensation loop are used. As was stated above, at the outputs of the Hall transducer in the alternate magnetic field the electromagnetic interference V_{EM46} voltage is formed along with the useful signal V_{H46}. Namely, $V_{46} = V_{H46} + V_{EM46}$.

The presence of electromagnetic interference V_{EM46} decreases the measurement accuracy of the alternate magnetic fields. In sensor design #3, owing to the outputs symmetry of the second Hall transducer and electromagnetic compensation loop, the voltage of electromagnetic interference V_{EM46} at these outputs is approximately equal to the voltage at the electromagnetic compensation, V_{EM27}: $V_{EM27} \approx V_{EM46}$. During the signal processing the compensation of the interference voltage V_{EM46} at the voltage outputs of the second Hall transducer is performed using the V_{EM27} voltage. This allows the V_X signal extraction, which is close to the Hall voltage V_{H46}, which is the informative parameter of the measured magnetic field

$$V_X = V_{46} - V_{EM27} = V_{H46} + V_{EM46} - V_{EM27} \approx V_{H46}$$

However, as the result of such factors as certain asymmetry of the outputs and input impedance mismatch of the measurement circuits, further extraction of the useful signal is impossible. The higher the frequency of the measured magnetic field, the higher the interference voltage V_{EM46}, which causes the measurement accuracy to decrease. The minimization of the active layer of the second Hall transducer in sensor design #3 provides the increasing of the ratio between the useful signal voltage V_{H46} and interference voltage V_{EM46}. This, in its turn, contributes to the measurement accuracy increasing.

One should state that the high-sensitive Hall transducers with small thicknesses of the active layer have insufficient time stability, which requires the periodical control of their parameters. Such control is performed in the second operation mode of the type #4 transducer. For this, the latter is placed into one or some points of a permanent magnetic field and the voltages at the voltage outputs of both Hall transducers are measured. In this mode, the first and the second Hall transducers are used. The first Hall transducer has sufficiently high sensitivity stability, and therefore it is used as a reference during the sensitivity control of the second Hall transducer.

As a result of the performed control, the sensitivity of the second Hall transducer is determined. The period of performance of the control is determined by such factors as the time drift of the high-sensitive Hall transducer and the accuracy required for the measurements. So, using three components in type #4 transducer – high-sensitive Hall transducer, high-stable Hall transducer and electromagnetic compensation loop allows increasing the measurement accuracy of the high-frequency magnetic fields.

Besides, sensor design #3 may be used as a test structure for high-accuracy measurement of metal-semiconductor contact resistance. For this, current is fed through contact areas 1 and 2, and the voltage difference is measured at contact areas 7 and 8. The measurement result will be the intermediate resistance between the metal film (electromagnetic compensation loop) and semiconductor film $R = V_{78}/I_{12}$.

2.6. Sensor design #4

Sensor design #4 is shown in Fig. 2.15, where the following notations are used: 1 – substrate; 2, 3, 4, and 5 – four arms of the cross-shaped figure, formed by the crossing of two semiconductor areas of vertical Hall transducers; 6, 7, 8 and 9 – current contacts; 10, 11, 12 and 13 – voltage contacts; 14 – semiconductor area of a horizontal Hall transducer.

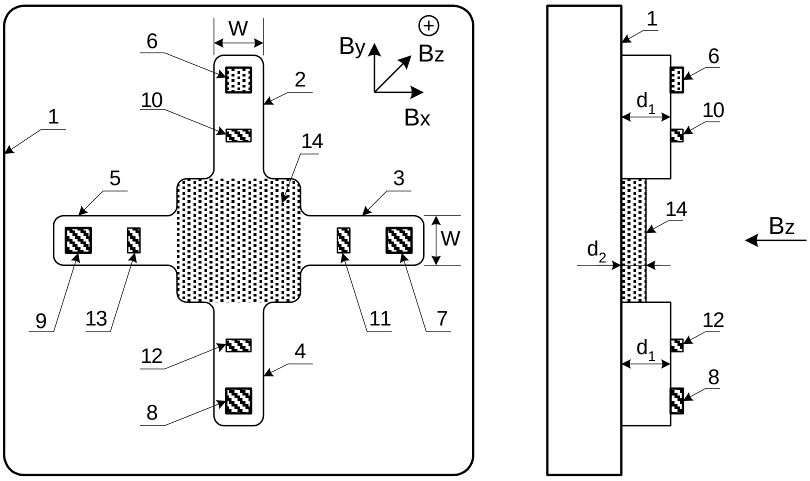

Fig. 2.15. Sensor design #4.

Arms 2, 4 and contacts 6, 8, 10, 12 form the first vertical Hall transducer, whereas arms 3, 5 and contacts 7, 9, 11 and 13 build the second vertical Hall transducer. The first transducer is intended for measuring the B_X magnetic field vector projection, and the second one – for measurement of B_Y projection. The measurement principle of Hall transducers is in forming the voltage difference at the voltage outputs during the deviation of charge carriers in the semiconductor area under the electromotive force influence.

The operation of sensor design #4 presumes two power supply modes. The first mode provides the operation of vertical Hall transducers, whereas the second one enables the operation of the horizontal one.

The first power-supplying mode presumes the connecting of the current contacts of the vertical Hall transducers when the currents in their semiconductor areas are flowing in mutually opposed directions. For this, the current contacts of both vertical Hall transducers are connected into one circuit. Namely, contacts 6 and 8 of the first vertical Hall transducer are connected together to the first, for example, positive output of the power source, whereas contacts 7 and 9 of the second vertical Hall transducer are also connected together to the second (therefore, negative) output of the power source. So, in the first vertical Hall transducer the currents are flowing from the top to the bottom (current I_2 in arm 2) and from the bottom to the top (current I_4 in arm 4), and in the second – from the left to the right (current I_3 in arm 3) and from the right to the left (current I_5 in arm 5). In the case of ideal symmetry of the transducer structure the equality takes place: $\overrightarrow{I_2} = -\overrightarrow{I_4}$; $\overrightarrow{I_3} = -\overrightarrow{I_5}$.

Output signals of vertical Hall transducers are formed at the voltage outputs as a voltage difference, which is proportional to the multiplication of the power-supply current value of the transducer and the correspondent magnetic field vector projection:

$V_X = V(12) - V(10) = K_X \cdot I \cdot B_X/W$ – for the first transducer and

$V_Y = V(13) - V(11) = K_Y \cdot I \cdot B_Y/W$ – for the second transducer,

where $V(10)$, $V(11)$, $V(12)$, $V(13)$ and $V(14)$ are the voltages at the voltage outputs 10, 11, 12, 13, 14, correspondingly; V_X, V_Y and K_X and K_Y – output signals and transducing coefficients of the first and second transducers correspondingly; I – operational current, W – the width of semiconductor areas.

From the physical point of view, the appearance of voltage difference at the voltage contacts of the vertical Hall transducers is explained by the fact that due to the opposed current flow directions in both transducer arms, the deviation of current carriers in those arms also has the opposed direction. In particular, if carriers in arm 2 of the first transducer deviate in the direction away from the substrate to the surface of the semiconductor area, then in arm 4 of this transducer carriers deflect in the opposite direction, from the surface to the substrate.

In a highly gradient magnetic field, the voltage difference formed at the voltage outputs of the vertical Hall transducers is the informative value of the averaged field induction value. Taking into consideration that all the voltage outputs of the vertical Hall transducers are equidistant from its center (crossing area), the measured averaged induction value corresponds to the spatial point of the transducer center.

The second power-supplying mode presumes the application of only one pair of current contacts, namely 6 and 8 of the first vertical transducer. Then, output 6 is connected to the first power supply output, and output 8 to the second one. This provides the linear trajectory of the charge carriers in semiconductor area 14 of the horizontal Hall transducer.

The output signal of the horizontal Hall transducer is a voltage difference, proportional to the multiplication of the transducer power supply current and the B_Z projection of the magnetic field induction vector, formed at the voltage outputs 11 and 13 of the second vertical Hall transducer:

$$V_Z = V(13) - V(11) = K_Z \cdot I \cdot B_Z / d_2$$

where K_Z is the transducing coefficient; d_2 is the thickness of the semiconductor area of the horizontal Hall transducer.

From the physical point of view, the appearance of the voltage difference at voltage outputs 11 and 13 is explained by charge carriers deviation in semiconductor area 14 of the horizontal Hall transducer under the influence of B_Z magnetic field induction vector projection that is in the direction from arm 5 to arm 3, or backward.

As in the vertical transducer, the horizontal Hall transducer measures the magnetic field induction value in the transducer center spatial point. Thus, type #3 transducer allows measuring all three projections B_X, B_Y and B_Z of the magnetic field induction vector in a single spatial point.

The other distinctive feature of the type #3 transducer is the possibility to change the d_2 thickness of the horizontal Hall transducer semiconductor area. This allows the formation of the transducer with equal sensitivity value to all three magnetic field induction vector projections: $V_X/B_X = V_Y/B_Y = V_Z/B_Z$. Taking into consideration that the sensitivity of vertical Hall transducers is inversely proportional to the semiconductor area width W, and for horizontal transducer – to the thickness of its semiconductor area d_2, the equality of the stated values of sensitivity is provided by the corresponding selection of W / d_2 ratio. It is important that in contrast to the d_1 thickness of the vertical Hall transducer areas, the d_2 thickness of the horizontal transducer semiconductor area may change after the outputs formation. In particular, the decrease of d_2 thickness may be implemented by partial etching of the semiconductor layer.

The increase in the accuracy is caused by the fact that the horizontal Hall transducer is placed in the center (crossing area) of the vertical Hall transducer. This provides the high spatial alignment of all transducers (two vertical and one horizontal), and therefore all the three projections B_X, B_Y and B_Z of the magnetic field induction vector are measured in a single spatial point. During the measurement of highly gradient fields, this gives the ability to decrease the magnetic field induction vector measurement error by several times. The simplifying of construction is caused by a series of circumstances. First, the measurement function of magnetic field three projections is performed by one transducer instead of a set of vertical and horizontal transducers. Second, the number of transducer outputs is decreased.

Usage of sensor design #4 is mentioned to be merged with the above-presented sensor design #1 and its implementation requires no further explanation.

2.7. SPICE model of 3-D magnetic sensors

In contrast to traditional Hall sensors, 3-D magnetic sensors on SHSs have much more complex measurement conversion functions. Moreover, to obtain their signals, one needs more complex signal transducers. That is why unified approaches to circuit simulation in SPICE allow us to simplify the synthesis and analysis of the equivalent circuit of an SHS. Having compared the signal families obtained during the analysis of these equivalent circuits with the experimental results, it is possible to refine the SHS model and then form arrays of data that can be used for developing calibration techniques.

It is worth mentioning that, for several reasons, it is impossible to use SPICE or SPICE-based programs directly for magnetic sensors simulation. Firstly, SPICE libraries do not support any magnetic field parameters. Secondly, simulation analysis of Hall sensors, especially structurally complex ones based on SHS, should account for changes not only in the magnetic flux density but also in the sensor position in a magnetic field. Moreover, depending on the simulation analysis objectives, the function can have the following arguments: the magnetic flux density vector length, the projections of the magnetic field vector onto the coordinate system associated with the sensor (its spatial position), and the parameters of the sensor structure or temperature.

To solve the above-stated problem, a SPICE model of 3-D magnetic sensors has been developed. The model is based on equivalent circuits whose elements are controlled by formal analogs’ parameters, namely, voltage, current, or resistance. Such formal analogs are the parameters of auxiliary circuit components that formally describe the numerical values of the magnetic field, the position of the sensor in the magnetic field, and the coefficients of the functional characteristics of the sensor, including its sensitivity, offset voltage, input, and output resistance, etc.

SPICE and MicroCAP libraries offer a wide range of typical components: resistors, capacitors, diodes, transistors, and controlled voltage and current sources (VofV, VofI, IofV, IofI, NFV, etc.) whose syntax allows to preset the dependencies of the source output on some specific voltages or currents in the circuit in analytical or table form. From the point of view of designing equivalent circuits for SHS, the models of the elements that synthesize such equivalent circuits should allow an analytical description of:

- controlled voltage sources for Hall voltages simulation;

- controlled resistors for modeling ohmic signal components;
- functional dependencies between the parameters of Hall sensors and the magnetic field vector components that are implemented by formal analogs and described using trigonometric functional relationships, particularly the dependencies of the Hall and ohmic signal components on the sensor tilt angle in the magnetic field.

Analysis of the functional and parametric capabilities of the controlled sources has shown that controlled voltage sources of NFV type are the most reasonable choice for the synthesis of Hall voltages.

The functional dependency of the Hall voltage on angle α_N between the magnetic field vector B and the perpendicular N to the sensor plane, $V_H = V_M \cdot \cos \alpha_N$, can be formally described analytically as $V(E) = V_M \cdot \cos(V(1) \cdot \pi/180)$ where $V(E)$ is the voltage of the NFV source E; $V_M = 1V$ is the normalized maximum voltage; $V(1)$ is the voltage in node (1) formed by voltage source Va. The latter is the formal analog of the tilt angle, $V(1) = V(V_a) \equiv \alpha_N$, as shown in Fig. 2.16. An example of the modeling analogy obtained in this way is shown in Fig. 2.17.

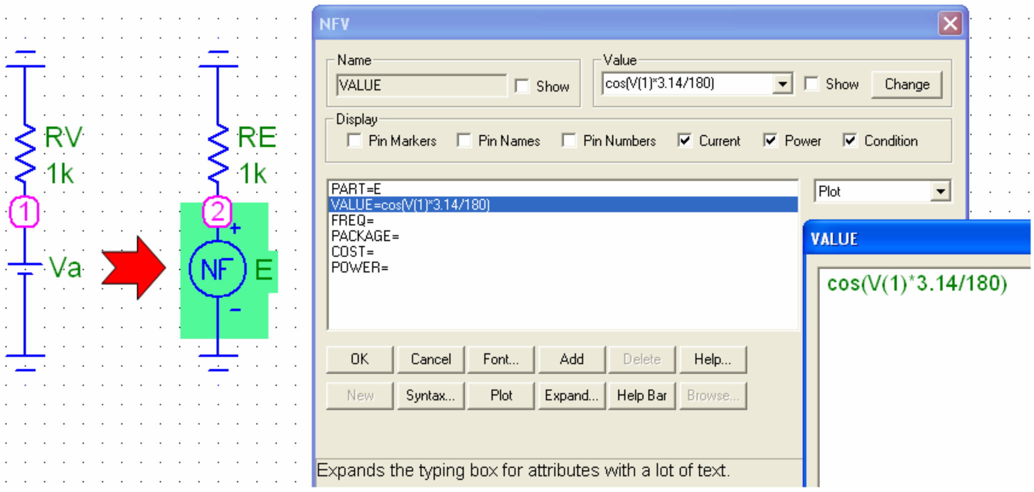

Name: VALUE

Value: cos(V(1)*3.14/180)

PART=E
VALUE=cos(V(1)*3.14/180)
FREQ=
PACKAGE=
COST=
POWER=

cos(V(1)*3.14/180)

Expands the typing box for attributes with a lot of text.

Fig. 2.16. An example of an NFV-type voltage source control circuit.

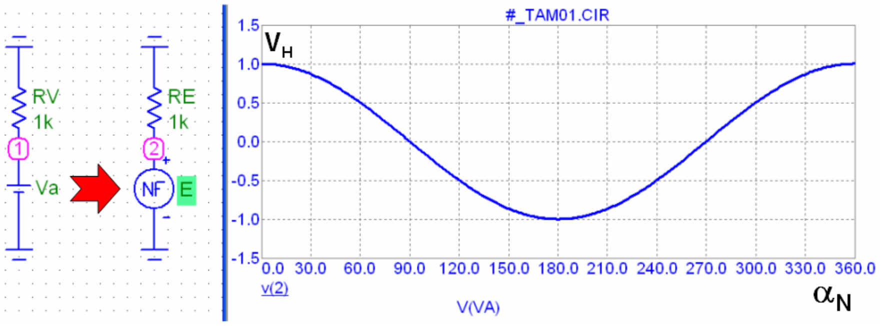

Fig. 2.17. An example of the modeling analogy between Hall voltage V_H and angle α_N.

A model of a functional resistor whose resistance can be set analytically is used for the synthesis of the sensor magnetoresistive structure. Fig. 2.18 depicts a sample result of synthesizing the quadratic dependency of resistance R_B of the sensor resistive structure on magnetic flux density B: $R_B(B) = R_0 \cdot (1 + K_{RB} \cdot B^2)$ in the form of dependency $R(R_1) = R_0 \cdot (1 + K_{RB} \cdot V(1)^2)$ where $R_0 = 100$ is resistance at B = 0; K_{RB} is the quadratic magnetoresistance coefficient; $V(1) = V(VB) \equiv B$ is the formal analog of the magnetic flux density.

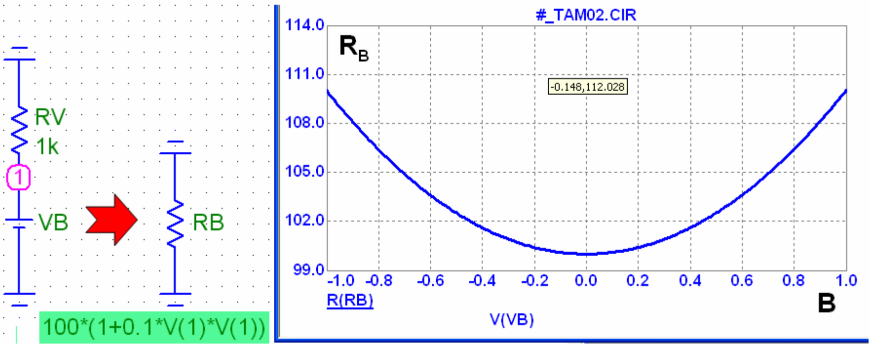

Fig. 2.18. A sample specification for a magnetoresistive structure model.

Upon the above-mentioned approaches for component specification, an equivalent circuit for the SPICE model of a 3-D magnetic sensor has been synthesized (Fig. 2.19). The model uses the following functional components as formal analogues:

- VB as the analog of the magnetic flux density vector B;
- Valf and Vbet as analogs of angles α and β of the magnetic flux density vector orientation in respect to the SHS plane;
- RE and RV as analogs of the magnetoresistance coefficient;

- EBX, EBY, EBZ as analogs of the Hall voltages in respect to axes X, Y, Z.

These functional components can be placed and connected arbitrarily since it’s their numerical values, not the result of interaction in the circuit, serve as the informative value in this representation. However, one should make sure that there are no idle speed modes or short circuits in the voltage sources since they usually cause a SPICE syntax error. When appropriate, other functional components may be added to the model, including those needed for the description of the planar effect coefficients and SHS asymmetry.

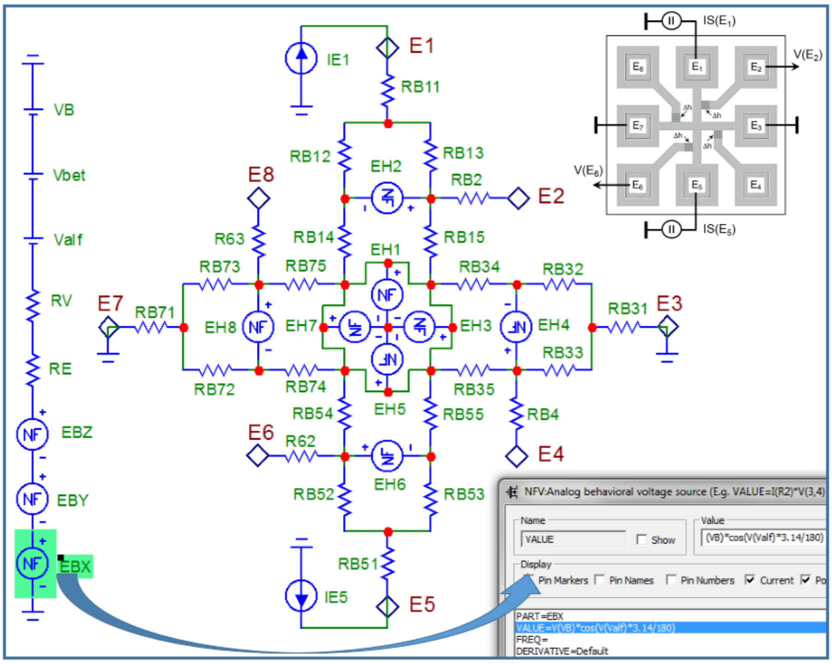

Name: VALUE ☐ Show

Value: (VB)*cos(V(Valf)*3.14/180)

☐ Pin Markers ☐ Pin Names ☐ Pin Numbers ☑ Current ☑ Po

```
PART=EBX
VALUE=V(VB)*cos(V(Valf)*3.14/180)
FREQ=
DERIVATIVE=Default
```

Fig. 2.19. The SPICE model equivalent circuit.

Then upon the obtained numerical values of the functional components, the equivalent circuit of the SHS structure is synthesized. For this purpose, we use the above-mentioned controlled resistive components RB** and voltage sources EH** (here ** denote the component number). At the final stage, we equip the synthesized equivalent circuit with an electric feeding circuit including current sources IE1, IE5.

Fig. 2.20, a shows sample simulation results including the normalized signals S_X and S_Y that represent the dependencies of the output voltage differences between electrodes E2 and E6 (signal S_X) and electrodes E4 and E8 (signal S_Y) on the rotation angle (Angle, deg) of the structure in the magnetic field. The simulation was conducted for three values (1, 2, 3) of the structure asymmetry that was marked with some discrepancies in the modulation coefficients of the model components' parameters. Fig. 2.20, b visualizes an evaluation of such asymmetry with normalized dependencies $S_Y = f_{XY}(S_{XY})$. When the structure is ideally symmetric, the following condition should hold: $S_X^2 + S_Y^2 = const$. Taking into account this fact, one can assess the asymmetry by the extent to which function f_{XY} deflects (2, 3) from an ideal circle (1).

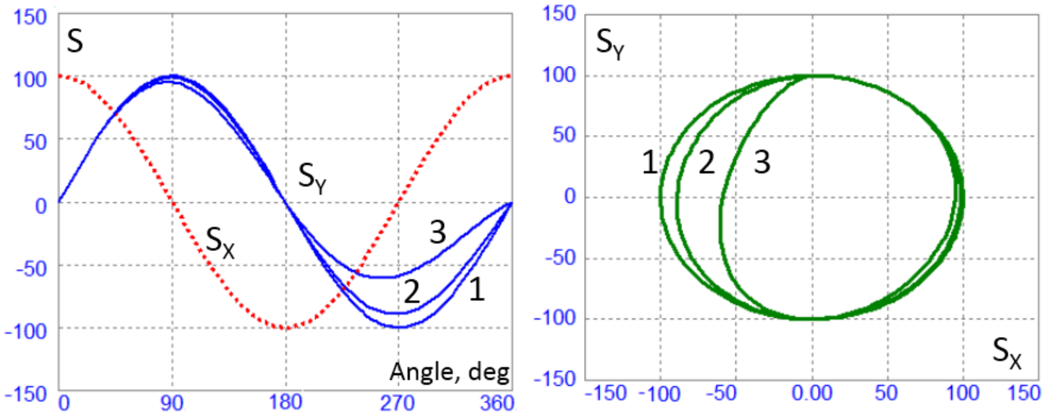

a) b)

Fig. 2.20. Sample simulation results.

The parameters of the presented SHS model can be corrected according to the experimental results. The simulation results are useful for the development and optimization of SHS calibration techniques.

2.8. Summary for Chapter 2

The new design of 3-D magnetic sensors based on SHS is presented in the chapter. Combining current flows in such sensors, one measures voltages upon which one then calculates projections B_X, B_Y, and B_Z of the magnetic flux density vector. The proposed 3-D sensor includes a traditional Hall sensor whose sensitivity axis (Z) is perpendicular to the semiconductor layer plane and two vertical SHSs whose sensitivity axes, X and Y correspondingly, are parallel to this plane. In contrast to known solutions, the potential (Hall) electrodes of the vertical SHSs are formed in the intermediate area between the semiconductor layer and the dielectric substrate and not on the surface of the semiconductor layer. Due to this solution, such sensors can be manufactured by traditional thin-film technology.

In comparison to the known 3-D magnetic field sensors, the developed sensors on SHS are characterized by two principal differences. First, in the new sensors on SHS, radiation-resistant semiconductors are used. Second, designs of such sensors do not require p-n junctions isolation with low radiation resistance. These differences provided high radiation resistance of the developed sensors.

A SPICE model of the 3-D magnetic sensor based on SHS has been developed. The model incorporates controlled voltage sources for simulation of Hall voltages and controlled resistive components for modeling the magnetoresistive modulation of the structure ohmic areas. The functional relationships between the parameters of the Hall sensors and the magnetic flux density vector projections are implemented by formal analogs and described by trigonometric functional dependencies, including those existing between the Hall and ohmic signal components and the sensor tilt angle in the magnetic field.

3. METHODS OF IN-SITU CALIBRATION AND DATA FUSION BASED ON INTEGRATED MAGNETOMETRIC TRANSDUCER.

3.1. Overview of topics on in-situ calibration technique

The true value of a physical quantity can never be determined exactly with one measurement. Errors of measurement should be minimized by specific methods of calibration and data processing, for example, as are presented in up-to-date books [1, 2]. The main approaches and advantages of in-situ calibration in common aspects are presented, as an example, in the chapter “Advantages of in-situ Calibration” of the book [3].

Most recent results in this field may be shown by the following topics: multimodal mechanical stimuli stage for in-situ calibration of MEMS gyroscopes [4], accurate pH measurement and determination in deep-sea environments by an in-situ pH sensor calibration device [5], development of in-situ microbial analyzer and internal standard calibration method [6], in-situ calibration of accelerometers in body-worn sensors using quiescent gravity [7], research on in-situ calibration technology of six-dimension force sensor for the LIDM docking performance test-bed [8], in-situ calibration to account for transmission losses in backscatter coefficient estimation [9], verifying Aquarius radiometer calibration drift using in situ data [10], improvements in the integration of lidar and photogrammetric datasets by in-situ camera calibration [11], rapid automatic high-precision in-situ wavelength calibration for tunable lasers [12], improved permittivity calibration method for wideband in-situ permittivity probe [13], in-situ array calibration for synthetic aperture sonar [14].

Some recent examples of in-situ calibration techniques in harsh radiation conditions are as follows: N42.28-2002 – American national standard calibration of germanium detectors for in-situ gamma-ray measurements [15], in-situ cross-calibration of in-core thermocouples in fast breeder test reactor [16], over-the-air array calibration of mmWave phased array in beam-steering mode based on measured complex signals [17].

This chapter addresses the problems of developing magnetic field measurement transducers' in-situ calibration in harsh radiation conditions. Presented in the chapter in-situ calibration methods and magnetic field measurement transducers are considered within the data fusion concept that recently emerged in information technologies [18]. In general, data fusion means combining multiple data sources to obtain more accurate, consistent, and valuable information than any individual data source can provide [19]. Data fusion techniques are typically used in prognostics systems [20], smart ubiquitous environments including Internet of Things (IoT) [21], navigation systems [22], image processing systems, particularly medical imaging [23], human-machine interface devices, and diagnostics devices including brain-computer interface [24], etc.

In sensor engineering, the data fusion concept gave rise to sensor data fusion or, for brevity, sensor fusion. This term mainly refers to heterogeneous sensor data fusion, i.e. fusion of data from integrated heterogeneous sensors. The latter are information sources that exploit different measurement techniques [25]. Among the main research topics in this area, one should mention multisensor data fusion algorithms [26], analysis of judicious fusion of inconsistent data obtained from integrated sensors [27], algorithms and unified framework for integrated sensors [28], etc. Some sample modern data fusion solutions include but are not limited to navigation systems [29], human activity monitoring [30], allergens detection and study [31].

In this chapter, the above-mentioned problem of magnetic field measurement transducers' in-situ calibration in harsh radiation conditions is solved by data and sensor fusion techniques on the integration of galvanomagnetic transducers (Hall effect transducers, Hall sensor) with induction transducers (induction coil sensor, magnetic loop sensors, search coils, pickup coils).

A wide range of aspects of design and applications of induction transducers are presented in recent publications: miniaturization design on magnetic induction sensors [32], high sensitivity and wide range soft magnetic tactile sensor based on electromagnetic induction [33], differential electromagnetic induction sensor using a spinning magnet excitation [34], development of compatible induction coil with pure ac for hall effect sensor: a study on metal materials thickness [35], close-range electromagnetic tracking of pulse induction search coils for subsurface sensing [36].

The authors' main results on the mentioned topics of in-situ calibration and data fusion in magnetic field measurement integrated galvanomagnetic and induction transducers for harsh radiation conditions are presented in our publication [37, 38] and patents [39, 40]. This chapter briefly summarizes these results.

3.2. Method # 1

The periodical in-situ calibration within Method #1 is performed when a change of a magnetic field to be measured exceeds a previously given value during some predetermined time interval. Such a method is called in-situ calibration in a quasi-stationary magnetic field.

The example of the time dependence of induction B of a quasi-stationary magnetic field to be measured is shown in the upper diagram of Fig. 3.1. It shows the induction changes ΔB_0 of the quasi-stationary magnetic field to be measured corresponding to the time intervals $\Delta t = t_2 - t_1$, at increase and decrease of magnetic field induction B. According to Method # 1, these induction changes ΔB_0 of the quasi-stationary magnetic field to be measured are used for calibrating galvanomagnetic transducer sensitivity directly in the process of magnetic field measurement.

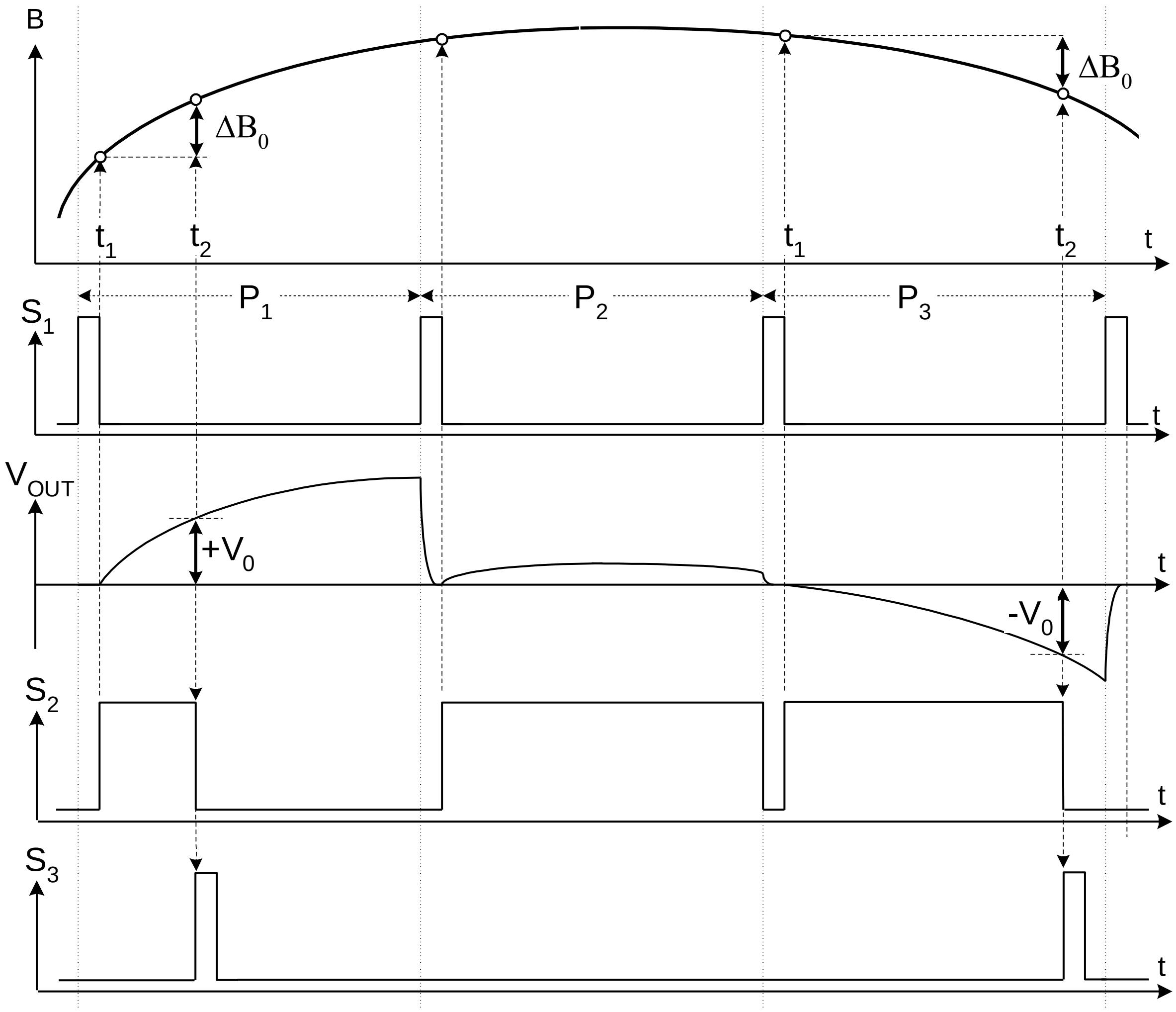

Fig.3.1. Time diagrams of the magnetic field induction and signals.

Galvanomagnetic transducer calibration includes coefficient K$_B$ determination, which determines the transducer's sensitivity and binds its V$_H$ output voltage with magnetic field induction B by the following equation:

$$V_H = K_B \cdot B \tag{3.1}$$

The galvanomagnetic transducer transduction function at its linear approximation is shown in Fig. 3.2. Coefficient K$_B$ is given by the formula as follows:

$$K_B = \frac{\Delta V_{H0}}{\Delta B_0}, \tag{3.2}$$

where $\Delta V_{H0} = V_H(t_2) - V_H(t_1)$ is a difference between the output voltages $V_H(t_1)$ and $V_H(t_2)$ of the galvanomagnetic transducer on boundaries of $\Delta t = t_2 - t_1$ time interval. By using K$_B$ coefficient defined in this way and using equation (1), the magnetic field induction B_M is calculated for any *t* point of time (Fig. 3.2) in accordance with the defined galvanomagnetic transducer output voltage ΔV_{HX}.

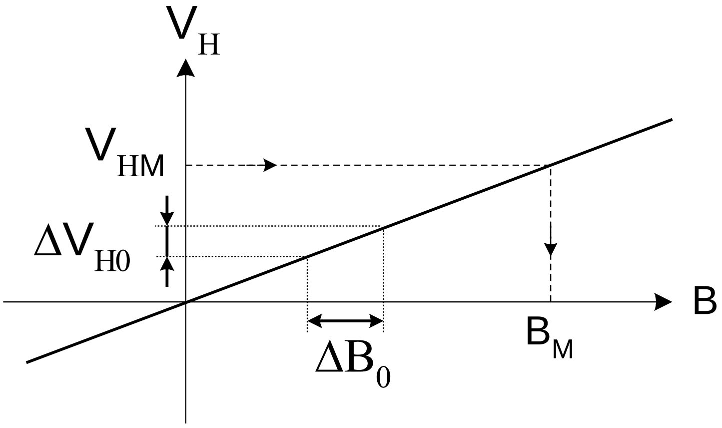

Fig.3.2. The transduction linear approximation of the galvanomagnetic transducer.

According to Method # 1, the induction change ΔB_0 of the quasi-stationary magnetic field to be measured is measured by a magnetic field induction sensor, which is usually comprised of coil 2 located in the magnetic field to be measured.

Voltage V_{COIL} on coil 2 outputs is proportional to the effective area A of its loops and the rate of change perpendicular to A area of magnetic field B induction vector component:

$$V_{COIL} = K_C \cdot \frac{dB}{dt}, \tag{3.3}$$

where K_C is the coefficient of proportionality.

According to Method # 1, the change of induction of a magnetic field to be measured is determined by the integration of the measured induction field transducer output voltage by the formula

$$V_{OUT} = K_C \cdot \frac{A}{\tau} \cdot \Delta B, \tag{3.4}$$

where τ is a time interval during which the integration takes place.

Since for calibration of galvanomagnetic transducer 1, it is necessary to determine the value of changes of magnetic field induction ΔB to be measured exactly in the area of galvanomagnetic transducer 1 allocation, this transducer is allocated inside coil 2 of the induction field transducer.

The proposed quasi-stationary magnetic field measurement method can be embodied in the device for quasi-stationary magnetic field measurement, the block diagram of which is shown in Fig. 3.3. This device is comprised of galvanomagnetic transducer 1 in the form of Hall transducer, magnetic field induction transducer coil 2, driver 3, which is connected to galvanomagnetic transducer 1 and provides its operating, time discriminator 4, which is connected to coil 2 and determines time intervals, in which magnetic field change reached the value known in advance, on-line data storage 5, which is controlled by time discriminator 4 and stores the results of driver 3 output voltage measurement, and corrector 6, which is controlled by time discriminator 4 and provides device periodical calibration according to the proposed method.

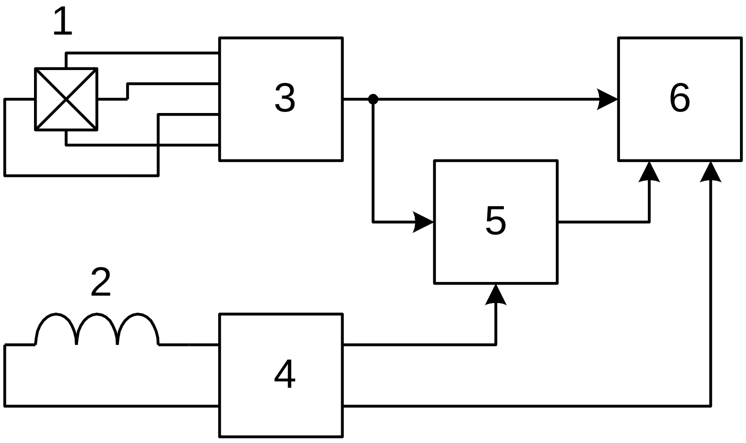

Fig.3.3. A block diagram of the device for magnetic field measurement.

Galvanomagnetic transducer 1 is located inside coil 2 of the magnetic field induction transducer (Fig. 3.4). The galvanomagnetic transducer 1 sensitivity axis (in particular, normal N to Hall transducer area) coincides with the coil 2 axis. Consequently, the measurement of magnetic field induction changes is provided by an induction transducer in the same section of the field in which the magnetic field induction is being measured using the Hall transducer.

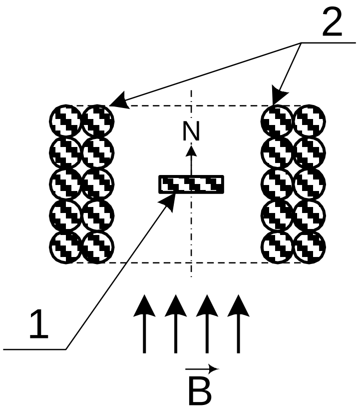

Fig.3.4. The position of galvanomagnetic transducer 1 in coil 2.

Only galvanomagnetic transducer 1 and coil 2 of magnetic field induction transducer are allocated in the area of magnetic field measurement under extreme operating conditions. The other elements of the magnetic field measurement device are located out of the extreme operation conditions area, which prevents the influence of destabilization factors existing in the area of extreme operating conditions.

Magnetic field measurement is performed by galvanomagnetic transducer 1 (Hall transducer). Driver 3 provides galvanomagnetic transducer signal formation and is comprised of a galvanomagnetic transducer current supply stabilizer, amplifier and analog-digital converter.

To simplify the disclosure of Method # 1 let us use a linear approximation of the transduction function of the magnetic field measurement device with the Hall transducer as a galvanomagnetic transducer. Then driver's output voltage V_H can be described as follows:

$$V_H = K_H \cdot K_A \cdot I_H \cdot B, \tag{3.5}$$

where K_H is the magnetic sensitivity of the Hall transducer; K_A is a coefficient of signal transformation by the driver; I_H is the Hall transducer supply current; B is the magnetic field induction vector component, which is perpendicular to the Hall transducer area.

In the process of long-term exploitation of the magnetic field measurement device under extreme operating conditions, the galvanomagnetic transducer magnetic sensitivity K_H is being changed, which is followed by measurement inaccuracy. In the general case, destabilization sources could be the transformation coefficient K_A and supply current I_H. That is why galvanomagnetic transducer calibration provides for the determination of single coefficient K_B, which binds output voltage V_H with magnetic field induction according to formula (1).

Time discriminator 4 determines the time interval, on the boundaries of which the magnetic field change, measured by means of coil 2, reaches the given value ΔB_0. According to Method # 1, voltage V_{COIL} from magnetic field induction transducer coil 2 is applied to the input of time discriminator 4, and the output of time discriminator 4 controls the operation of on-line data storage 5 and corrector 6 of this device.

A possible variant of the time discriminator 4 layout and its links with other elements of the device are shown in Fig. 3.5. Such a time discriminator is comprised of an integrator, which has operating amplifier OA1, resistor R, capacitor C and switch SW, two comparators on operational amplifiers OA2, OA3, logical element LE and timer TM.

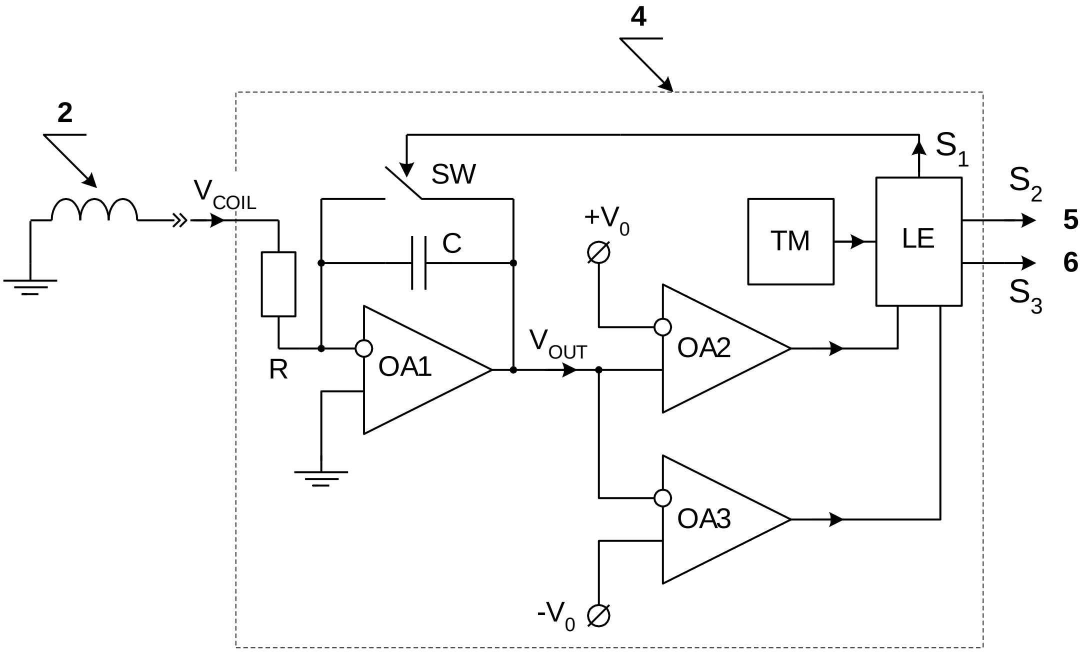

Fig.3.5. Time discriminator layout.

Voltage V_{OUT} on integrator output is described by formula (4), where $\tau = R \cdot C$ is the integrator time constant. So the magnetic field induction transducer coil 2 and integrator provide magnetic field induction change measurement, the result of which is almost independent of destabilization factors, in particular, high penetrating radiation level and temperature. It must be emphasized that a possible change of electro-physical parameters of coil 2 wire has no effect on the signal in any way. According to formula (3), the signal, which is picked up from coil 2, is determined not by electrophysical parameters of wire, but only by its loops' effective area A, which is not affected by the radiation.

The time discriminator operation is demonstrated by time diagrams (Fig. 3.1), which show a time change of magnetic field induction B(t), integrator output voltage $V_{OUT}(t)$ and operating pulses S_1, S_2, S_3. Timer TM (Fig. 3.5) forms a sequence of synchronizing pulses $S_1(t)$, duration and sequence period of which are fixed $P_1 = P_2 = P_3 = \text{const}$. Synchronizing pulses $S_1(t)$ periodically turn on the switch SW, which resets the voltage on integrator output, $V_{OUT}(t_1) = 0$. Just after each synchronizing pulse termination (t_1) a periodical integration process starts (magnetic field measurement) and the rise-up edge of the pulse $S_2(t)$ is formed for controlling the on-line data storage. This pulse acts as a function of command, which selects and stores the output signal $V_H(t_1)$ of driver 3 of the galvanomagnetic transducer 1 in the on-line data storage. In most cases, this signal has already been formed digitally by the analog-digital converter of this driver. Thus, voltage $V_H(t)$ is recorded in the on-line data storage 5 and is an informative value of magnetic field induction $B(t_1)$, which is measured by means of galvanomagnetic transducer 1.

Further operation of the time discriminator depends on magnetic field B(t) change rate. In the case of a sufficiently fast change of magnetic field, the voltage V_{OUT} on integrator output will exceed one of the reference values $+V_0$ (for example, the first period P_1 in Fig. 3.1) or $-V_0$ (the third period P_3 in Fig. 3.1) before the start-up of the next synchronizing pulse. These reference values of voltage determine the threshold values of magnetic field change ΔB_0. In time point t_2, when the integrator output voltage is equal to one of the reference values $V_{OUT} = \mp V_0$, the drop of pulse $S_2(t)$ and the rise-up edge of the pulse $S_3(t)$ of corrector 6 control are formed (Fig. 3.1). During this time, output signal $V_H(t_2)$ of the galvanomagnetic transducer driver is measured and recorded in the on-line data storage.

Otherwise, when magnetic field change does not exceed the threshold value ΔB_0 before period termination (for example, second period P_2), synchronizing pulse $S_1(t)$ of the next period will be reset by the integrator. As the result, pulse $S_3(t)$ will not be formed. Thus, at minute magnetic field change, when integrator operating accuracy is low, the correction of the transduction function of the magnetic field measurement device is not performed according to Method # 1.

Corrector 6 (Fig. 3.3) calculates coefficient K_B, which binds a time interval $\Delta t = t_2 - t_1$, determined by the time discriminator in which magnetic field ΔB_0 change took place, with output voltages $V_H(t_1)$ and $V_H(t_2)$ of the galvanomagnetic transducer driver on the boundaries of this time interval, by the formula

$$K_B = \frac{V_H(t_2) - V_H(t_1)}{\Delta B_0}. \tag{3.6}$$

Taking into consideration equation (3.4) and that during time Δt the magnetic field change is ΔB_0, coefficient K_B is described as

$$K_B = K_I \cdot \frac{A}{\tau} \cdot \frac{V_H(t_2) - V_H(t_1)}{V_0}, \tag{3.7}$$

where V_0 is a value of the reference voltage of the time discriminator layout.

Then, by measuring the galvanomagnetic transducer driver voltage value V_{HM} in any time point and by using coefficient K_B, the calculation of magnetic field induction B_M is performed. In particular, at a linear approximation of the transduction function (Fig. 3.2), according to Method # 1 the measurement of magnetic field induction will result in the determination of the induction value:

$$B_M = \frac{V_{HM}}{K_B}. \tag{3.8}$$

At piecewise-linear approximation of the transduction function of the magnetic field measurement device, coefficient K_{Bj} is determined for each part j of the transduction function. At approximation of the transduction function by polynomials, a set of equations, in which, in particular, coefficient $K_B(B)$ dependence is represented as the first derivative dV_H/dB, is used for calculation.

3.3. Method # 2

The periodical in-situ calibration within Method #2 is performed by a group of interconnected induction transducers, at least in four stages of the measurement transformation. As an example, Fig. 3.6 shows the first induction transducer 1 conventionally placed in a magnetometric module, the second induction transducer 2 and galvanomagnetic transducer 3.

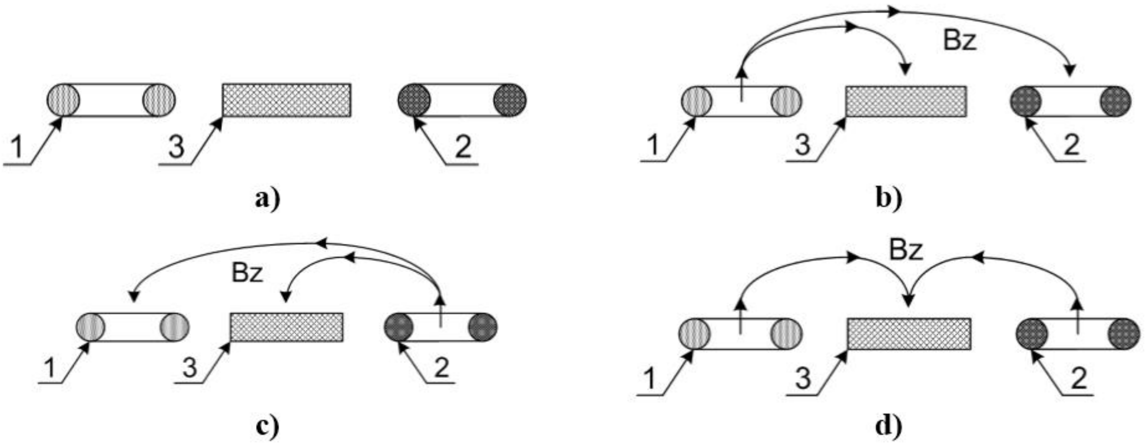

Fig.3.6. Calibration stages at Bx = 0.

The measurement of the magnetic field with the periodic calibration of the measuring transducer according to Method # 2 is carried out by the first induction transducer 1 (Fig. 3.6, a), by the second induction transducer 2, and by galvanomagnetic transducer 3, which constitute an integrated magnetometric module.

Depending on the stage of the measuring transformation, the induction transducers form the test magnetic field Bz or measure the change in the measuring magnetic field Bx. There is an interaction between the above-mentioned transducers of a functional module. Namely, the test magnetic field, which is formed by one of the induction transducers, affects the signals of another induction transducer and the galvanomagnetic transducer.

The magnetic flux through induction transducers, which are informative parameters of the change in the measured magnetic field, causes the formation of the electromotive force (voltage) on the leads of these induction transducers. This voltage is integrated over a period of time by the integrator whose signal is the result of measuring the change of the magnetic field during the integration. In addition, induction transducers can form a test magnetic field Bz, which occurs as a result of applying biasing voltage (current) to these transducers appropriately.

The magnetic field measurement by the galvanomagnetic transducer, in particular the Hall semiconductor transducer, is based on the measurement of the output voltage of this galvanomagnetic transducer and the subsequent calculation of the magnetic field induction using the known value of the sensitivity of the transducer. By applying biasing voltage (current) to the galvanomagnetic transducer the stream of charge carriers is created in it. Under the influence of the Lorentz force on a moving charge carrier in the galvanomagnetic transducer, a signal occurs, for example, the voltage difference on the output terminals of the Hall transducer. This voltage is an informative signal of the process of measuring the magnetic field.

Measurement of a magnetic field with a periodic calibration of a measuring transducer according to Method # 2 includes measurement of the output voltage of the galvanomagnetic transducer and the subsequent calculation of the induction of the measured magnetic field by the measured output voltage and the previously known sensitivity of the galvanomagnetic transducer. The indicated sensitivity is determined by periodically calibrating the galvanomagnetic transducer by establishing the relationship between the change in the magnetic field and the corresponding change in the output voltage of the galvanomagnetic transducer, and the calibration is carried out directly in the process of measuring the magnetic field.

The change in the magnetic field used for periodic calibration of the galvanomagnetic transducer is formed by a sequence of combinations of a previously unknown measuring magnetic field and a predetermined test magnetic field, with the formation of the test magnetic field and the measurement of the magnetic field change, carried out by at least two induction transducers, at least in four stages.

In the first stage of the measurement transformation (Fig. 3.6, b), the test magnetic field Bz is formed, say, by the first induction transducer 1, and the measurement of signals generated by this test magnetic field is carried out, for example, by the second induction transducer 2 and galvanomagnetic transducer 3.

In the second stage of the measurement transformation (Fig. 3.6, c), the test magnetic field Bz is formed by the aforementioned second induction transducer 2, and the measurements of the signals generated by this test magnetic field are carried out by the aforementioned first induction transducer 1 and galvanomagnetic transducer 3.

In the third stage of the measurement transformation (Fig. 3.6, d), the test magnetic field Bz is formed by the superposition of the magnetic fields of the above-mentioned first and second induction transducers, and the measurements of this superposition of magnetic fields are carried out by galvanomagnetic transducer 3.

In the fourth stage of the measurement transformation (Fig. 3.7, a), measuring magnetic field Bx is carried out by galvanomagnetic transducer 3 and two (first one 1 and second 2) induction transducers. The number of stages of the measurement transformation can be arbitrary with the superposition of the measuring Bx and the test Bz magnetic fields. Such superposition of the fields is shown in Fig. 3.7, b (test magnetic field Bz according to the first stage of the measurement transformation), Fig. 3.7, c (test magnetic field Bz according to the second stage of the measurement transformation), and Fig. 3.7, d (test magnetic field Bz according to the third stage of measuring transformation).

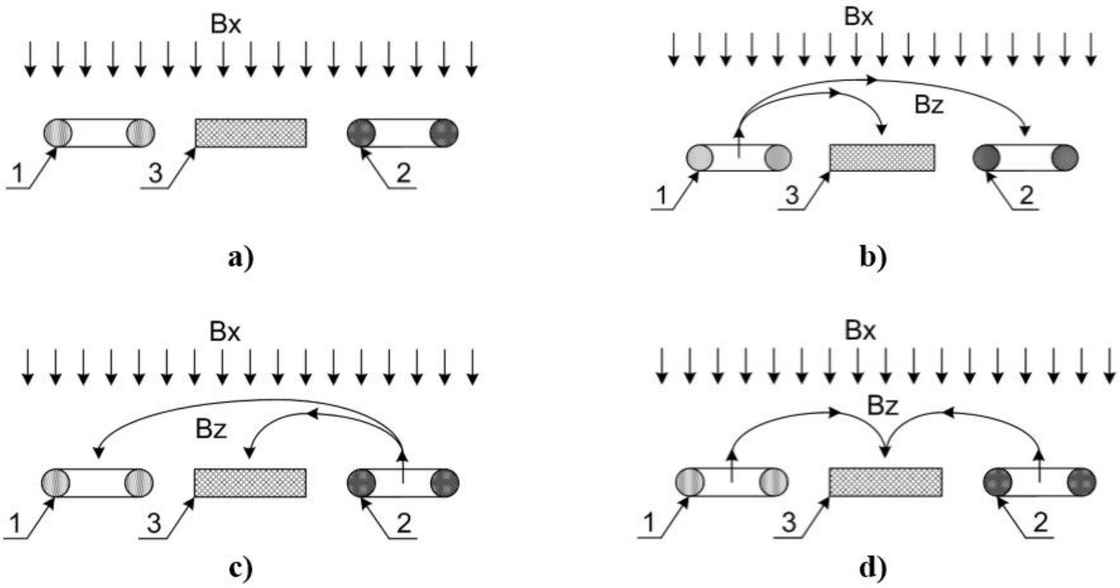

a) b) c) d)

Fig.3.7. Calibration stages at Bx = var.

Induction transducers are coils of metal wire, at least containing such coils and a number of auxiliary elements, in particular, a frame and leads (not shown in the figures). The coils of the induction transducers 1, 2 and the galvanomagnetic transducer 3 form a single functional magnetometric module whose design is optimized to provide the required calibration accuracy. In particular, as shown in Fig. 3.8, the coil of the first induction transducer 1 is formed in the coil of the second induction transducer 2, and galvanomagnetic transducer 3 is located inside the coil of the first induction transducer 1.

A prerequisite for the high accuracy of calibration is the presence of a significant effect of the test magnetic fields of the induction transducers on the signals of the galvanomagnetic transducer and the high temporal stability of such an action. This prerequisite is provided by the corresponding parameters of the coils of the induction transducers, in particular, the diameter of the coils, the number of turns and the power supply, the mutual spatial arrangement of the coils and the galvanomagnetic transducer, the mechanical and temperature stability of the design of the functional magnetometric module, etc.

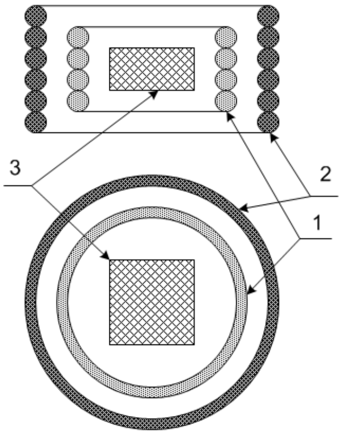

Fig.3.8. Components of the integrated magnetometric module in Method #2.

According to Method # 2, an increase in the accuracy of the measurement of a magnetic field with a periodic calibration of a measuring transducer is achieved by the formation and use of an appropriate sequence of test signals. The latter are caused both by changes in the induction of the measured magnetic field and by the test magnetic field generated by induction transducers. In particular, if the rate of change in the measuring magnetic field is too slow or too fast for the formation of qualitative signals of integrators, only the test magnetic fields of induction transducers are used, or the superposition of these test magnetic fields with a measuring magnetic field.

In addition, using such superpositions of magnetic fields, one can detect measurement errors due to the signal lines between the signal transducer (in particular, an integrator) and a functional magnetometric module. Then, taking into account the determined errors, one carries out the correction of the measurement results, and, therefore, increases the measurement accuracy.

3.4. Method #3

The objective of Method # 3 is to improve the accuracy of magnetic field measuring by in-situ calibration of a galvanomagnetic transducer with output voltage off-set cancelation technique. In this case, the galvanomagnetic transducer with two pairs of leads provides measurement in two stages. At the first stage, the first pair of leads is used to supply power to the galvanomagnetic transducer, while the other pair is used to measure the output voltage. At the second stage, the first pair of leads is used to measure the output voltage, and the other pair is used to supply power to the galvanomagnetic transducer.

Herewith, the accuracy is improved due to periodical calibration of the galvanomagnetic transducer while measuring the magnetic field using for this calibration at least two values of output voltage, the first being provided by the action of the measured magnetic field only, whereas the other represents the sum of the measured magnetic field and test field, whose value is given in advance.

The objective is achieved by a combination of galvanomagnetic transducer output voltage forming caused by the measured B_X magnetic field at the first (Fig. 3.9, a) and the second stages (Fig. 3.9, b), as well as, by the sum of the measured B_X and test B_R magnetic fields at the first stage (Fig. 3.9, c) and at the second stage (Fig. 3.9, d).

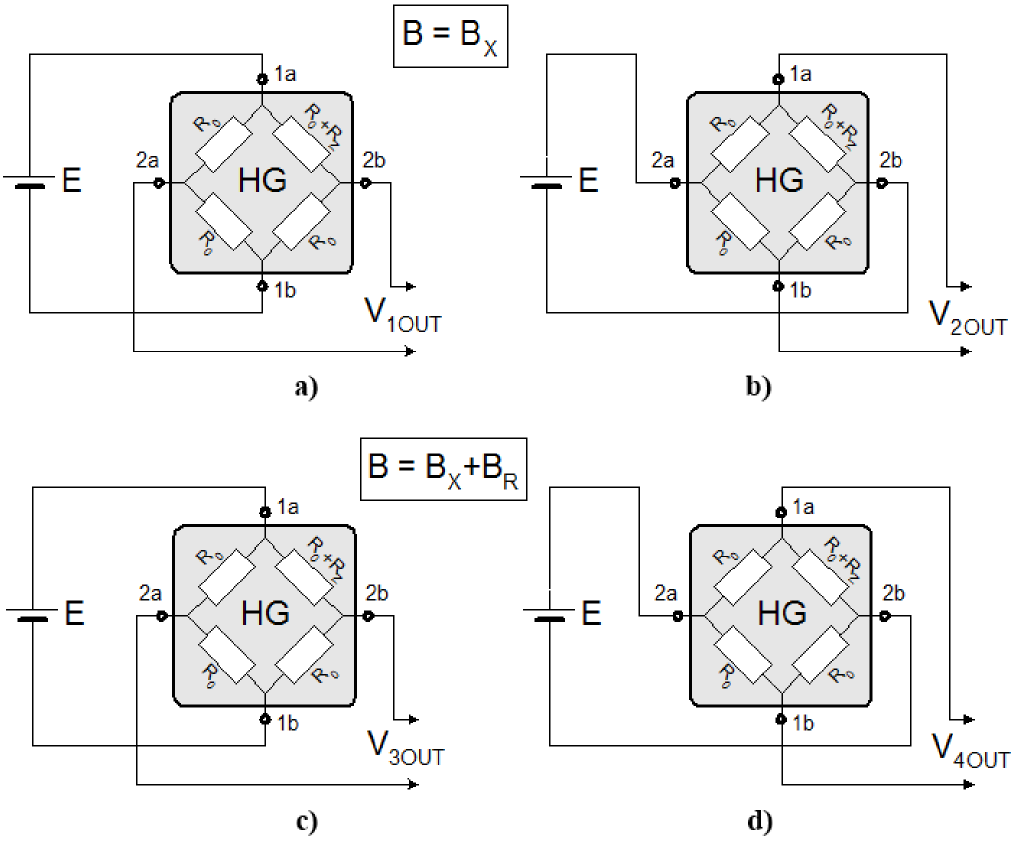

a) b) c) d)

Fig.3.9. Stages of forming the output voltage.

The galvanomagnetic transducer (HG) is a rectangular semiconductor structure that has two pairs of leads: the first pair – leads 1a, 1b, and the other pair – leads 2a, 2b. These transducers operate on the principle of charge carrier deflection under the action of Lorentz force, and the discrepancy between their output voltages is caused by the Hall effect.

The power supply to the HG transducer is through a voltage or current source (E). While supplying power to the HG transducer via leads 1a, 1b, output voltage V_{1OUT} is formed on leads 2a, 2b (Fig. 3.9, a). The equivalent scheme of the galvanomagnetic transducer is represented by resistors R_0 and R_Z, whereas resistance R_Z is included in the equivalent scheme for describing the non-symmetric nature of the transducer. The structure of the ideal galvanomagnetic transducer is symmetric, which meets the condition of $R_Z = 0$. If there is no magnetic field (B = 0), the output voltage of the ideal HG transducer is zero $V_{OUT} \cdot (B = 0) = 0$.

However, the existing transducers do not have the ideal symmetry, which is caused, in particular, by the uneven distribution of admixtures in the semiconductor material of which the transducer was made, deviation in the structure size, anisotropy, etc. The availability of resistance R_Z, which represents the total influence of the above effects on the output voltage, leads to the formation of the residual voltage $V_{OUT}(B = 0) = V_{RZ}$.

Under the action of magnetic field B_X the output voltage V_{1OUT} of the galvanomagnetic transducer (Fig. 3.9, a) is approximately proportional to the magnetic field induction B_X, and under the availability of the residual voltage V_{RZ} it equals

$$V_{1OUT} = K_B \cdot B_X + V_{RZ}, \tag{3.9}$$

where K_B – sensitivity (proportion coefficient of the linear conversion function).

As seen from the scheme in Fig. 3.9, b, at the second stage of measuring the sign of the residual voltage V_{RZ} becomes the opposite, that is the output voltage of the galvanomagnetic transducer is

$$V_{2OUT} = K_B \cdot B_X + V_{RZ}. \tag{3.10}$$

The effect of the residual voltage V_{RZ} compensation is achieved by summing up the results of measurements of both stages

$$V_{1OUT} + V_{2OUT} = 2 \cdot K_B \cdot B_X. \tag{3.11}$$

Thus, the V_{RZ} residual voltage drift of the galvanomagnetic transducer, which occurs, in particular, under long-term radiation operation conditions of the transducer, does not affect the result of the above two-stage measurement. Nevertheless, the sensitivity drift K_B is still a problem, which does not enable achieving the required accuracy of magnetic field measuring.

This problem, complying with Method # 3, may be eliminated by the fact that sensitivity K_B of the galvanomagnetic transducer is found at least during one of the above stages by determining at least two values of output voltage, the first of which is caused by the measured magnetic field, while the other is caused by the sum of the measured magnetic field and test field, whose value is given in advance (Fig. 3.9, c, Fig. 3.9, d).

The result of measuring the output voltage caused by the sum of the measured B_X and test B_R magnetic fields while using the galvanomagnetic transducer according to the scheme of the first stage is

$$V_{3OUT} = K_B \cdot (B_X + B_R) + V_{RZ}. \tag{3.12}$$

Similarly, the output voltage under the scheme of the second stage is

$$V_{4OUT} = K_B \cdot (B_X + B_R) - V_{RZ}. \tag{3.13}$$

Using the results of the carried out measurements, it is possible to receive the following:

$$V_{3OUT} - V_{1OUT} = K_B \cdot B_R \tag{3.14}$$

$$V_{4OUT} - V_{2OUT} = K_B \cdot B_R \tag{3.15}$$

The sensitivity of the galvanomagnetic transducer is found by using equation (3.14) or (3.15)

$$K_B = \frac{V_{3OUT} - V_{1OUT}}{B_R} \tag{3.16}$$

The measurements of the output voltage of the galvanomagnetic transducer, caused by the sum of the measured B_X and test B_R magnetic fields, may be made by using a coil, which, together with the galvanomagnetic transducer, creates an integrated measuring probe and is placed in the magnetic field measurement area.

There are two ways of forming a test magnetic field.

Under the first way the value of the beforehand given test magnetic field B_R is achieved by supplying power to the coil at the given current. The magnitude of the magnetic field of the coil is determined by its geometrical dimensions, number of loops and the power supply current. Therefore, this test field does not depend on destabilizing radiation operation conditions and may be considered constant and given in advance.

The other way of creating the test magnetic field suggests that the measured field is a variable value. The change of the measured magnetic field is established with the use of the coil and serves as a test field B_R. Like in the above-mentioned first way, it is possible to ignore the impact of radiation conditions and the coil parameters. Consequently, a signal from the coil, with the use of which the magnitude of the test field B_R is determined, may be considered constant.

It should be noted that the use of the coil for measuring the change of the measured magnetic field that serves as the test value B_R is justified only under specific parameters of this field change. Thus, the coil, whose output voltage value is determined by the speed of the magnetic field change with time, does not enable measuring stable or quasi-stationary magnetic fields, and therefore, it may not replace the galvanomagnetic transducer in the proposed measurement method. Instead, the galvanomagnetic transducer has no limitations on measuring stable or quasi-stationary magnetic fields. However, the stability of its residual voltage and sensitivity to destabilizing, particularly, radiation operation conditions, are unsatisfactory.

This problem is solved by the proposed method for measuring the magnetic field, which enables combining residual voltage compensation on the one hand and calibration of the galvanomagnetic transducer sensitivity on the other hand. Consequently, the proposed method provides high accuracy of measuring magnetic field with the use of the galvanomagnetic transducer under long-term destabilizing operation conditions, for instance, under the action of high penetrating radiation.

Depending on operation conditions the method under discussion enables considerable improvement in the accuracy of measurements. In particular, under the radiation fluence of fast neutrons of 10^{18} cm^{-2} degradation of the galvanomagnetic transducer based on semiconductor material InSb leads to the increase of residual voltage by 5 times (particularly, for the standard sample of Hall transducer with V_{RZ} = 1 mV to V_{RZ} = 5 mV) and decrease of the sensitivity by 7 times (in particular, under K_B = 350 mV/T to K_B = 50 mV/T). It is evident that tolerance of the measurement made by the magnetic transducer with the use of the mentioned Hall transducer sample is within 75%, which means that it is possible to consider that measuring as a process becomes purposeless. Instead, the use of the proposed measurement method provides the offset voltage compensation to the rate of 0.1 mV and calibration of sensitivity with the tolerance of maximum ±0.25% (under 0.2% nonlinearity of conversion function K_B within the range of magnetic field 1T), which totally corresponds to the tolerance of magnetic field measuring of up to ± 0.3% (within the range of magnetic field from ± 0.03 T to ± 1 T).

3.5. Integrated magnetometric transducer and data processing

Based on the data fusion concept and previously described methods of in-situ calibration, a new type of magnetic field measurement unit, namely, Integrated Magnetometric Transducer (IMT), has been developed. IMT comprises a Hall sensor, a coil, and some auxiliary components (Fig. 3.10). The simple one-dimensional (1-D) and 3-D versions of IMT are presented in Fig. 3.11. IMP provides:

- direct measurement of magnetic field induction;
- temperature measurement by the coil resistance (as a copper thermoresistor);

- HG thermostatting by means of controllable heating of the coil;
- measurement of weak magnetic field induction by means of compensation method;
- formation and measurement of stationary test magnetic fields;
- formation and measurement of pulsed magnetic fields with high induction values;
- formation and measurement of differential test magnetic field;
- thermostatting with simultaneous measurement of magnetic fields;
- constant or pulsed periodical annealing of radiation defects.

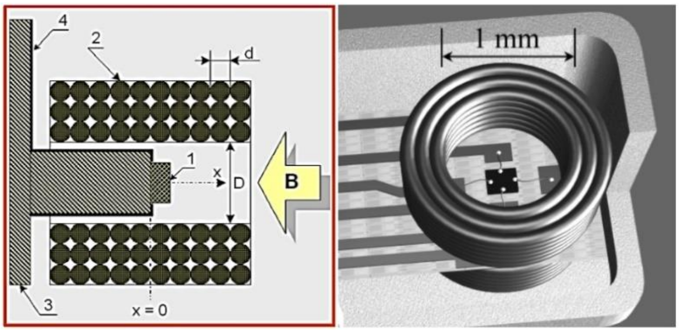

Fig.3.10. Integrated magnetometric transducer:
1 – Hall sensor, 2 – coil, 3 – base, 4 – outputs.

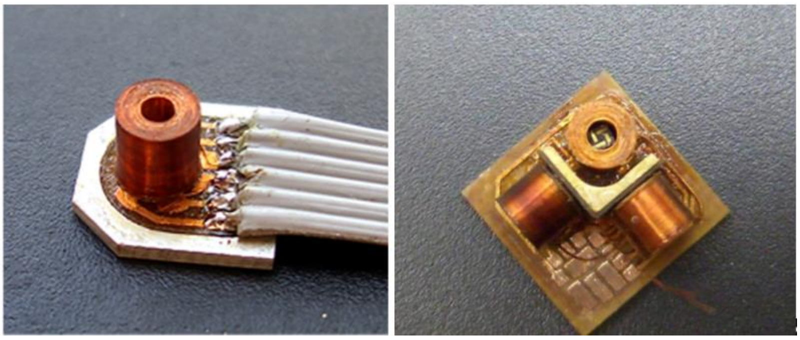

a) b)

Fig.3.11. IMT (a) and 3-D probe on IMT (b).

- The main approaches to IMT signals processing are as follows:
- simultaneous analysis of the transducing parameter by the integral and differential components of the signal;

- frequency separation of the integral and differential components of the signal;
- state-of-art calculation method within the data fusion concept.

Frequency separation of differential and integral components of the signal, which is the base of the given algorithm, is caused by the necessity of high measurement accuracy of the signal change (differential component) at the high value of the signal formed by the measuring field (integral component). Thus when measuring a change of the test field of the actuating coil with the induction of $\Delta B = 1$ mT at a relative measurement error of $\delta B = 10^{-3}$, device resolution should not be worse than $\Delta B_{min} = 1$ μT. Reaching such resolution and appropriate stability at magnetic field measurements up to 10 T presupposes providing the dynamic range of the signal in the measuring circuit not less than 140 dB.

It is obvious that such parameters are practically unachievable. The solution to the problem means the independent processing of differential and integral components of the signal. The simplest method of such separation is the processing of the integral components in the direct current circuit, and test one – in the frequency-selective circuit, when an alternate current frequency is set up in the actuating coil. In each of the tracks, a dynamic range of (70 ÷ 80) dB is provided, which allows obtaining the ratio of the maximum measuring field value B_{max} to the resolution by test field ΔB_{min} near (140 ÷ 160) dB.

Depending on measurement accuracy let us consider the transducing function as a linear relationship, polynomial one, or mathematical model which links Hall voltage with electrophysical and design parameters.

Taking into account the rather good linearity of transducing function, the function derivative may be considered a constant value in all measuring ranges with an error within 0.1÷5.0 %. Then the problem of determining the transducing function, which could drift during long-term operation under hard radiation, is reduced to the measurement of curvature $S = \Delta U_H / \Delta B$, where ΔU_H is the Hall voltage change, caused by the test field with induction ΔB. In the case of analogous signal processing, an efficient method is a correction of HG operating current in such a way that the ratio $\Delta U_H / \Delta B$ is constant during all measurements.

The use of polynomial representation of the transducing function allows one to improve the measurement accuracy considerably. It is expected that transducing function

$$U_{H_0} = \sum_{j=0}^{n} \alpha_j \cdot B^j \tag{3.17}$$

(α_j are the coefficients of the polynomial series) drifts almost linearly ($U_{H_e} = G \cdot U_{H_0}$, where G is the factor of proportionality). The transducing function and quantities to be measured are presented in Fig. 3.12.

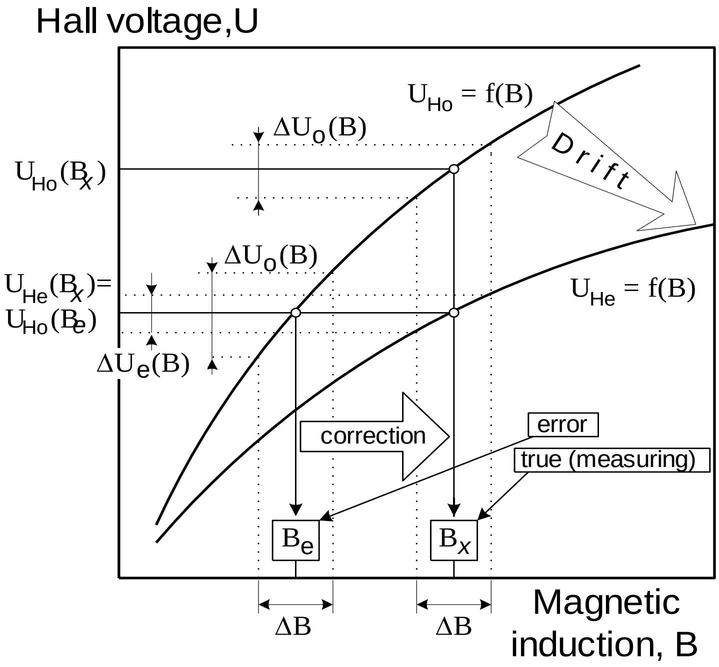

Fig.3.12. Transducing function correction.

If the change value $\Delta U_0 / \Delta B$ of the measured voltage in the point of $U_{H_e}(B_X)$ is equal to the nominal function derivative in this point, then the HG parameter is constant. But, as one may see in Fig. 3.12, when the transducing function drifts, its change value is not constant too: $\Delta U_e / \Delta B \neq \Delta U_0 / \Delta B$.

Having determined the transducing function derivative

$$\frac{dU_{H_e}}{dB} = \frac{d(G \cdot U_{H_0})}{dB} = G \cdot \frac{dU_{H_0}}{dB} = G \cdot \sum_{j=1}^{n} j \cdot \alpha_j \cdot B^{j-1} \tag{3.18}$$

and taking into account condition

$$\lim_{\Delta B \to 0} \frac{\Delta U_H}{\Delta B} = \frac{dU_H}{dB},$$

let us write the system of equations for linear scaling:

$$\begin{cases} U_{H_e}(B_X) = G \cdot U_{H_0}(B_X) \\ \frac{dU_{H_e}(B_X)}{dB} = G \cdot \frac{dU_{H_0}(B_X)}{dB} \end{cases} \tag{3.19}$$

After appropriate transformations we receive

$$U_{H_e}(B_X) \cdot \sum_{j=1}^{n} j \cdot \alpha_j \cdot B^{j-1} = \frac{\Delta U_e(B_X)}{\Delta B} \cdot \sum_{j=0}^{n} \alpha_j \cdot B^j \tag{3.20}$$

In order to solve (20) for B_x with known values of integral $U_{He}(B_x)$ and differential $\Delta U_e(B_x)$ signal components and given actuating field value $\Delta B=const$, let us apply Newton iteration method.

Let us transform (20) to the equation $f(B)=0$:

$$f(B) = \overline{U_H} \cdot \sum_{j=0}^{n} \alpha_j \cdot B^j - \sum_{j=1}^{n} j \cdot \alpha_j \cdot B^{j-1} = 0 \tag{3.21}$$

where $\overline{U_H} = \frac{\Delta U_e(B_X)}{U_{H_e}(B_X)} \cdot \frac{1}{\Delta B}$ is the normalized value of the signal.

Taking into account that at the [B_e, B_x] interval

$$\frac{d^2 \cdot f(B)}{dB^2} \neq 0 \text{ and } f(B_e) \cdot \frac{d^2 \cdot f(B_e)}{dB^2} > 0,$$

the root is determined by $B_m = B_{m-1} - \frac{f(B_{m-1})}{df(B_{m-1})/dB}$ iteration.

As the initial iteration root, we take $B_1=B_e$, which is determined without correction. Therefore the second iteration root is

$$B_2 = b_e - \frac{\overline{U_H} \cdot \sum_{j=0}^{n} \alpha_j \cdot B^j - \sum_{j=1}^{n} j \cdot \alpha_j \cdot B^{j-1}}{\overline{U_H} \cdot \sum_{j=1}^{n} j \cdot \alpha_j \cdot B^{j-1} - \sum_{j=2}^{n} j \cdot (j-1) \cdot \alpha_j \cdot B^{j-2}} \tag{3.22}$$

The iteration process continues until the condition $|B_X - B_{m-1}|/B_m < \delta B$ is satisfied, where δB is the relative error of the measurement. The calculation result will be the true value of the field induction measured $B_X = B_m$. As it has resulted from the investigations carried out, the error of the presented algorithm is in the range of 0.05% ÷ 0.1% and depends on the drift value when operating under radiation conditions.

3.6. Summary for Chapter 3

Three new methods of magnetic field measurement transducers' in-situ calibration in harsh radiation conditions are described. Based on these methods and the data fusion concept the new type of magnetic field measurement unit – Integrated Magnetometric Transducer (IMT) – has been developed. IMT comprises a Hall sensor, one or more coils, and some construction components.

The periodical in-situ calibration within Method #1 is performed when a change of a magnetic field to be measured exceeds a previously given value during some predetermined time interval. In-situ calibration within Method #2 is performed in some stages of the measurement by a group of interconnected induction transducers. Method # 3 is aimed at improving the accuracy of magnetic field measuring by in-situ calibration of galvanomagnetic transducer with output voltage off-set cancelation technique.

An increase in the accuracy of the measurement with a periodic calibration of a measuring transducer is achieved by the formation and use of an appropriate sequence of test signals, which are caused both by changes in the induction of the measured magnetic field and by the generated induction transducers of the test magnetic field. In particular, if the rate of change in the measuring magnetic field is too slow or too fast for the formation of qualitative signals of integrators, only the test magnetic fields of induction transducers are used, or the superposition of these test magnetic fields with a measuring magnetic field.

The main approaches to IMT signals processing comprise simultaneous analysis of the transducing parameter by integral and differential components of the signal, frequency separation of integral and differential components of the signal, as well as state-of-art calculation method within the data fusion concept.

4. MAGNETIC MEASURING INSTRUMENTATION FOR HARSH RADIATION CONDITIONS

4.1. Overview of topics on measuring instrumentation for harsh radiation conditions

In this chapter, a set of novel magnetic field measuring instrumentations on Hall sensors for harsh radiation conditions is presented. The set includes:

- RHP-ISC and RHP-WB instrumentations for plasma magnetic field monitoring in nuclear fusion reactors;
- RHP-MAP instrumentation for permanent cyclotron magnet magnetic field high precision mapping in charge particle accelerators;
- RHP-RAD instrumentation for testing sensors directly during their irradiation.

Owing to its high temperature, nuclear fusion plasma cannot be confined directly to material vessels. The problem is obviated by using magnetic fields, which confine and thermally insulate the fuel, keeping it away from the vessel walls. Recent results in magnetic field measurements in nuclear fusion research may be shown by the following topics: comparison of two different techniques for long-term magnetic measurements in nuclear fusion research [1], approaches for magnetic sources reconstruction in controlled thermo-nuclear fusion technology [2], the plasma compression fusion device enabling nuclear fusion ignition [3], evaluation of positional stability in active magnetic levitation using spherical HTS bulk for inertial nuclear fusion [4], fast identification problems in 3-D iron core fusion devices [5].

Development of magnetic field measuring instrumentations for JET (Joint European Torus) and ITER (International Thermonuclear Experimental Reactor) reactors are presented, for example, in the publications: real-time systems in JET tokamak [6], flexible system for the control of external magnetic perturbations in the JET tokamak [7], electromagnetic analysis of the 3-D effects of the metallic structures in JET tokamak [8], recent improvement of the design of the ITER steady-state magnetic sensors [9], progress in the design and testing of in-vessel magnetic pickup coils for ITER [10], axisymmetric magnetic control in ITER [11].

Magnetic field mapping is the development of maps or images of magnetic fields in space. Magnetic field maps are needed for designing and optimizing magnets used in particle accelerators. Development of instrumentation for magnetic field mapping may be observed, for example, by topics: a study on magnetic field mapping method in the center volume of the air-core solenoid [12], magnetic navigation system utilizing a closed magnetic circuit to maximize magnetic field and a mapping method to precisely control magnetic field in real time [13], design and instrumentation of a magnetic field micro-probe mapper: an e-lab apparatus to map a coil's magnetic field [14], 3-D field mapping and active shimming of a screening-current-induced field in an HTS coil using harmonic analysis for high-resolution NMR magnets [15].

In cyclotron-type particle accelerators, these topics are presented in studies: radial magnetic field optimization of the 5 T superconducting cyclotron for medical application [16], magnetic field optimization and tolerance study of a medical superconducting cyclotron [17], the magnetic field design of HITFiL cyclotron [18].

A few recent studies and developments of instrumentations for testing materials and fusion reactor components in radiation conditions are the following: a new facility for combined-load testing of fusion reactor in-vessel components [19], construction of an in-situ radiation test system for semiconductor materials and devices based on a 4.5 MV accelerator [20], high-vacuum gamma irradiation facilities for synergistic effects testing on optoelectronic components and materials [21], material damage test for ILC collimators [22].

The authors' main results in the above-mentioned topics of measuring instrumentation for harsh radiation conditions are presented in our publication [23-30]. This chapter briefly summarizes these results.

4.2. RHP-ISC instrumentation

Magnetic measuring instrumentation with the in-situ calibration technique, which has been mentioned in the previous chapter and is further referred to as RHP-ISC instrumentation, has been developed for plasma magnetic field monitoring in nuclear fusion reactors. RHP-ISC consists of sets of radiation-stable 3D probes and an electronic unit (Fig. 4.1). Each 3D probe contains (Fig. 4.2, Fig. 4.3): 3 Hall sensors, 3 coils, and 1 thermo-diode. The Hall sensors generate output voltages V_{HGX}, V_{HGY}, and V_{HGZ}, which are proportional to the corresponding magnetic field induction components B_X, B_Y, and B_Z. The coils perform two functions. In pick-up mode, they generate voltages V_{CLX}, V_{CLY}, and V_{CLZ}, which are proportional to the corresponding magnetic field induction change rate components ΔB_X, ΔB_Y, and ΔB_Z. In calibration mode, the coils generate test magnetic fields B_{0X}, B_{0Y}, and B_{0Z} of approximately 5 mT at supply current of about 20 mA.

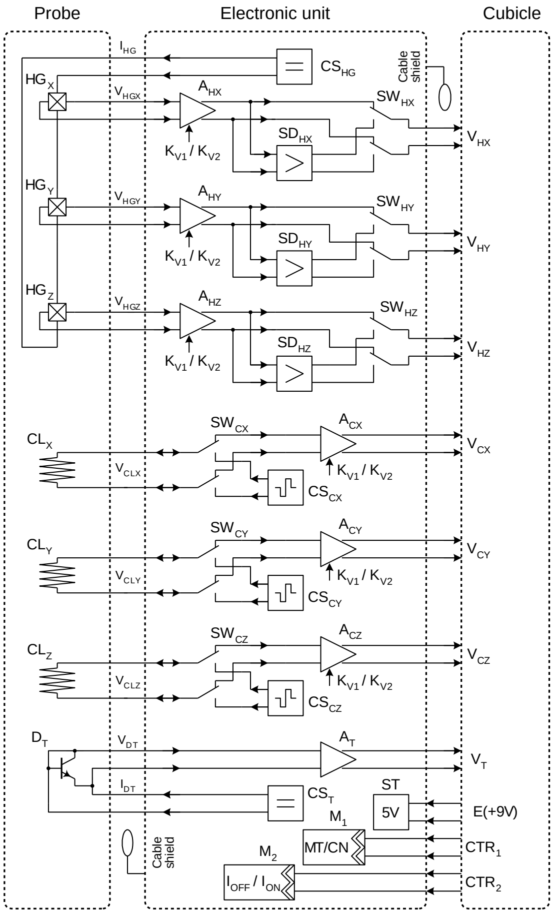

Fig. 4.1. The layout of RHP-ISC instrumentation.

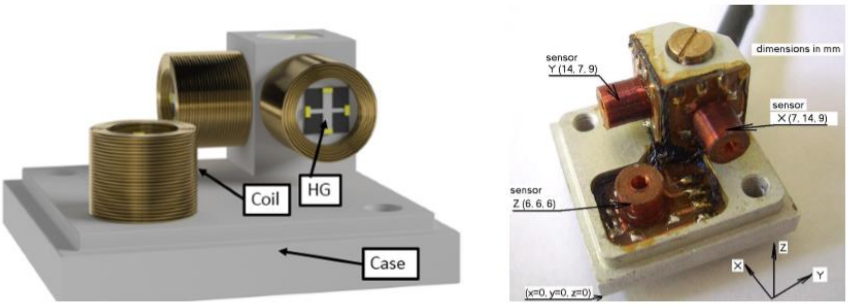

Fig. 4.2. The structure of the 3D probe.

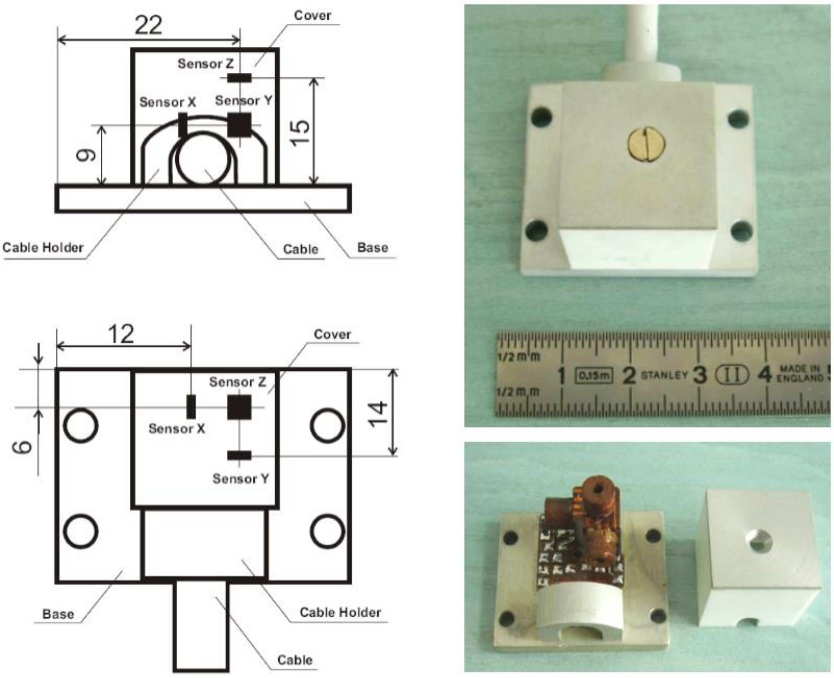

Fig. 4.3. The assembling of the 3D-probe.

This test magnetic field does not depend on the radiation dose, and thus it can be used for periodic determination of the Hall sensors' sensitivity. The thermodiode provides the possibility of the probe's temperature measurement in the range up to 100˚C, which gives the possibility of estimating magnetic fields taking into account temperature-induced changes of the parameters of the Hall sensors and coils.

The main parts of the electronic unit are:

- CS_{HG} – the source of DC supply current to the Hall sensors;

- CS_{CX}, CS_{CY}, CS_{CZ} – sources of AC supply current to the coils;
- CS_T – the source of DC current to the thermo-diode;
- A_{HX}, A_{HY}, A_{HZ} – differential amplifiers of the Hall sensor signals;
- A_{CX}, A_{CY}, A_{CZ} – differential amplifiers of the coil signals;
- A_T – differential amplifier of the thermo-diode signal;
- SD_{HX}, SD_{HY}, SD_{HZ} – synchronous detectors of the test field signals;
- SW_{HX}, SW_{HY}, SW_{HZ}, SW_{CX}, SW_{CY}, SW_{CZ} – switches of the operation modes;
- ST – supply voltage stabilizer +5 V;
- M_1 – controller of operation mode “Measurement – calibration”;
- M_2 – controller of the Hall sensors' power supply mode “ON–OFF”.

The electronic unit provides analog differential signals (voltages), which are then transmitted by twisted pairs into the next stage units for analog-to-digit conversion, filtering, data storage and presentation. The output signals of the electronic unit are:

- V_{HX}, V_{HZ}, V_{HZ} – differential voltages generated by the Hall sensors (B-Channel);
- V_{CX}, V_{CZ}, V_{CZ} – differential voltages generated by the coils (C-Channel);
- V_T – the differential voltage generated by the thermo-diode (T-Channel);

The differential voltage amplifiers V_{HX}, V_{HZ}, V_{HZ}, V_{CX}, V_{CZ}, and V_{CZ} have two amplification factors $K_{V1} = 10$ and $K_{V2} = 100$. The choice of the amplification factor is made independently for each amplifier with the help of mechanical switches located on the PCB of the electronic unit. This gives the possibility of choosing one out of two magnetic field measurement ranges: for instance, the first one – $B < 0.2$ T, the second one – $B < 2$ T.

Control over the electronic unit operation modes is provided by logic signals:

- CTR_1 – control over operation mode “Measurement – calibration”;
- CTR_2 – control over the Hall sensors' power supply “ON–OFF”.

The electronic unit has two modes of operation:

- "Measurement" – CTR_1 = Low;
- "Calibration" – CTR_1 = High.

The possibility of controlling the Hall sensors' supply current is provided for:

- "I_{HG}-OFF" – CTR_2 = Low;
- "I_{HG}-ON" – CTR_2 = High.

In "Measurement" mode (B-Channel), three components of the magnetic field induction B_X, B_Y, and B_Z are measured online at the frequency of analog-digital conversion of 10 kHz. Output voltages of the electronic unit serve as information signals for this mode:

$$V_{HMX} = V_{HGX} \cdot K_{V_i}, \qquad V_{HMY} = V_{HGY} \cdot K_{V_i}, \qquad V_{HMZ} = V_{HGZ} \cdot K_{V_i}$$

where $V_{HGX}, V_{HGY}, V_{HGZ}$ – Hall sensors' output voltages; K_{V_i} – amplification factors of differential amplifiers A_{HX}, A_{HY}, A_{HZ}.

Besides, the values of the magnetic field change ΔB_X, ΔB_Y, ΔB_Z (optional), whose information signals are the output voltages of the electronic unit, are measured:

$$V_{CX} = V_{CLX} \cdot K_{V_i}, \qquad V_{CY} = V_{CLY} \cdot K_{V_i}, \qquad V_{CZ} = V_{CLZ} \cdot K_{V_i}$$

where $V_{CLX}, V_{CLY}, V_{CLZ}$ – output voltages on the coil terminals in pick-up mode; K_{V_i} – amplification factors of differential amplifiers A_{CX}, A_{CY}, A_{CZ}.

"Calibration" mode (C-Channel) is meant for periodic determination of the sensitivity of the Hall sensors, whose parameters can partially drift during long-term exploitation in a radiation environment. Voltages are information signals for this mode:

$$V_{HCX} = V_{HGX}(B_{0X}) \cdot K_{VC}, \quad V_{HCY} = V_{HGY}(B_{0Y}) \cdot K_{VC}, \quad V_{HCZ} = V_{HGZ}(B_{0Z}) \cdot K_{VC}$$

where $V_{HGX}(B_{0X}), V_{HGY}(B_{0Y}), V_{HGZ}(B_{0Z})$ – the Hall sensors' output voltages at the test fields in coils of B_{0X}, B_{0Y}, B_{0Z}; K_{VC} – total factors of transmittance characterizing differential amplifiers A_{HX}, A_{HY}, A_{HZ} and synchronous detectors SD_{HX}, SD_{HY}, SD_{HZ}. The typical value is $K_{VC} \approx 1000$, which at $B_0 \approx 5$ mT and Hall sensor sensitivity of $S_B \approx 100$ mV/T provides the electronic unit's output signal of $V_{HCX} \approx V_{HCY} \approx V_{HCZ} \approx 0.5$ V.

In “Calibration” mode, the values of the external magnetic fields B_X, B_Y, and B_Z, at which such measurements are conducted, do not influence voltages V_{HCX}, V_{HCY}, V_{HCZ}; and this is of crucial importance. This condition is satisfied with the help of synchronous detectors separating the signals generated by the coils' AC test magnetic field from the signals generated by the DC external magnetic fields.

I_{HG}-OFF mode is determined for measuring the level of electromagnetic noise. In all the modes, the temperature is measured (T-Channel). Its information signal is voltage $V_T = V_{DT} \cdot K_{VT}$, where V_{DT} – voltage on thermo-diode D_T, K_{VT} – amplification factor of differential amplifier A_T.

The parameters of each set (3D-probe & Electronic Unit) are described by an array of 32 linear approximation coefficients (Table 4.1).

Table 4.1.

The calibration coefficient array for the 3D probe & Electronic Unit

3D probe & Electronic Unit #			
Parameter description		α	A_0
1	T-channel	α_T[#]	V_{T0}[#]
2	C-Channel X	α_C [#X]	V_{C0}[#X]
3	C-Channel Y	α_C [#Y]	V_{C0}[#Y]
4	C-Channel Z	α_C [#Z]	V_{C0}[#Z]
5	B-Channel X @ KL for V_0	$\alpha_{V0@L}$[#X]	$V_{00@L}$[#X]
6	B-Channel X @ KL for K_B	$\alpha_{KB@L}$[#X]	$K_{B0@L}$[#X]
7	B-Channel Y @ KL for V_0	$\alpha_{V0@L}$[#Y]	$V_{00@L}$[#Y]
8	B-Channel Y @ KL for K_B	$\alpha_{KB@L}$[#Y]	$K_{B0@L}$[#Y]
9	B-Channel Z @ KL for V_0	$\alpha_{V0@L}$[#Z]	$V_{00@L}$[#Z]
10	B-Channel Z @ KL for K_B	$\alpha_{KB@L}$[#Z]	$K_{B0@L}$[#Z]
11	B-Channel X @ KH for V_0	$\alpha_{V0@H}$[#X]	$V_{00@H}$[#X]
12	B-Channel X @ KH for K_B	$\alpha_{KB@H}$[#X]	$K_{B0@H}$[#X]
13	B-Channel Y @ KH for V_{0v}	$\alpha_{V0@H}$[#Y]	$V_{00@H}$[#Y]
14	B-Channel Y @ KH for K_B	$\alpha_{KB@H}$[#Y]	$K_{B0@H}$[#Y]
15	B-Channel Z @ KH for V_0	$\alpha_{V0@H}$[#Z]	$V_{00@H}$[#Z]
16	B-Channel Z @ KH for K_B	$\alpha_{KB@H}$[#Z]	$K_{B0@H}$[#Z]

Linear approximation of temperature dependencies

Temperature dependencies of A_{MT} values are approximated in the following way:

$$A_{MT} = A_{T0} \cdot (1 + \alpha_A \cdot T),$$

where A_{T0}, α_a are linear approximation coefficients; T is temperature in °C.

During the calibration process the coefficients A_{MT} and α_A are determined by measuring the value A_{MT} at two temperatures T_1, T_2 (for example, $T_1 = 25°C$, $T_2 = 100°C$):

$$\begin{cases} A_{MT1} = A_{T0} \cdot (1 + \alpha_A \cdot T_1) \\ A_{MT2} = A_{T0} \cdot (1 + \alpha_A \cdot T_1) \end{cases}$$

After conversion

$$\frac{A_{MT2}}{A_{MT1}} = \frac{1 + \alpha_A \cdot T_2}{1 + \alpha_A \cdot T_1}; \quad A_{MT2} + A_{MT2} \cdot \alpha_A \cdot T_1 = A_{MT1} + A_{MT1} \cdot \alpha_A \cdot T_2$$

we receive the formula for the calculation of linear approximation coefficients:

$$\alpha_A = \frac{A_{MT2} - A_{MT1}}{A_{MT1} \cdot T_2 - A_{MT2} \cdot T_1}; \quad A_{T0} = \frac{A_{MT1}}{1 + \alpha_A \cdot T_1}$$

Channels for temperature measurements (T-channel)

Calculation of temperature T_M of the probe is done by the following formula:

$$T_M = \frac{V_{TT} - V_{T0}}{V_{T0} \cdot \alpha_T} \tag{4.1}$$

where V_{TT} is the measured value of T-channel output voltage; V_{T0} and α_T are linear approximation coefficients.

During the calibration process the probe is located in the thermostat and the measurement of two output voltages V_{T1}, V_{T2} of the T-channel is done at two temperatures T_1, T_2 being determined by the reference thermometer

$$\begin{cases} V_{T1} = V_{T0} \cdot (1 + \alpha_T \cdot T_1) \\ V_{T2} = V_{T0} \cdot (1 + \alpha_T \cdot T_2) \end{cases}$$

Thus, the linear approximation coefficients are calculated

$$\alpha_T = \frac{V_{T2} - V_{T1}}{V_{T1} \cdot T_2 - V_{T2} \cdot T_1}; \quad V_{T0} = \frac{V_{T1}}{1 + \alpha_T \cdot T_1}$$

Further, the coefficients α_T and V_{T0} are used for the determination of the probe's temperature.

The channels for magnetic field measurements (B-channel)

The thermally compensated value of magnetic field induction B_R is calculated by the formula:

$$B_T = K_{BT} \cdot (V_M - V_{0T}), \tag{4.2}$$

where V_M is the measured value of B-channel output voltage (here and further the result of B-channel voltage measuring is a difference of two values, the first of which is measured at $I_{HG} => ON$, and the second at $I_{HG} => OFF$); K_{BT} is the temperature-dependent transduction coefficient; V_{0T} is the temperature-dependent value of the offset voltage value.

Temperature dependencies of K_{BT} and V_{0T} values are described as follows:

$$K_{BT} = K_{B0} \cdot (1 + \alpha_{V0} \cdot T_M); \tag{4.3}$$

$$V_{0T} = V_{00} \cdot (1 + \alpha_{V0} \cdot T_M), \tag{4.4}$$

where K_{B0}, α_{KB}, V_{00}, α_{V0} are linear approximation coefficients, being determined in the process of B-channel calibration; T_M is the measured value of the probe's temperature in °C.

The possibility to select one of the magnetic field measurement ranges ±2 T or ±0.2 T is provided by the corresponding selection of amplification coefficients K_L or K_H of output differential voltage of the electronic unit. That is why during calibration two sets of coefficients are being determined: $K_{B0@L}$, $\alpha_{KB@L}$, $V_{00@L}$, $\alpha_{V0@L}$ and $K_{B0@H}$, $\alpha_{KB@H}$, $V_{00@H}$, $\alpha_{V0@H}$.

The process of measurement of a magnetic field is fulfilled as follows:

b1) – the voltage V_{TN} of T-channel is measured and the temperature T_N is measured by formula (4.1);

b2) – the temperature-dependent value of B-channel transduction coefficient K_{BT} is calculated by formula (4.3);

b3) – the temperature-dependent value of B-channel offset voltage V_{0T} is calculated by formula (4.4);

b4) – the voltage V_M of B-channel is measured and then the real value B_R of magnetic field induction is calculated by formula (4.2).

During magnetic field measuring the optimal amplification coefficient (K_L or K_H) is selected, and for calculation the corresponding set of coefficients is applied.

The calibration process of B-channel is performed as follows:

k1) – the probe is located in a magnetic field null-chamber (B = 0);

k2) – the value of the offset voltage of B-channel V_{0T1} is measured at temperature T_{1B0} (for example T_{1B0} = 25°C) and the value of V_{0T2} is measured at temperature T_{2B0} (for example T_{2B0} = 100°C);

k3) – using the system of equations

$$\begin{cases} V_{0T1} = V_{00} \cdot (1 + \alpha_{V0} \cdot T_{1B0}) \\ V_{0T2} = V_{00} \cdot (1 + \alpha_{V0} \cdot T_{2B0}) \end{cases}$$

the linear approximation coefficients are calculated:

$$\alpha_{V0} = \frac{V_{0T2} - V_{0T1}}{V_{0T1} \cdot T_{2B0} - V_{0T2} \cdot T_{1B0}}; \quad V_{00} = \frac{V_{0T1}}{1 + \alpha_{V0} \cdot T_{1B0}}. \tag{4.5}$$

k4) – the probe altogether with a gaussmeter is located in a calibration electromagnet;

k5) – at temperature T_{1B} (for example, T_{1B} = 25°C; the equality of temperatures $T_{1B} = T_{1B0}$ is not necessary) and at two values of magnetic field induction B_{T1} being reverse (for example, B_{T1+} = 500 mT, B_{T1-} = -500 mT for amplification coefficient K_L and B_{T1+} = 100 mT, B_{T1-} = -100 mT for amplification coefficient K_H) the values of output voltages of B-channel V_{T1B+} and V_{T1B-} are measured;

k6) – temperature-dependent values of transduction coefficient K_{BT1} are calculated (for the temperature T_{1B})

$$K_{BT1} = \frac{B_{T1+} - B_{T1-}}{V_{T1B+} - V_{0T1B}};$$

k7) – at the given value of induction B_T of the magnetic field and two values of temperature T_{1BT}, T_{2BT} (for example, $T_{1B} = 25$°C; $T_{2B} = 100$°C) the value of output voltages of B-channel V_{T1B} and V_{T2B} are calculated;

k8) – the temperature-dependent values of the off-set voltage are calculated

$$V_{0T1B} = V_{00} \cdot (1 + \alpha_{V0} \cdot T_{1B})$$

k9) – the temperature coefficients of linear approximation are calculated as follows:

$$K_{B0} = \frac{V_{BT2} - V_{BT1}}{V_{BT1} \cdot T_{2B} - V_{BT2} \cdot T_{1B}}; \quad K_{B0} = \frac{K_{B1}}{1 + \alpha_{KB} \cdot T_{1B}}$$

where $V_{BT1} = V_{T1B} - V_{0T1B}$; $V_{BT2} = V_{T2B} - V_{0T2B}$.

The calibration process provided above is performed for both values of amplification coefficients K_L or K_H of the electronic unit's output differential voltage.

Channels of periodic in-situ calibration (C-channel)

The compensated value of the voltage of periodic in-situ calibration is calculated by the formula

$$V_{CT} = V_{C0} \cdot (1 + \alpha_C \cdot T) \qquad (4.6).$$

Voltages V_{CT} of C-channel are determined as the difference

$$V_{CT} = V_{CT}[I_{HG} => ON] - V_{CT}[I_{HG} => OF]$$

where $V_{CT}[I_{HG} => ON]$ and $V_{CT}[I_{HG} => OF]$ are the measured values of C-channel voltage at switched on and switched off current of the Hall sensor supply correspondingly.

During calibration, the measurement of output voltages V_{CT} of C-channel is performed at two temperatures T_1 and T_2 determined using T-channel. By results of these measurements and using the system of equations

$$\begin{cases} V_{CT1} = V_{C0} \cdot (1 + \alpha_C \cdot T_1) \\ V_{CT2} = V_{C0} \cdot (1 + \alpha_C \cdot T_2) \end{cases}$$

the following constants are calculated:

$$\alpha_C = \frac{V_{CT2} - V_{CT1}}{V_{CT1} \cdot T_2 - V_{cT2} \cdot T_1}; \quad V_{C0} = \frac{V_{CT1}}{1 + \alpha_C \cdot T_1}$$

During periodic calibration the following measurement and calculations are performed:

c1) – the voltage V_{TN} of T-channel is measured and using formula (4.1) the temperature T_N is calculated;

c2) – using formula (4.6) the basic temperature-compensated value of voltage V_{CTN} of C-channel is calculated;

c3) – the real values of voltage of C-channel are measured $V_{CTR} = V_{CT}[I_{HG} => ON] - V_{CTR}[I_{HG} => OF]$;

c4) – the coefficient $K_C = V_{CTR}/V_{CTR}$, which determines the discrepancy between the real Hall sensor sensitivity and its basic value, is measured. This coefficient is used for the determination of the drift of Hall sensor sensitivity under irradiation effect and, if necessary, for the correction of coefficient K_{BT}.

4.3. RHP-WB instrumentation

RHP-WB instrumentation, as well as previously described RHP-ISC, has been developed for plasma magnetic field monitoring in nuclear fusion reactors. The main feature of RHP-WB is wideband magnetic field measurement with electromagnetic noise compensation.

RHP-WB instrumentation is based on radiation-stable Hall sensors. As was mentioned before, in contrast to pick-up coils, which have been traditionally used for nuclear fusion reactors' magnetic field measuring, Hall sensors do not have any particular restrictions on measuring steady-state and DC magnetic fields. However, considerable electromagnetic noise on the outputs of Hall sensors and signal lines, which connect the sensors and signal processing circuits, sets a restriction upon the frequency range of the Hall sensor devices.

The electromagnetic noise is caused by the electromotive force, which generates the voltage V_{EMF} in the sensor's measuring circuit. The value of this voltage is proportional to the effective area of the S_E loop, on which the magnetic field induction is being changed:

$$V_{EMF} \sim S_E \cdot \frac{dB}{dt}$$

The effective area of the loop $S_E = S_H + S_L$ includes the area S_H, which is formed by the outputs of the Hall sensor, and the area S_L, which is formed by the signal line wires (Fig. 4.4). So that to minimize the electromagnetic noise, it is necessary to reduce the above-stated areas, which can be done by using the special topologies of Hall sensors and signal lines TL in the form of twisted pairs. However, as far as the electromagnetic noise is proportional to the frequency f_M, such a solution is not appropriate at $f_M > 10$ kHz.

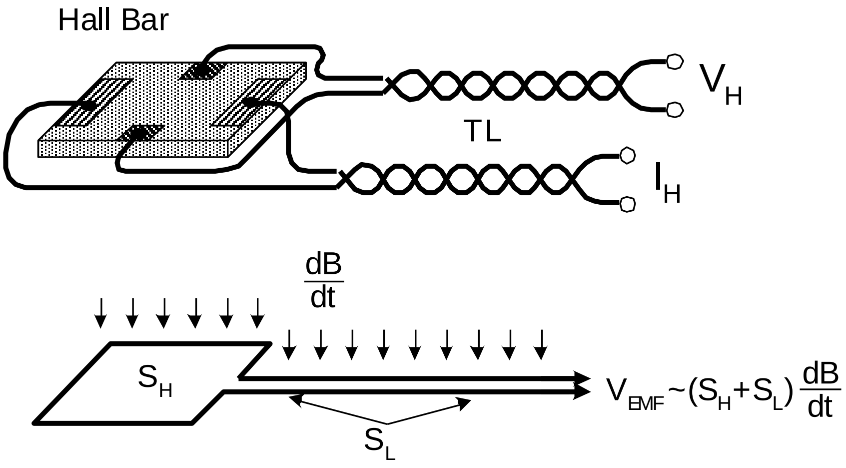

Fig. 4.4. Electromagnetic noise V_{EMF} generation in the Hall sensor circuit.

The stated problem is especially noticeable when the Hall sensors are located in the vacuum vessel of the nuclear fusion reactors. In this case, first, the length of the signal lines more than 5 m between the sensor, which is located in the reactor vessel, and the signal processing circuit, which is located outside of the vessel, is significant, which leads to the increase of the area S_H and response V_E. Second, it is impossible to make a high-performance twisted pair of wires with polymer insulation due to thermal instability and outgassing of the insulation, while using the wires with mineral insulation does not allow minimizing their area S_L due to the considerable diameter and rigid case of these wires. Third, thermally stable radiation hard Hall sensors are characterized by low sensitivity (less than 50 mV/T), which results from the necessity to use thermally stable heavily-doped semiconductors with low charge carrier mobility. This significantly impairs the signal-to-noise ratio, and thus restricts the operating frequency range (not more than 10 kHz) for the magnetic field measuring devices based on Hall sensors.

So that to solve the problem of making the magnetic field measurement frequency range wider up to f_M = 250 kHz at analog-to-digital conversion frequency f_{ADC} = 500 kHz, the method of synchronous signal detection is used. This would allow a significant decrease (more than by the factor of 100) in the influence of the electromagnetic noise V_{EMF} induced on both sensor (with the active area S_H) and signal lines (with active area S_L). To implement this method, each measurement is performed once per two cycles, with the direction of the current through the Hall sensor being changed in each cycle. Taking into account that when the supply current direction is changed, the galvanomagnetic component of the output signal is reversed while the polarity and value of the electromagnetic noise remain the same, we can state the following system of equations:

$$\begin{cases} V_{M1} = K_H \cdot I_H \cdot B + K_{EMF} \cdot S_E \cdot \dfrac{dB}{dt} \\ V_{M2} = -K_H \cdot I_H \cdot B + K_{EMF} \cdot S_E \cdot \dfrac{dB}{dt} \end{cases}$$

where: V_{M1}, V_{M2} is the voltage in the measuring circuit in the first and the second cycles; K_H, I_H is sensitivity and supply current of the Hall sensor; B is magnetic field induction; K_{EMF}, S_E is a transduction factor and effective area, on which the electromotive force is generated (electromagnetic noise).

So to solve the above-stated equation system, we can subtract one equation from another and receive the result of the magnetic field induction measuring, which, in the first approximation, does not depend on the electromagnetic noise. However, practically, the efficiency of synchronous signal detection is not a simple task. The problem is that electromagnetic noise, which is a term in both above-mentioned equations, is not a constant value.

This problem might be solved by the filtration of the high-frequency signal component and averaging the results of several two-cycle measurements, as well as by the analogue method applying the integrators and the digital method applying the spectral analysis. It is obvious, that such solutions restrict the frequency band of the magnetic field to be measured and for this reason cannot be applied for high-frequency measurements.

RHP-WB instrumentation is based on an alternative solution by increasing the Hall sensor's supply current switching frequency up to the level, which exceeds the frequencies of the magnetic field and electromagnetic noise. Such a solution does not restrict the measuring frequency band, but it raises considerable technical problems: it is necessary to generate, transmit at a long distance and accurately convert high-frequency signals. In particular, if it is necessary to receive the stream of signal data at the analog-to-digital transduction frequency f_{ADC} = 500 kHz, then supply current switching, the transmission of the small Hall sensor signal at a long distance and its amplification should be performed at the 1MHz frequency at the least. That is why for the two-cycle synchronous measurements it is necessary to use two analog-to-digital transducers f_{ADC} = 500 kHz (one transducer per one measurement cycle) and corresponding units of analog signal commutation and its storage during the analog-to-digital transduction.

The layout of RHP-WB instrumentation is presented in Fig. 4.5. Each set consists of a probe and an electronic unit (ELU) connected by a signal transmission line (TL). The probe contains three orthogonal Hall sensors HG_X, HG_Y, HG_Z and RT thermo-resistor. The electronic unit generates and amplifies signals V_{MX1}, V_{MY1}, V_{MZ1}, V_{MX2}, V_{MY2}, and V_{MZ2} by means of two-cycle synchronous detection.

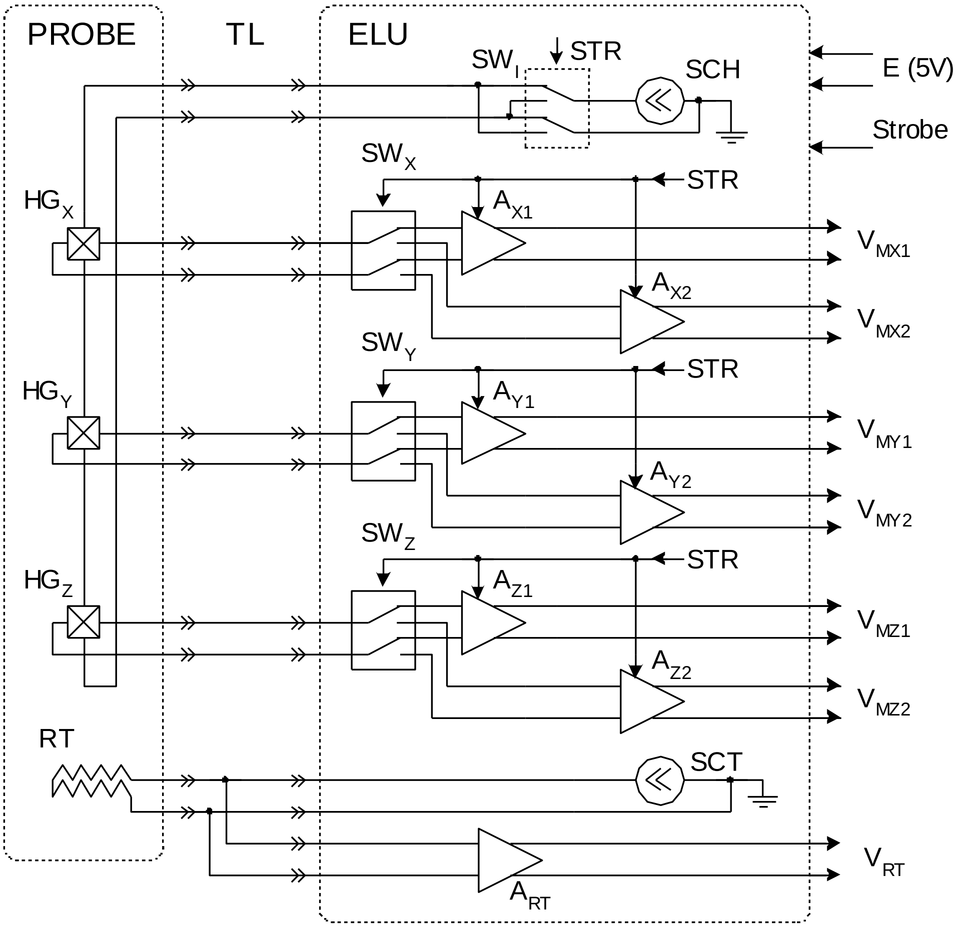

Fig. 4.5. The layout of RHP-WB instrumentation.

Based on these signals, three components of the magnetic field induction vector B_X, B_Y and B_Z are calculated. Two signals, V_{M1} and V_{M2}, are provided for the calculation of each magnetic field induction vector component. Subsequent analog-to-digital conversion of these signals at frequency f_{ADC} = 500 kHz makes the electromagnetic noise compensation possible, which in its turn provides accurate magnetic field measurement within the 0÷250 kHz frequency range. The electronic unit contains current sources SCH, SCT, switches SW_I, SW_X, SW_Y, SW_Z and differential amplifiers A_{X1}, A_{X2}, A_{Y1}, A_{Y2}, A_{Z1}, A_{Z2}, A_{RT}.

The design and the prototype of the probe are shown in Fig. 4.6, where: 1 – base, 2 – assembly cube, 3 – Hall sensors, 4 – thermoresistor; 5 – ceramic printed circuit boards PCB, 6 – metallization of PCB, 7 – outputs, 8 – supporting structures, 9 – lid, 10 – screws or pins, 11 – holes for mounting.

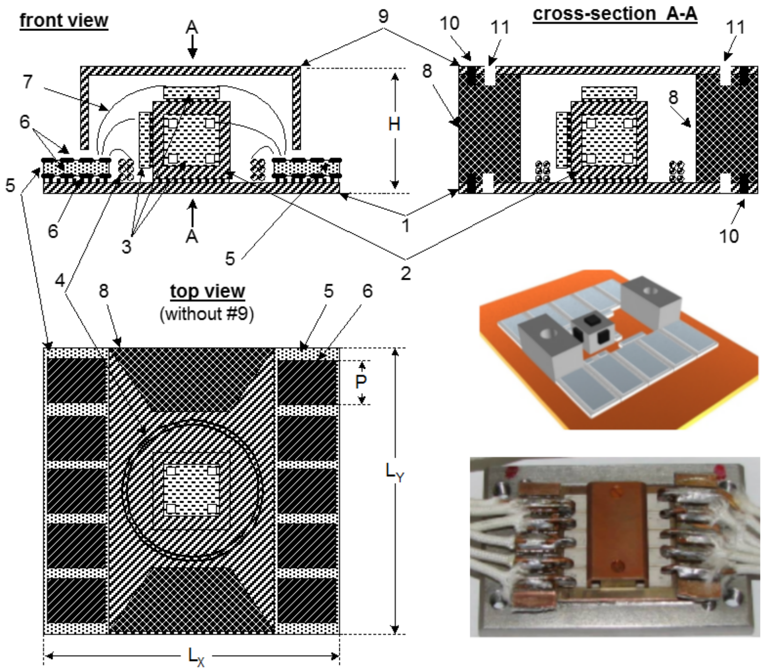

Fig. 4.6. The design and the prototype of the probe.

4.4. RHP-MAP instrumentation

RHP-MAP instrumentation has been developed for permanent cyclotron magnet magnetic field high-precision mapping in charge particle accelerators.

Two principally different approaches are most widely used for high-precision magnetic field measuring. The first one is based on Nuclear Magnetic Resonance (NMR) probes and provides very high measuring accuracy. Unfortunately, NMR probes cannot operate in inhomogeneous magnetic fields. The second approach is based on Hall sensor (HG) probes. Such HG probes do not have any limitations concerning field homogeneity, but their measuring accuracy is rather low. Low accuracy is caused by certain transducing characteristics instability typical of all semiconductor HG (sensitivity, off-set voltage) and the presence of various parasitic effects in semiconductor HG (for example, planar effect).

The novelty of RHP-MAP instrumentation is based on the integration of the HG probes set and NMR magnetometer into a complex measuring system that is calibrated directly in a cyclotron magnet. For HG probes calibration they are placed around the circle (Fig. 4.7).

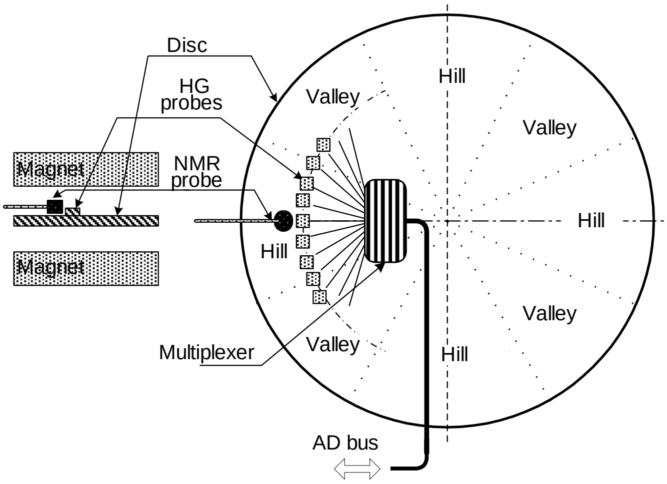

Fig. 4.7. Location of the HG probes during the calibration.

The NMR probe should be placed near one of the HG probes and the area of the NMR probe should meet the requirements of high field homogeneity in the middle of one of the “hills” or “valleys” of the magnet. During the calibration using the NMR probe, accurate values of the field and the output signal of the HG probe located around are measured. The disk rotates during calibration, which allows the alignment of all the HG probes of the mapper with the NMR probe. This procedure is performed consequently in the “hill” and “valley” areas, which allows achieving at least two positions of the field where the maximum calibration accuracy is provided. During mapping, the HG probes are placed along the radius (Fig. 4.8).

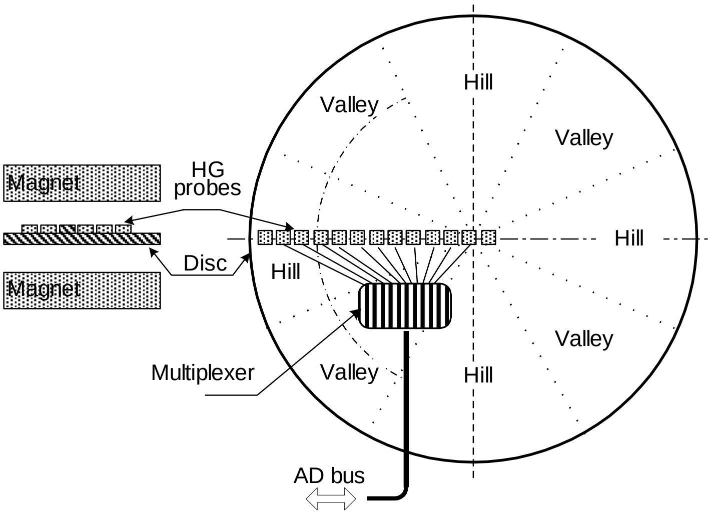

Fig. 4.8. Location of the HG probes during the cyclotron magnet mapping.

RHP-MAP instrumentation (Fig. 4.9, Fig. 4.10) consists of a signal processing unit, a multiplexer unit (Fig. 4.11), and a set of probes. The signal processing unit provides high-precision analog-to-digital conversion and communication with a computer. The multiplexer unit provides stabilization of the power-supplying modes of the probes set, amplifying and signals multiplexing from 24 magnetic field sensors and 2 temperature sensors. RHP-MAP is complemented with two multiplexer units that are operating synchronously with one signal processing unit. This allows an increase in probes amount: 48 magnetic field probes and 4 temperature sensors. The probe set and multiplexer unit are located on the disk in the gap of the magnet under magnetic field mapping.

The signal processing unit contains 5 data buses:

- AD-bus-1, AD-bus-2 – with multiplexer units;
- D-bus – with the computer;
- M-bus – with the step motor controller;
- E-bus – with the angle encoder.

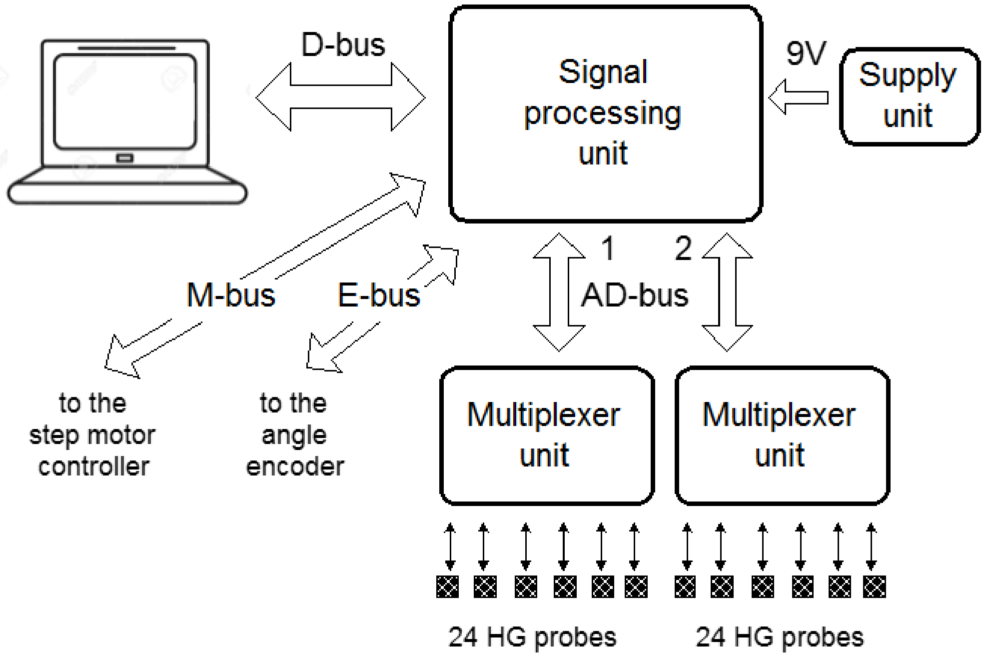

Fig. 4.9. The block diagram of RHP-MAP instrumentation.

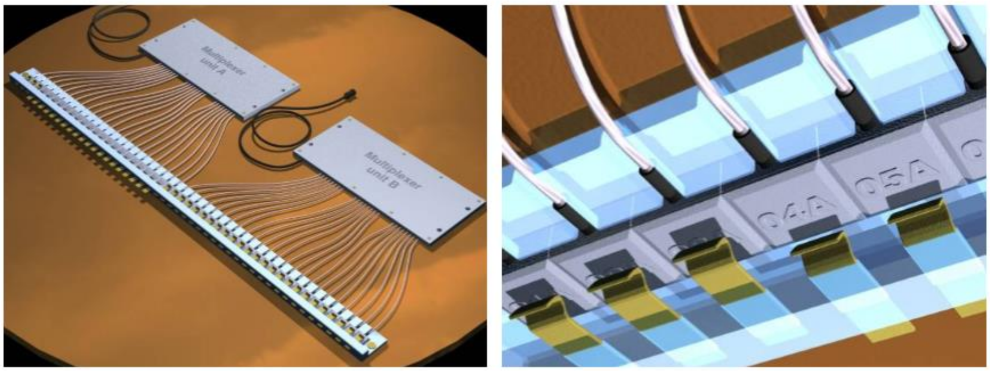

Fig. 4.10. Multiplexer units and set of probes.

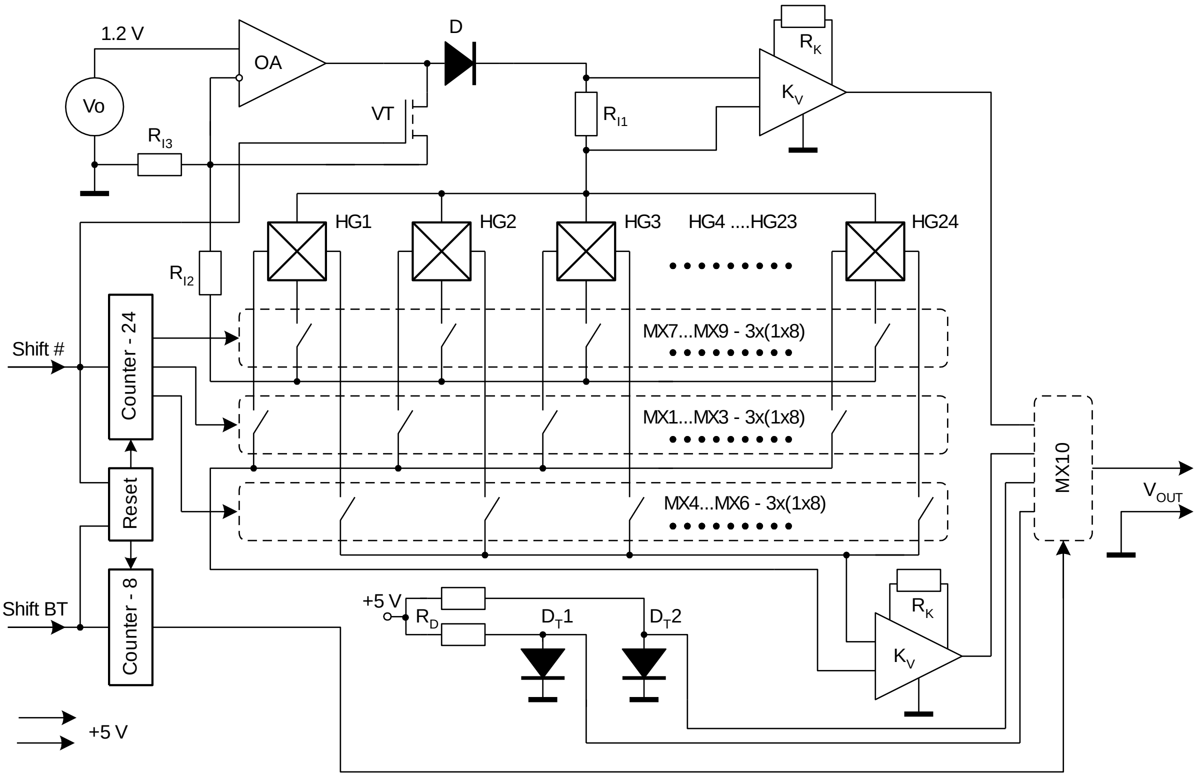

Fig. 4.11. The layout of the multiplexer unit with Hall sensors set.

The multiplexer unit consists of:

- Reference-voltage source V_0;
- Current stabilizer based on the operational amplifier OA (R_{II} – current measuring resistor, R_{12} – biasing resistor, R_{13} – current set resistor);
- Current commutation circuit based on the diode D and field-controlled transistor VT;

- Hall sensors feed circuits switches based on the analog multiplexers MX7÷ MX9;
- Hall sensors signal switches based on the analog multiplexers MX1÷ MX6;
- Amplifiers of the Hall sensors signals and current measuring circuit based on the differential amplifiers K_V and resistors R_K;
- Circuits of the temperature signals based on the temperature diodes D_{T1}, D_{T2};
- Output switches based on the analog multiplexer MX10;
- Digital circuits of the multiplexers control – Counter 24, Counter 8, Reset.

Consequent commutation of the Hall sensors channels is provided by control pulses Shift #. Each pulse Shift # increases the amount of the pulses counted by the counter Counter 24, and, therefore, changes the channel number. In the case of Shift # = 0 mode of the measurement of the Hall sensors signals V_H is formed. When Shift # = 1 abridgement of the supply current through the transistor VT occurs, and so current does not flow through the Hall sensors. It allows the measurement and compensation for the offset voltage V_{H0}.

The output switch provides analog multiplexing of the output voltage V_{OUT}. This switch is controlled by pulses Shift BT which change the number in Counter 8. During the first cycle V_H and V_{H0} voltages from the amplifier of the signals of the Hall sensors are formed. During the second cycle V_I and V_{I0} voltages from the amplifier of the signals of the current-collecting resistors are formed. During the third and fourth cycles the signals from the temperature diodes D_{T1} and D_{T2} are formed, correspondingly. When one-level pulses simultaneously occur on two control inputs Shift # and Shift BT, it resets Counters 8 and Counter 24. This provides device transition to the initial state – measurement of the magnetic field induction using the first channel.

The voltage on the temperature diodes D_{T1}, D_{T2} is used directly by a program for the temperature calculation. Voltages of the Hall sensors V_H, V_{H0} and the corresponding voltages from the current-collecting resistor V_{RI}, V_{RI0} are used to form the normalized signal M calculated by a program according to the equation

$$M = \frac{V_H - V_{H0}}{V_{RI} - V_{RI0}}.$$

Using the normalized signal M as an informative parameter of the measured magnetic field B solves a problem of the compensation of the additive and multiplicative error components and thus provides high measurement accuracy.

It was necessary to solve the principally important problem of strict keeping of sensors plane parallel to the lower base of the probes during the mapper’s development. This problem is relevant because of the necessity of measurement error decreasing. The measurement error is caused by a change in the sensors’ angle of slope in the magnetic field of the magnet being investigated.

The output voltage of the sensor at a first approximation is determined by the cosine of the angle between the vector of magnetic field induction B and normal N to the plane of the sensor active layer. This angle, in its turn, is determined by two other angles – by angle α between the field induction vector and normal to the plane of the probe, and angle β between the plane of the sensor active layer and plane of the probe (Fig. 4.12). In some cases, these angles are added, and in other cases – they are subtracted. Rotation of the sensor, whose active layer is tilted in relation to the probe plane, around its axis by 180° will cause a change of the output signal for $\cos(\alpha - \beta) - \cos(\alpha + \beta)$.

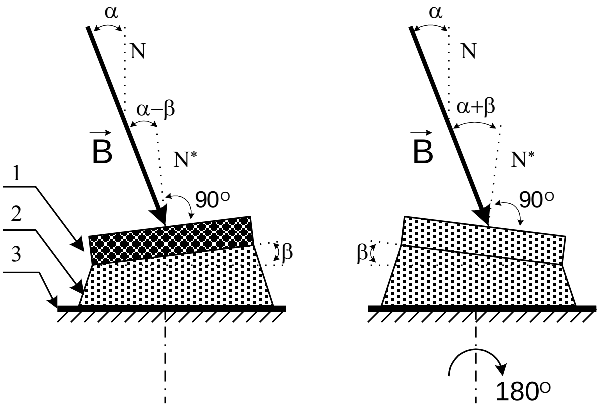

Fig. 4.12. The chip mounting: 1 – chip, 2 – transient layers, 3 – base.

Let us notice that if at least one of the mentioned angles tends to zero, sensor rotation around its axis does not cause a change in the output signal. Besides, in the case of $\alpha \to 0$ or $\beta \to 0$ one can apply approximation $\cos(\alpha - \beta) - \cos(\alpha + \beta) \to 0$.

In the cyclotron magnet mapping problem by mounting the probes array onto the disk, one may observe a change in the output signal during the disk rotation around its axis (Fig. 4.13). The reason for such a signal change is the presence of angle (β) between the sensor active layer and lower probe surface and the presence of angle of disk tilting (α) in the magnet gap.

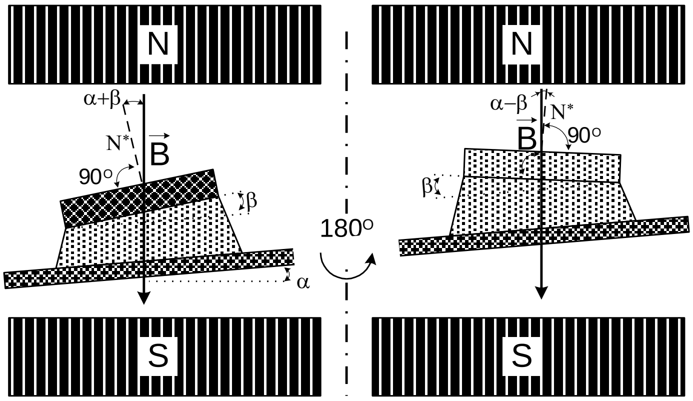

Fig. 4.13. The chip mounting on the disk in the magnet gap.

To minimize the angle β value, technology was developed for sensor chip precise mounting into probes and checking the parallelism of the chip working plane to the lower probe surface. The know-how of the developed technology consists in methods of keeping the chip mounting zone plane perfectly parallel to the lower probes surface, top-quality sensor chip gluing and control of parallel mounting.

The technique of parallel chip mounting control is represented in Fig. 4.14. Control is carried out using the rotation gear that allows the probe to rotate around its axis in the magnetic field. During the control process, one may measure minimum and maximum signal values by rotating the probe being investigated. To increase measurement accuracy, the probe plane is initially inclined under a certain angle to the magnetic field induction vector (for example, $\alpha = 50°$). Such a location allows significant sensitivity increasing of the technique of measuring non-parallelism of sensor mounting. It is presented in Fig. 4.15, a. So, at non-parallelism

$\beta = 1°$ (β is the angle between the sensor active layer and the probe plane) and at a zero angle of inclination of the probe normal to the magnetic field induction vector $\alpha = 0°$, a relative signal change at the rotation of the probe for 180° is $\delta = 100\% \cdot (\cos(\alpha + \beta) - \cos(\alpha)/\cos(\alpha)) \approx 0.015\%$.

At the same non-parallelism ($\beta = 1°$) and inclination angle $\alpha = 50°$ (Fig. 4.15, b), the relative signal change is $\delta = \pm 1.2\%$, i. e. non-parallelism measurement method sensitivity increases in two orders.

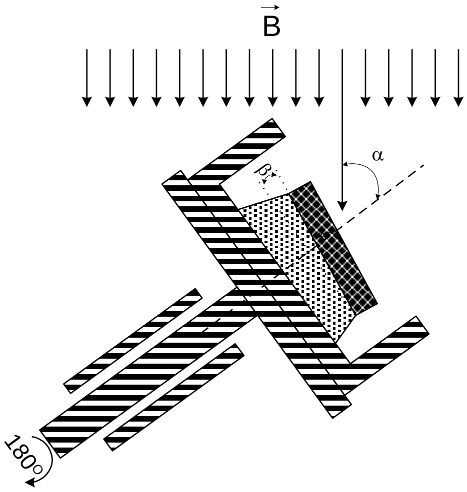

Fig. 4.14. Mechanism of control for sensor mounting in the probes.

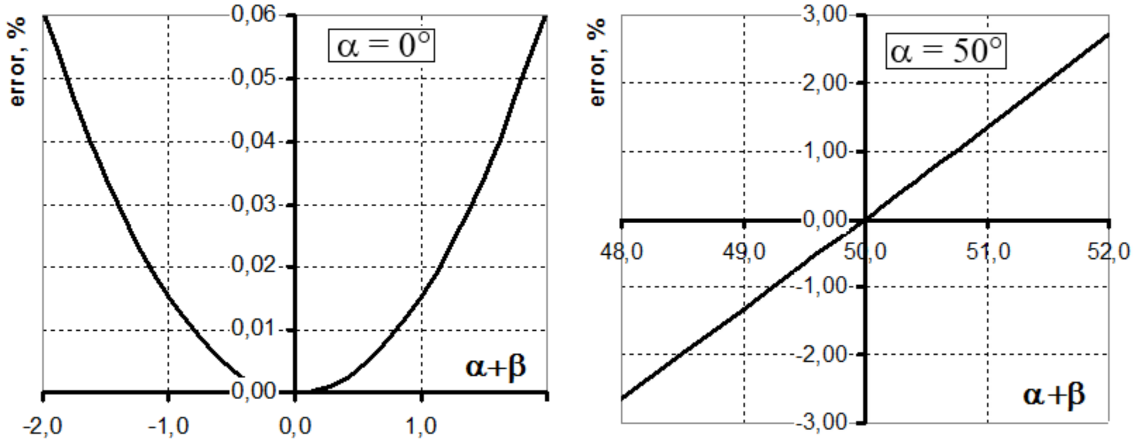

a) b)

Fig. 4.15. Non-parallelism error of mounting sensors into probes.

Using the described technique, sensor mounting non-parallelism was measured for all probes manufactured for the mapper. The investigations have shown that the signal change during rotation of the manufactured probes around their axes at α = 50° does not exceed δ = ±0.6%, which corresponds to the non-parallelism angle β =0.5°. So, at α = 0° the signal change will be within the range of δ = ±0.005%.

Calculation graphs of the limiting error values of the cyclotron magnetic field mapping at the different disk inclination angles and maximum values of the sensor non-parallelism angles of β =0.5° are given in Fig. 4.16. Therefore, for keeping the measurement error within the range of δ = ±0.01% non-parallelism of the disk mounting in the magnet gap should not exceed α = 0.5°.

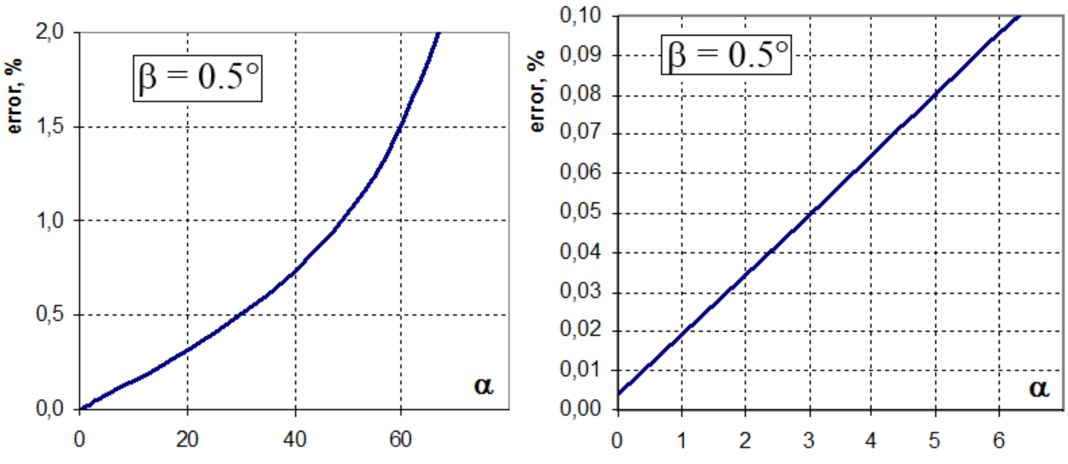

a) b)

Fig. 4.16. Non-parallelism error of mounting the disk into the magnet.

High requirements to magnetic field distribution measuring accuracy specifications at a considerable amount of measuring channels (sensors) have caused the necessity for special calibration methodology development. The problem is caused by the fact that Hall sensors' time stability is insufficient for providing long-term measurements with an error of ±0.01%. Consequently, the necessity of periodical calibration appears.

We also should take into consideration the fact that Hall sensors field transducing functions approximation using continuous polynomial functions is very problematical. On the one hand, at low values of polynomial function degree, it is impossible to reach the defined approximation accuracy. On the other hand, at high values of the polynomial, it becomes impossible to manage a simple way of transducing function correction even in case of inessential time drift. This may be explained by the fact that correction of high-degree polynomial coefficients leads to considerable function drift: while decreasing approximation error in one of the field points, the error in other field points increases. This error increase may become several times bigger than before the correction. Besides, it should be taken into account that in the case of numerous sensors, high-powered polynomial coefficient correction is a complicated and continuous process.

The above-stated facts have caused the necessity of developing such a calibration and transducing function coefficient correction methodology that can provide high-precision mapper measuring channels transducing function approximation, simplicity, flexibility, and easiness of the periodical function correction process.

The investigations being carried out have shown that Hall sensors' field characteristics may be described quite accurately (with accuracy within ±0.01%) only by a high-degree polynomial. However, if periodical transducing function calibration is necessary, using high-degree polynomials is highly undesirable. In order to decrease the degree of polynomials, it has been decided to divide the whole field characteristic into several areas. This allows using second-degree polynomials for every area. Its correction during the calibration of the sensor is quite simple.

The investigations have shown that in the range of real field values in cyclotron magnets (magnitude of magnetic field induction does not exceed 1.4 T) it is sufficient to use only three areas to provide ±0.01% of measuring results mutual disarrangement of all Hall sensors, namely:

- area "–B" for $B < -B_Z$;
- area "B_0" for $-B_Z < B < B_Z$;
- area "+B" for $B > B_Z$,

where ±B_Z – field points where a transition between two approximation areas occurs (usually $B_Z = 0.5$ T).

Taking into consideration that the field in the working gap of cyclotron magnets under the investigation is unipolar and usually is within $B < -B_Z$ or $B > B_Z$, it is possible to perform mapping of these magnets only in one of the areas of the field characteristics (area "–B" or "+B"). This circumstance is of great importance and it allows us to perform a relatively simple method of periodical mapper calibration.

The general view of "Calibration" window is represented in Fig. 4.17. Every channel of the mapper has its own window of approximation coefficients, where four types of calibration are represented:

- "NOMINAL" – nominal characteristics;
- FINE_NOM" – corrected nominal characteristic;
- "NMR" – characteristic, based on NMR probe data;
- FINE_NOM" – corrected "NMR" characteristic.

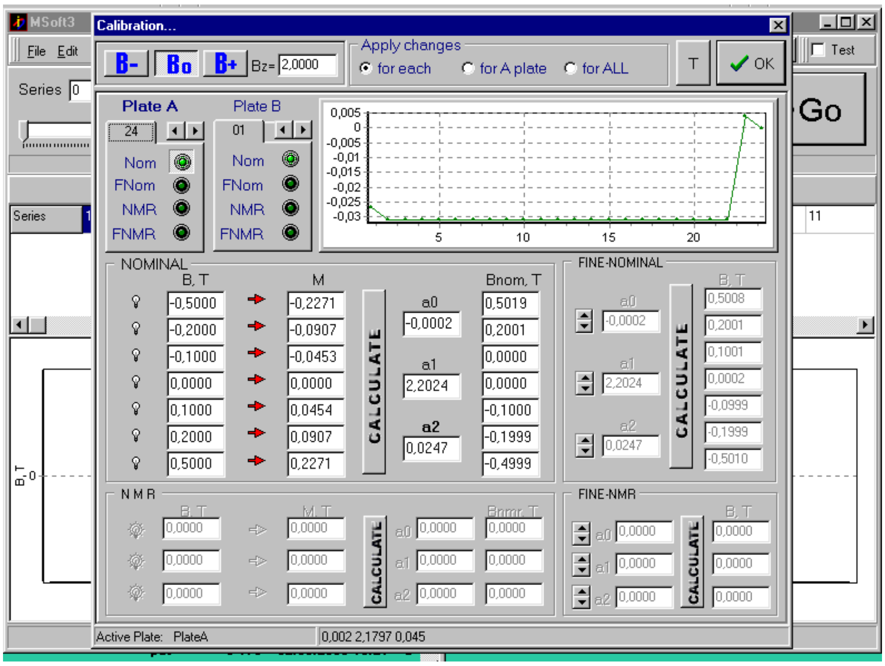

Bz= 2,0000

Apply changes: ● for each ○ for A plate ○ for ALL

Series 0

NOMINAL

B, T	M	Bnom, T
-0,5000	-0,2271	0,5019
-0,2000	-0,0907	0,2001
-0,1000	-0,0453	0,0000
0,0000	0,0000	0,0000
0,1000	0,0454	-0,1000
0,2000	0,0907	-0,1999
0,5000	0,2271	-0,4999

a0 -0,0002
a1 2,2024
a2 0,0247

FINE-NOMINAL

a0 -0,0002
a1 2,2024
a2 0,0247

B, T
0,5008
0,2001
0,1001
0,0002
-0,0999
-0,1999
-0,5010

N M R

B, T	M, T	Bnmr, T
0,0000	0,0000	0,0000
0,0000	0,0000	0,0000
0,0000	0,0000	0,0000

a0 0,0000
a1 0,0000
a2 0,0000

FINE-NMR

a0 0,0000
a1 0,0000
a2 0,0000

B, T
0,0000
0,0000
0,0000

Active Plate: PlateA 0,002 2,1797 0,045

Fig. 4.17. Calibration window view.

The calibration type may be the same for all channels or it may be chosen for each channel separately. Switching between calibration types may be performed using “NOMINAL”, “FINE_NOM”, “NMR” or “FINE_NOM” buttons, which may be set first in “All” panel or second in the approximation coefficients window for a corresponding channel. In the same way, if chosen for calibration magnetic field values are matching in all channels, they may be set in “All” panel. In the mismatch case, they may be set in the windows corresponding to the channels.

For the chosen field points, the corresponding values of the normalized M signals are measured by activating the measuring process. After measuring of M = f(B) set of data in all seven or at least three field points B_{Mi}, the polynomial coefficients a_0, a_1, and a_2 are calculated. The coefficient calculation is performed for three reference points of the field. Those reference points are the normalized M signals by default at minimal, maximal and average values of the field $M_{min} = f(B_{min})$, $M_{max} = f(B_{max})$, $M_{av} = f(B_{av})$, that are chosen from the available M = f(B) set of data.

Calculation is performed by the following equations:

$$a_2 = \left(\frac{B_{max}-B_{av}}{M_{max}-M_{av}} - \frac{B_{av}-B_{min}}{M_{av}-M_{min}}\right) \cdot \frac{1}{M_{max}-M_{min}};$$

$$a_1 = \frac{B_{av}-B_{min}}{M_{av}-M_{min}} - (M_{av} + M_{min}) \cdot a_2;$$

$$a_0 = B_{min} - a_1 \cdot M_{min} - a_2 \cdot M_{min}^2.$$

The field reference points may be changed during the measurement process. Icons “⊗” are used for this purpose, which correspond to necessary field values. Choosing the reference field points is optimal if the minimum value is close to the field values in the “valleys” of magnets under investigation and the maximum values are close to the values in the “hills” of the magnet.

Besides the direct polynomial coefficients a_0, a_1, a_2, “NOMINAL” characteristic is obtained as a result of calculations

$$B_{NOMi} = a_0 + a_1 \cdot M_i + a_2 \cdot M_i.$$

So, by matching calculated values of B_{NOMi} with the input B_{Mi} set it becomes possible to perform a quick approximation quality analysis.

If approximation quality is insufficient or field characteristic has a little drift during the mapper transportation, transducing function polynomial coefficients may be corrected. The corrected nominal characteristic panel (“FINE_NOM”) is used for this purpose. Changing the a_0, a_1, and a_2 coefficients one may observe corresponding $B_{FINENOMi}$ values change.

“FINE_NOM” characteristics are also used for direct calibration of the mapper in the magnet under the investigation. In this case, magnetic sensors are placed on the disc in a circle. The sensors pass through determined spatial points in the magnet gap by rotating the disc. There should be three such points – a point with the minimal field (“valley” area), a point with the maximum field (“hill” area) and a point with the average field value (for example, in the “hill” area in the case of the increased magnet gap). Such calibration is performed as follows.

First, the normalized signals from all the sensors of the mapper are obtained at the first point of the magnet gap. The mapper is switched to “Single” step-by-step measuring mode. Sensor #1 is matching with first spatial point by rotating the disc. The first channel measurement result is obtained by pressing “Go” button once. Further, sensor #2 is introduced into this spatial point of the magnet gap by rotating the disc, and its measurement result is obtained.

Measuring results of all other sensors of the mapper are achieved in a similar way. During this process in the graphic window one can see field induction measurement results in a defined spatial point using nominal polynomial coefficients. To improve the resolution of plots, they may be scaled by selecting a scaling area with a mouse pointer. It is obvious that in the case of the perfect calibration of the nominal characteristic, the measuring results of all mapper channels will match absolutely. In practice, the absolute matching of measuring results of all channels is impossible. It is because of a particular error in the spatial matching of sensors in a particular field point, because of noises and interferences present in measured signals, and also because of calibration errors.

The influence of the first two sources may be decreased by performing the stated sequence of measurements several times. The results of each measurement series are recorded with the series number. Correspondingly to the measurement sequence, the above-stated normalized signals of all the mapper's sensors in the second and third spatial points of the magnet gap are obtained and recorded.

Further, "FINE_NOM" calibration characteristic formation is carried out. For this purpose, the mapper channels whose results differ from the measuring results' average value of other channels are determined using the obtained plots. It should be stated that changes that should be introduced into the coefficients a_0, a_1, a_2 are inessential. Therefore, such correction is performed manually, observing the corresponding changes in the available visual-aided measurement results in three field points.

Transducing functions' correction may be performed more precisely and quickly using "NMR" characteristic coefficients. In contrast to "NOMINAL" characteristic, "NMR" characteristic is formed directly at the magnet under the investigation. Only three field points are used, where induction values are controlled using a reference magnetometer. The highest calibration absolute accuracy is provided by using a reference Nuclear Magnetic Resonance type magnetometer (NMR).

The formation of the "NMR" characteristic is similar to the above-considered "NOMINAL" characteristic. In this case, magnetic field values are input manually, using the meterage of the reference magnetometer. As in the previous case, the polynomial coefficients of "NMR" characteristics may be corrected, using the "FINE_NOM" panel.

Calculation of the magnetic field induction magnitudes is performed taking into consideration a temperature change according to the equation $B_T = B_M \cdot \left(1 + \alpha_T \cdot (T - T_0)\right)$, where B_M is field induction value, calculated according to the chosen calibration characteristic (disregarding the temperature); α_T – Hall sensors temperature coefficients (α_T = 0.008 %/°C by default; T_0 – calibration temperature

(T_0 = 20°C by default); T – temperature calculated on the base of thermo-diode voltage V_{DT} (in case of using two thermo-diodes the temperature value is averaged).

As was stated above, three Hall sensors field characteristics approximation areas “–B”, “B_0” “+B” are used for the magnetic field induction calculation. The transition from one area to another occurs automatically at field induction values of $-B_z$ and B_z. For each mapper channel values of $-M_z$ and $+M_z$ are calculated by the software. The calculation is conducted using linear coefficients a_1 of “B_0” area by the approximation formula $M_Z = B_Z/a_1$. In the case of $-M_Z<M<M_Z$ the “B_0” area is chosen, in the case of $M<M_Z$ the “–B” area is chosen, and in the case of $M>M_Z$ the “+B” area is chosen. It should be emphasized that to prevent the influence of transducing function jumps in B_Z points on calculation results, B_Z values must be set outside the magnetic field range where maximum measurement accuracy is to be provided.

A prototype of RHP-MAP instrumentation is presented in Fig. 4.17, whereas its main characteristics are given in Table 4.2.

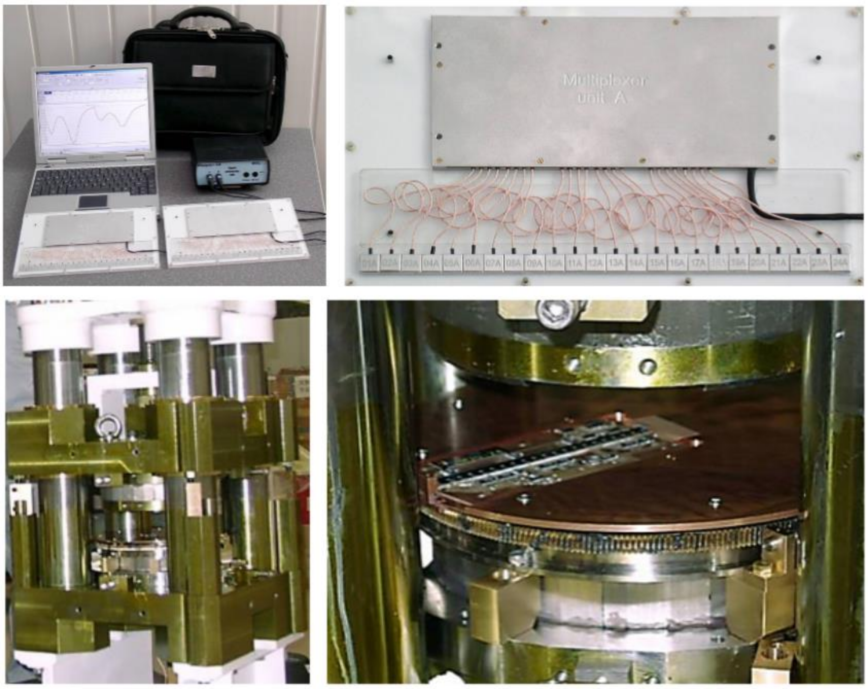

Fig. 4.17. The prototype of RHP-MAP instrumentation.

Table 4.2.

The main characteristics of RHP-MAP instrumentation

Parameter	Value
Number of magnetic field measuring channels	48
Number of temperature measuring channels	4
Magnetic field measuring results repeatability (compared to the field of B = 1T)	≤ ±0.003%
Hall sensor temperature sensitivity coefficient	≤ ±0.01%/°C
Disagreement in the transducing function approximation results in all sensors (in the range of field induction of ±0.6…1.4 T)	≤ ±0.01%
Hall sensors chip inclination into probes	≤ ±0.5 degree
Temperature measurement resolution	≤ 0.1 °C

4.5. RHP-RAD instrumentation

RHP-RAD instrumentation has been developed for investigating sensors directly during their irradiation in nuclear reactors. Here, like in the earlier described in-situ calibration technique, the main problem is generating a stable test magnetic field in remote places with a high neutron radiation level. Taking into account the impossibility of applying permanent magnets under such conditions, the test magnetic field is generated by a small electromagnet (solenoid).

For providing the required measurement accuracy, a method of signal synchronous detecting with further analog-to-digital conversion with a 24-bit microconverter is used. Such method provides measurement irrepeatability of ±0.1 % at signal level of 0.5 mV (at sensor's magnetic sensitivity of $S = 100$ mV/T the test magnetic field $\Delta B = 5$ mT generates a signal $V = S \cdot \Delta B = 0.5$ mV) and signal transmission line of the length 20 m.

The signals of the investigated sensors are measured relative to the signal of the reference sensor located outside the neutron-irradiated area. Besides, the reference sensor's test field is generated by an auxiliary coil serially connected to the coil bearing the sensors being investigated under the radiation impact. Such a solution allows compensation for the time and temperature instability of the test magnetic field.

RHP-RAD instrumentation (Fig. 4.18, Fig. 4.19) consists of two heads (Head 1, Head 2) with investigated sensors, electronic unit and signal lines (TL1a, TL1b, TL2a, TL2b, TL3). The heads are placed in the reactor channel, while the electronic unit is outside the reactor in its maintenance area (at the distance up to 20 m from the heads), and the computer is in the personnel room (at the distance up to 15 m from the electronic unit).

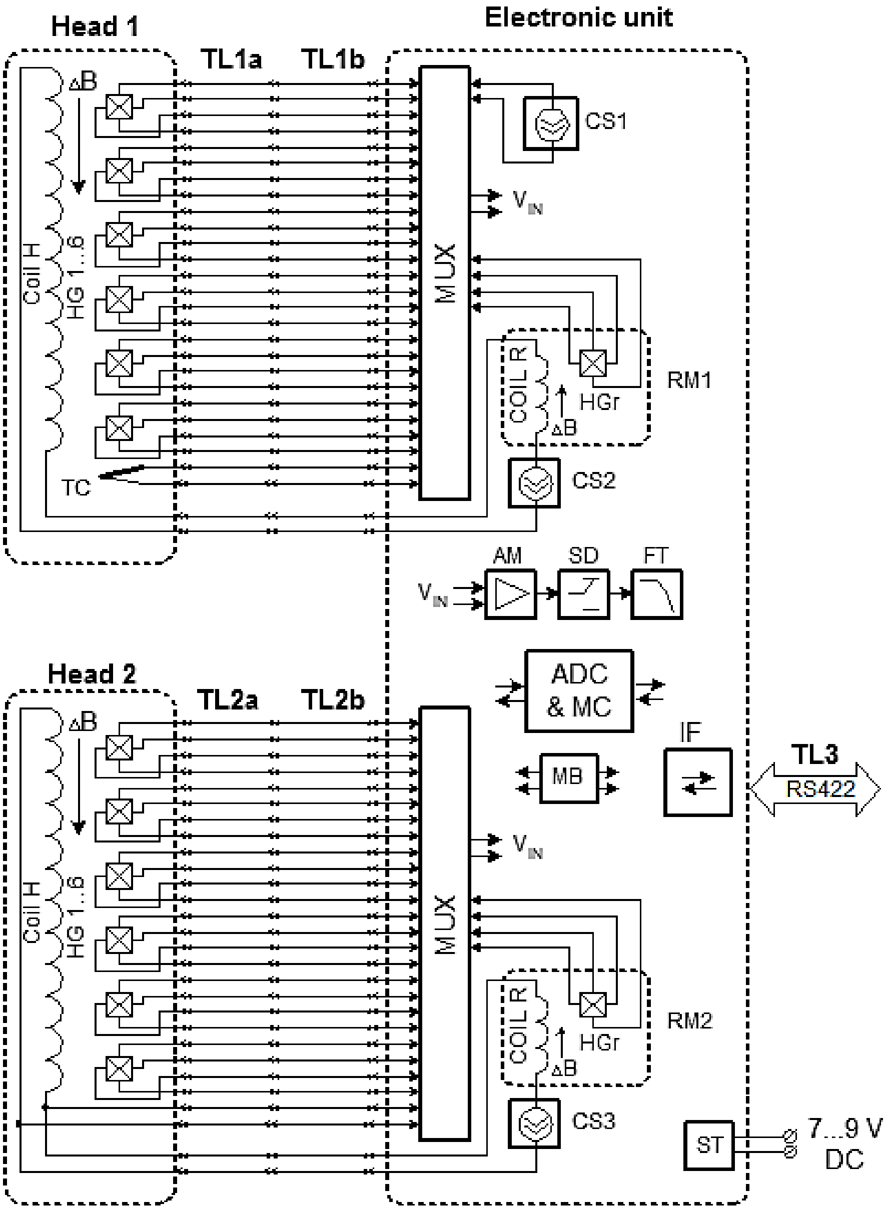

Fig. 4.18. The layout of RHP-RAD instrumentation.

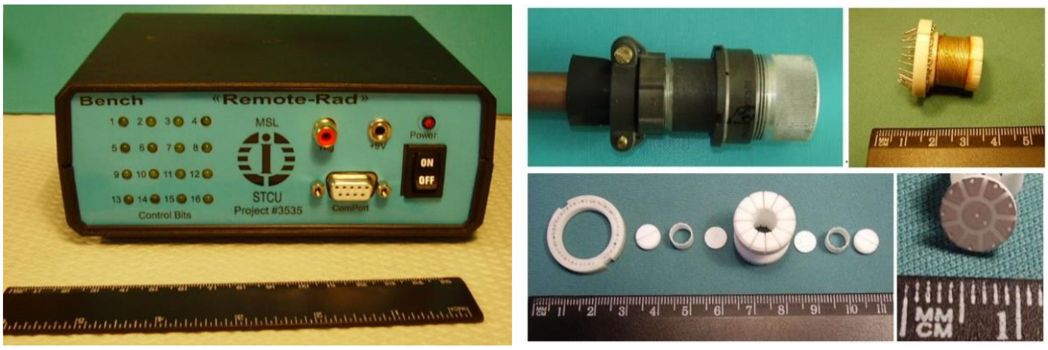

a) b)

Fig. 4.20. The prototype of the RHP-RAD electronic unit (a) and head (b).

Each head contains 6 Hall sensors or galvanomagnetic generators (HG) of some other type and Coil H for generating a test magnetic field. Head 1 contains a thermocouple for temperature measurement. The temperature of Head 2 is measured by the thermo-resistive method, with the temperature dependence of coil wire resistance used as an informative parameter. Signal lines connecting the heads to the electronic unit are meant for transferring analog signals and consist of two parts. TL1a and TL2a parts are made of rigid radiation-hard high temperature resistant wires with a length of 2m (for being installed in a reactor channel), whereas TL2b and TL1b parts are made of flexible twisted pairs. TL3 signal line is to transfer digital signals between the electronic unit and the computer.

The electronic unit consists of a MUX signal multiplexer, CS1 source of supply current for galvanomagnetic sensors, CS2, CS3 sources of supply current for coils, RM1, RM2 reference signal modules, AM amplifier, SD synchronous detector, FT signal filter, ADC&MC microconverter module, IF interface module, ST stabilizer, and MB cross-PCB. The sensors are supplied with direct current, while the coils are supplied with alternating current pulses with a frequency of about 200 Hz. Besides, each coil is supplied with a separate current source.

The signal multiplexer provides a series connection of HG sensors up to CS1 current source and the sensors' differential signals V_{IN} transfer onto AM amplifier input. Then the signal is converted with SD synchronous detector and filtered with a low-frequency FT filter. Synchronization of the signal phase in SD detector takes place along the pulse edge of current generated by CS2, CS3 coils supply current sources.

Each of the RM1 and RM2 reference signal modules consists of Coil R auxiliary coil and HGr reference Hall sensor. These modules are inside the electronic unit (outside the radiation area), and thus the parameters of HGr reference sensors and auxiliary coils can be considered unaffected. Taking into account the aforementioned facts and the auxiliary coils serially connected to the coils inside Head 1 and Head 2, periodic measurement of output signals from HGr reference Hall sensors allows us to determine the test field drift ΔB with time. Besides, representing the measurement result as the ratio between the investigated sensor signals and the HGr reference Hall sensor signal allows compensation for the parameter drift in the measurement circuit as a whole. Sensor parameters investigation provides for measuring their sensitivity, off-set voltage, temperature and voltage of interferences in the measuring circuit.

The main software window of RHP-RAD instrumentation is shown in Fig. 4.21.

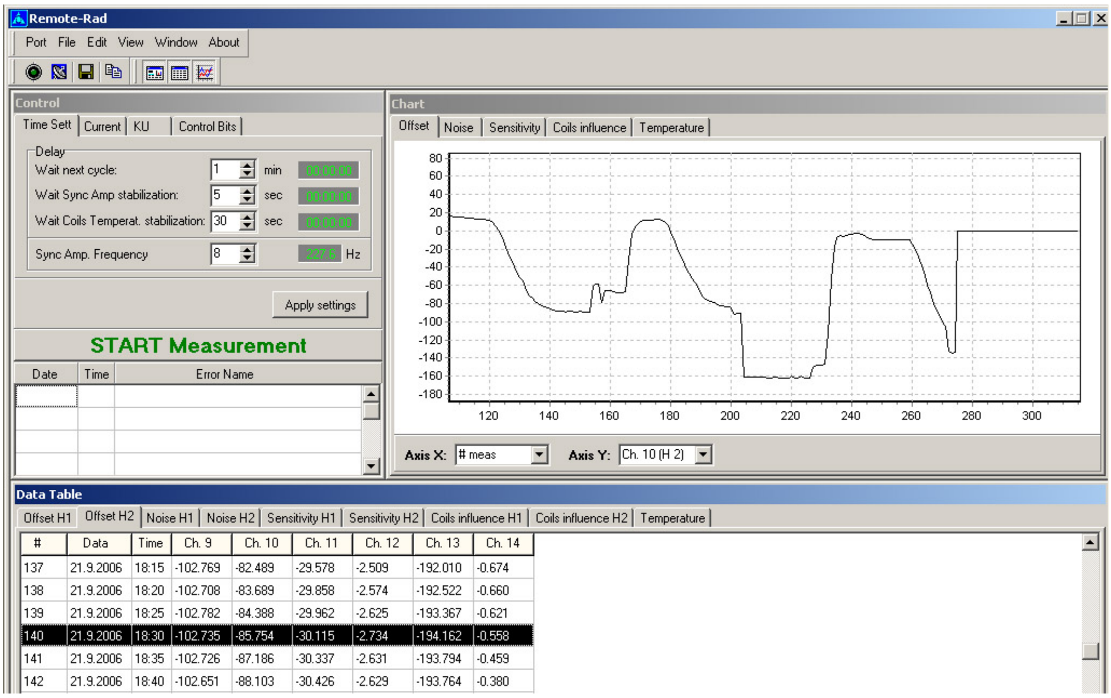

Wait next cycle: 1 min 00:00:00
Wait Sync Amp stabilization: 5 sec 00:00:00
Wait Coils Temperat. stabilization: 30 sec 00:00:00
Sync Amp. Frequency 8 227.6 Hz

Axis X: # meas
Axis Y: Ch. 10 (H 2)

#	Data	Time	Ch. 9	Ch. 10	Ch. 11	Ch. 12	Ch. 13	Ch. 14
137	21.9.2006	18:15	-102.769	-82.489	-29.578	-2.509	-192.010	-0.674
138	21.9.2006	18:20	-102.708	-83.689	-29.858	-2.574	-192.522	-0.660
139	21.9.2006	18:25	-102.782	-84.388	-29.962	-2.625	-193.367	-0.621
140	21.9.2006	18:30	-102.735	-85.754	-30.115	-2.734	-194.162	-0.558
141	21.9.2006	18:35	-102.726	-87.186	-30.337	-2.631	-193.794	-0.459
142	21.9.2006	18:40	-102.651	-88.103	-30.426	-2.629	-193.764	-0.380

Fig. 4.21. Main software window of RHP-RAD instrumentation.

4.6. Testing Hall sensors under irradiation

RHP-RAD instrumentation has been applied for direct investigation into Hall sensors under irradiation of fast neutrons. The reactor operation mode is shown in Fig. 4.22. The experiment lasted for 90 days in three sessions of the reactor operation. During reactor stops at the end of each irradiation session, the facility continued to perform measurements during the next several days in order to find out if the sensors' characteristics were affected by relaxation after the irradiation.

On the first session of the reactor operation, the samples were irradiated up to the fluence of $F_1=7{,}4\cdot10^{15}$ n cm^{-2} at the flux intensity of $j=6{,}86\cdot10^{9}$ n·cm^{-2}·s^{-1}, till the end of II session – up to the fluence of $F_2=1{,}0\cdot10^{16}$ n·cm^{-2} at $j=1{,}07\cdot10^{10}$ n·cm^{-2}·s^{-1} and till the end of the III session – up to the fluence of $F_3=3{,}1\cdot10^{16}$ n·cm^{-2} at $j=8{,}46\cdot10^{9}$ n·cm^{-2}·s^{-1}. Average reactor neutron energy was equal to E=1.5 MeV, and the portion of thermal and intermediate neutrons in the experiment was equal to 20% and 25% respectively, of the integral fast neutron flux.

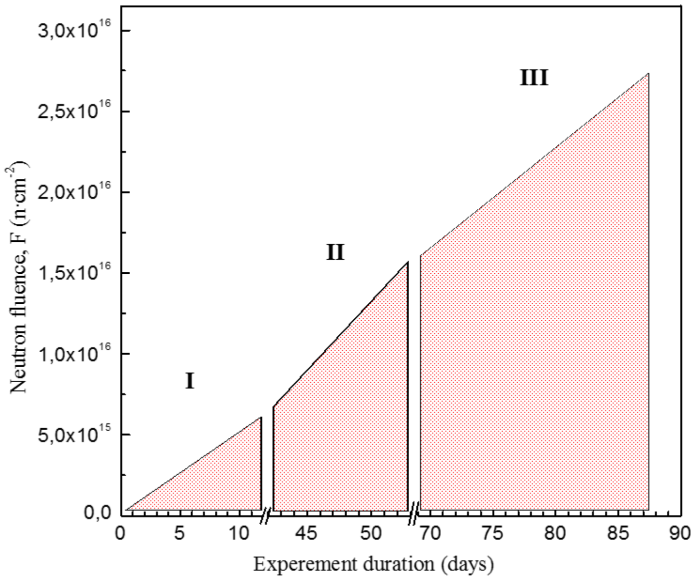

Fig. 4.22. The operating mode of neutron reactor during the experiment.

High measurement resolution and noise rejection provided by described above RHP-RAD instrumentation have been proved. For example, Fig. 4.23 presents a data array of a relative sensitivity change in one of the samples studied. It shows high resolution up to 0.01% of the measured value.

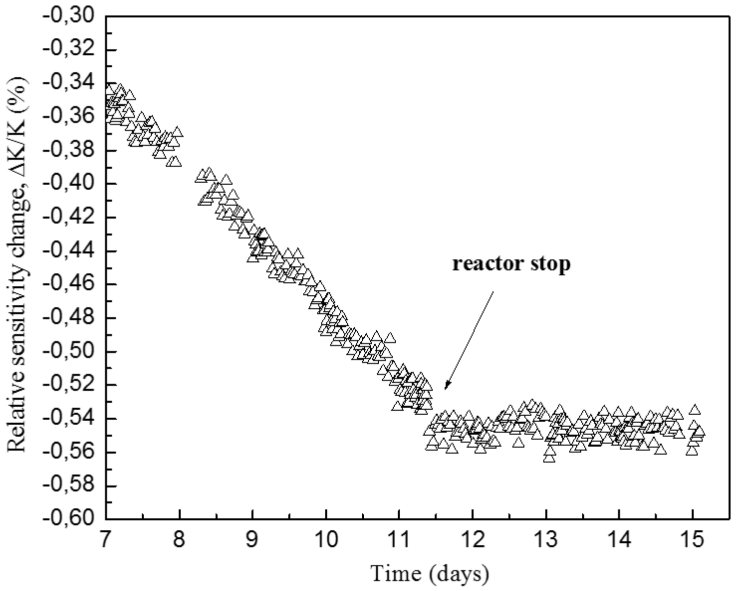

Fig. 4.22. The operating mode of the neutron reactor during the experiment.

Among 6 samples under investigation (Table 4.3), three were based on microcrystal (whiskers) with initial carrier concentration of $n_1 = 8{,}6\cdot10^{16}$ cm^{-3} (#1), $n_2 = 6{,}4\cdot10^{17}$ cm^{-3} (#2), and $n_3 = 9{,}7\cdot10^{17}$ cm^{-3} (#3). The other three were based on thin-film structure InSb with charge carrier concentration of $n_4 = 3{,}0\cdot10^{18}$ cm^{-3} (#4), $n_5 = 7{,}5\cdot10^{17}$ cm^{-3} (#5), and $n_6 = 3{,}4\cdot10^{17}$ cm^{-3} (#6). Relative sensitivity (Fig. 4.23) and charge carrier concentration dependencies (Fig. 4.24) have been studied.

Table 4.3

The parameters of the magnetic field sensor (at 300K) being tested

№	Initial charge carrier concentration n, cm^{-3}	Mobility μ, $cm^2\cdot V^{-1}\cdot s^{-1}$	Resistivity ρ, Ω·cm
Microcrystal magnetic sensors			
#1	$8{,}6\cdot10^{16}$	52400	$14{,}3\cdot10^{-4}$
#2	$6{,}4\cdot10^{17}$	24000	$4{,}3\cdot10^{-4}$
#3	$9{,}7\cdot10^{17}$	22300	$2{,}7\cdot10^{-4}$
Thin film magnetic sensors			
#4	$3{,}0\cdot10^{18}$	10300	$2{,}1\cdot10^{-4}$
#5	$7{,}5\cdot10^{17}$	22000	$4{,}3\cdot10^{-4}$
#6	$3{,}4\cdot10^{17}$	24700	$7{,}4\cdot10^{-4}$

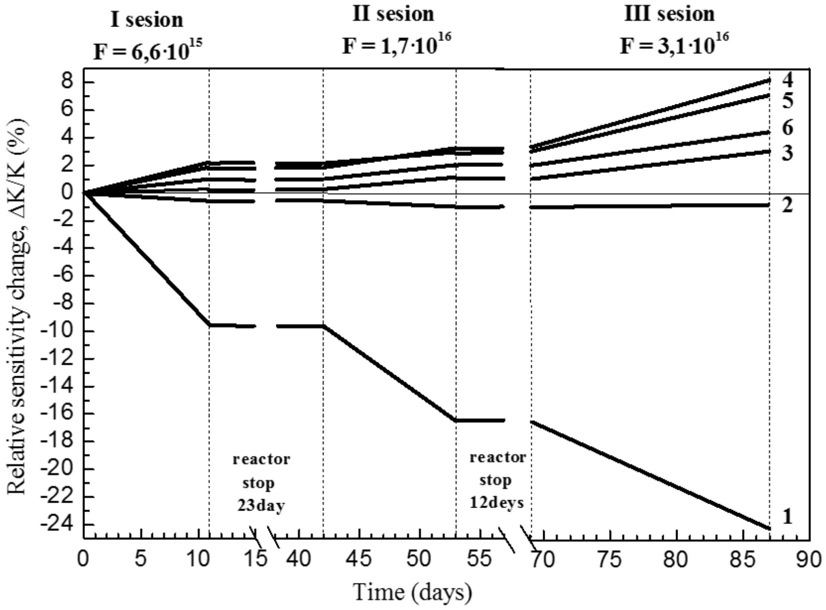

Fig. 4.23. Relative sensitivity dependence.

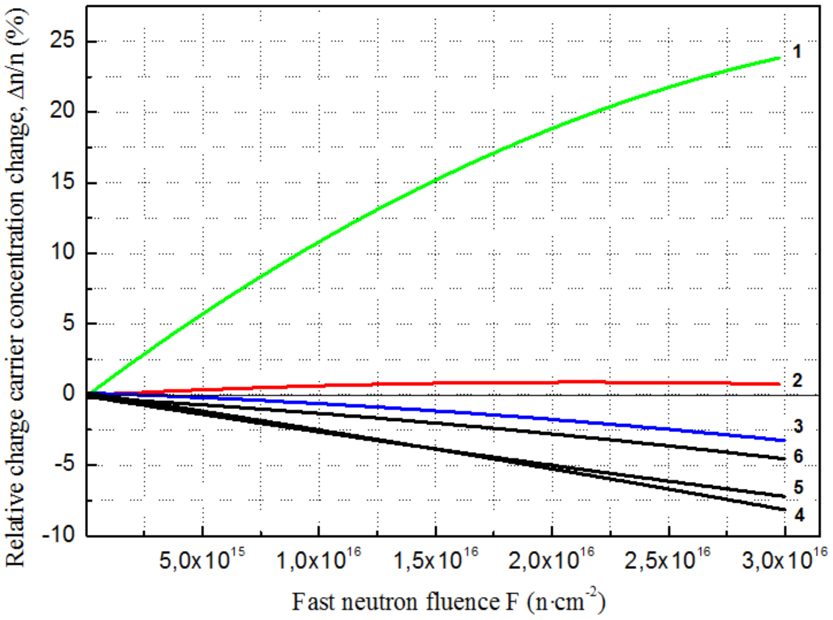

Fig. 4.24. Relative charge carrier concentration dependence.

The maximum value of concentration change of 24 % under irradiation with maximum dose can be seen in low-doped microcrystal sample #1 with an initial carrier concentration of $n_1 = 8{,}6\cdot10^{16}$ cm^{-3}. The concentration of electrons in it increases with the growth of neutron fluence, and for highly-doped microcrystal sample #3, $n_3 = 9{,}7\cdot10^{17}$ cm^{-3}, the charge carrier concentration decreases during the whole range of fluences. In all film #4, #5, #6 samples the carrier concentration decreases during the whole range of neutron fluences.

All the dependencies have the non-linear behavior, which means that the rate of concentration change does not remain constant during neutron fluence growth: in low compensated samples #1 and #2 the rate of concentration change decreases while the fluence grows, whereas in highly compensated samples #3, #4, #5 and #6 it increases. This means that under neutron irradiation both simultaneously running radiation processes – nuclear doping and introduction of radiation defects – have opposite signs in low compensated samples #1 and #2 and partially compensate each other. The increase in concentration occurs due to nuclear doping, which generates electrons in those samples and is a predominant process. The decreasing of the rate of this concentration increase is connected with the fact that the density of the introduced acceptor type radiation defects increases while fluence grows and partially compensates for the concentration of electrons generated by nuclear doping.

From the analysis of the measurement results, it follows that the most stable during the whole fluence interval is sensor #2 with initial carrier concentration $n_2 = 6{,}4 \cdot 10^{17}$ cm^{-3}. Up to the highest neutron fluence of $F = 3{,}1 \cdot 10^{16}$ n·m^{-2} the change in its sensitivity didn’t exceed 1 % compared to the initial value, and at the fluence of $F = 1 \cdot 10^{15}$ n·m^{-2} it amounts to only 0,05%. This proves the possibility of using such sensors in the above-mentioned measuring magnetic field instrumentations for high radiation conditions.

4.7. Summary for Chapter 4

A set of magnetic field measuring instrumentation on Hall sensors for harsh radiation conditions is described. It includes RHP-ISC and RHP-WB instrumentations for plasma magnetic field monitoring in nuclear fusion reactors, RHP-MAP instrumentation for permanent cyclotron magnet magnetic field high-precision mapping in charge particle accelerators, and RHP-RAD instrumentation for investigating sensors directly during their irradiation in nuclear reactors.

RHP-ISC instrumentation is based on radiation-stable 3D probes and an in-situ calibration technique. Each 3D probe contains 3 Hall sensors and 3 coils. The Hall sensors generate output voltages V_{HGX}, V_{HGY}, and V_{HGZ}, which are proportional to the corresponding magnetic field induction components B_X, B_Y, and B_Z. The coils perform two functions. In pick-up mode, they generate voltages V_{CLX}, V_{CLY}, and V_{CLZ}, which are proportional to the corresponding magnetic field induction change rate components ΔB_X, ΔB_Y, and ΔB_Z. In calibration mode, the coils generate test magnetic fields B_{0X}, B_{0Y}, and B_{0Z} of approximately 5 mT at supply current of about 20 mA. These test magnetic fields do not depend on the radiation dose, and thus they can be used for periodic determination of the Hall sensors' sensitivity.

Considerable electromagnetic noise on the outputs of Hall sensors and signal cables, which connect the sensors with signal processing circuits, set a restriction upon the frequency range of the Hall sensor devices. To solve this problem, a Hall sensor’s supply current switching technique at high frequency was applied in RHP-WB instrumentations. Its electronic unit generates and amplifies a set of signals by means of two-cycle synchronous detection. Subsequent analog-to-digital conversion of these signals at frequency f_{ADC} = 500 kHz makes the electromagnetic noise compensation possible, which in its turn provides accurate magnetic field measurement within the 0÷250 kHz frequency range.

The novelty of RHP-MAP instrumentation is based on the integration of an NMR probe and HG probes set into a complex measuring system that is calibrated directly in a cyclotron magnet. The first one provides very high measuring accuracy but NMR probes cannot operate in inhomogeneous magnetic fields. The second approach using Hall sensors does not have any limitations concerning the field homogeneity, but their measurement accuracy is rather low. The NMR probe is placed on a disk near one of the HG probes, and the area of the NMR probe should meet the requirements of high field homogeneity in the middle of one of the “hills” or “valleys” of the magnet. During the calibration using the NMR probe, accurate values of the field and output signal of the HG probe are measured. The disk is rotated during the calibration, which allows the alignment of all the HG probes of the mapper with the NMR-probe. During the mapping the HG probes are placed by the radius. RHP-MAP instrumentation provides the accuracy of magnetic field measuring ±0.01% at 48 HG probes set.

RHP-RAD instrumentation for investigating sensors directly during their irradiation in nuclear reactors is based on the test magnetic field technique and signal synchronous detecting with analog-to-digital conversion on 24-bit microconverter. It provides measurement irrepeatability of ±0.1 % at test magnetic field $\Delta B = 5$ mT.

Using RHP-RAD instrumentation Hall sensors relative sensitivity and charge carrier concentration dependencies have been studied directly during their irradiation. It was shown that the most stable is the Hall sensor with initial carrier concentration $n = 6{,}4 \cdot 10^{17}$ cm^{-3}. Up to the neutron fluence of $F = 3{,}1 \cdot 10^{16}$ n·m^{-2} the change in its sensitivity didn’t exceed 1 % and at fluence of $F = 1 \cdot 10^{15}$ n·m^{-2} it amounts to only 0,05%. This proves the possibility of using such sensors in measuring magnetic field instrumentations for high radiation conditions.

References for Chapter 1

1. Heidari; H., Nabaei, V. (2020). Magnetic Sensors Based on Hall Effect. Heidari, H., Nabaei, V. Magnetic Sensors for Biomedical Applications (pp.33-56). IEEE 2020. https://doi.org/10.1002/9781119552215.ch2.
2. Brauer, John R. (2014) Hall Effect and Magnetoresistive Sensors. Brauer, John R. Magnetic Actuators and Sensors (pp.175-199). IEEE 2014. https://doi.org/10.1002/9781118779262.ch10.
3. Avdochenko, B. I., Karlova, G. F., Yurchenko, V. I. (2016, October). Weak magnetic field detectors based on Hall-effect sensors. 2016 13th International Scientific-Technical Conference on Actual Problems of Electronics Instrument Engineering (APEIE), 91-93. https://doi.org/10.1109/APEIE.2016.7802219.
4. Parmar, M. M., Saren, H., Das, P. (2020, November). Fabrication and Characterization of InAs/AlSb based Magnetic Hall Sensors. 2020 5th IEEE International Conference on Emerging Electronics (ICEE), 1-4. https://doi.org/10.1109/ICEE50728.2020.9776959.
5. Ferhi, O., Sandner, M., Rohrmann, K., Meier, P., Prochaska, M. (2019). Field Modulation for Precise Weak Magnetic Field Measurement with a Hall-Plate. 2019 Kleinheubach Conference, 1-4.
6. Nicoloiu, A., Ciubotaru, F., Nastase, C., Dinescu, A., Iordanescu, S., Ahmad, H., … Müller, A. (2019, June). Room and Cryogenic Temperature Behaviour of Magnetic Sensors Based on Gan/Si Single Saw Resonators. 2019 20th International Conference on Solid-State Sensors, Actuators and Microsystems & Eurosensors XXXIII (TRANSDUCERS & EUROSENSORS XXXIII), 2037-2040. https://doi.org/10.1109/TRANSDUCERS.2019.8808415.
7. Kazakova, O., Gallop, J. C., See, P., Cox, D., Perkins, J. K., Moore, J.D., Cohen, L.F., Detection of a Micron-Sized Magnetic Particle Using InSb Hall Sensor. IEEE Transactions on Magnetics, 45(10), 4499-4502. https://doi.org/10.1109/TMAG.2009.2025513.
8. Mihajlovic, G., Xiong, P., von Molnar, S., Field, M., Sullivan, G. J., Ohtani, K. (2007). Submicrometer Hall Sensors for Superparamagnetic Nanoparticle Detection. IEEE Transactions on Magnetics, 43(6), 2400-2402. https://doi.org/10.1109/TMAG.2007.893123.
9. Togawa, K., Sanbonsugi, H., Lapicki, A., Abe, M., Handa, H., Sandhu, A. (2005). High-sensitivity InSb thin-film micro-Hall sensor arrays for simultaneous multiple detection of

magnetic beads for biomedical applications. IEEE Transactions on Magnetics, 41(10), 3661-3663. https://doi.org/10.1109/TMAG.2005.854789.

10. Haned and, N., Missous, M. (2002, November). Low magnetic field mapping using an InGaAs-AlGaAs-GaAs 2 DEG Hall sensor. The 10th IEEE International Symposium on Electron Devices for Microwave and Optoelectronic Applications, 231-236. https://doi.org/10.1109/EDMO.2002.1174963.
11. Partin, D. L., Heremans, J. P., Schroeder, T., Thrush, C. M., Flores-Mena, L. A. (2006). Temperature stable Hall effect sensors. IEEE Sensors Journal, 6(1), 106-110. https://doi.org/10.1109/JSEN.2005.860362.
12. Abderrahmane, A., Koide, S., Sato, S., Ohshima, T., Sandhu, A., Okada, H. (2012). Robust Hall Effect Magnetic Field Sensors for Operation at High Temperatures and in Harsh Radiation Environments. IEEE Transactions on Magnetics, 48(11), 4421-4423. https://doi.org/10.1109/TMAG.2012.2196986.
13. Rafí, J. M., Pellegrini, G., Godignon, P., Ugobono, S. O., Rius, G., Tsunoda, I., … Moll, M. (2020). Electron, Neutron, and Proton Irradiation Effects on SiC Radiation Detectors. IEEE Transactions on Nuclear Science, 67(12), 2481-2489. https://doi.org/10.1109/TNS.2020.3029730.
14. Mizuta, E., Nakada, Y., Kuboyama, S., Inoue, M., Kumagai, Y., Tatemichi, S., … Shindou, H. (2018, September). Radiation Test Results in Newly Developed Super-Junction Power MOSFETs. 2018 18th European Conference on Radiation and Its Effects on Components and Systems (RADECS), 1-6. https://doi.org/10.1109/RADECS45761.2018.9328675.
15. Ahmad, D., Fauzi, N., Md Rashid, K. A., Mohamed Zin, M. R., Hasbullah, N. F. (2015). Neutron Radiation Effects on the Electrical Characteristics of InAs/GaAs Quantum Dot-in-a-Well Structures. IEEE Transactions on Nuclear Science, 62(6), 3324-3329. https://doi.org/10.1109/TNS.2015.2478450.
16. Ruddy, F. H., Siedel, J. G. (2006, October). Effects of Gamma Irradiation on Silicon Carbide Semiconductor Radiation Detectors. 2006 IEEE Nuclear Science Symposium Conference Record, 583-587. https://doi.org/10.1109/NSSMIC.2006.356223.
17. Berger, R. W., Brown, R., Doyle, S., Haddad, N., Kapcio, P., Rodgers, J., Wood, N. (2001, September). Radiation effects on high performance spaceborne electronics. RADE 2001 6th European Conference on Radiation and Its Effects on Components and Systems (Cat. No.01TH8605), 323-327. https://doi.org/10.1109/RADECS.2001.1159301.

18. Porumb, C. S., Aldosari, A. H., Fuduli, I., Cutajar, D., Newall, M., Metcalfe, P., … Petasecca, M. (2016). Characterisation of Silicon Diode Arrays for Dosimetry in External Beam Radiation Therapy. IEEE Transactions on Nuclear Science, 63(3), 1808-1817. https://doi.org/10.1109/TNS.2016.2567446.
19. Aniceto, R., Milanowski, R., Moro, S., Cahoy, K., Schlenvogt, G. (2017, October). Proton Radiation Effects on Hamamatsu InGaAs PIN Photodiodes. 2017 17th European Conference on Radiation and Its Effects on Components and Systems (RADECS), 1-6. https://doi.org/10.1109/RADECS.2017.8696239.
20. Lauenstein, J. -M., Casey, M. C., Ladbury, R. L., Kim, H. S., Phan, A. M., Topper, A. D. (2021, March). Space Radiation Effects on SiC Power Device Reliability. 2021 IEEE International Reliability Physics Symposium (IRPS), 1-8. https://doi.org/10.1109/IRPS46558.2021.9405180.
21. Miura-Mattausch, M., Kikuchihara, H., Baba, S., Navarro, D., Iizuka, T., Sakamoto, K., Mattausch, H. J. (2020, September). Compact Modeling of Radiation Effects in Thin-Layer SOI-MOSFETs. 2020 International Conference on Simulation of Semiconductor Processes and Devices (SISPAD), 319-322. https://doi.org/10.23919/SISPAD49475.2020.9241636.
22. Zhang, X., Zhang, Y., Gao, Y., Xue, J. (2019, May). Feasibility Analysis of Establishing a Physical Model of Radiation Effects from SiC to device. 2019 3rd International Conference on Radiation Effects of Electronic Devices (ICREED), 1-3. https://doi.org/10.1109/ICREED49760.2019.9205162.
23. Esquivias, I., Barbero, J., López, D., Fischer, M., Roessner, K., Koeth, J. (2011, september). Evaluation of the radiation hardness of GaSb-based laser diodes for space applications. 2011 12th European Conference on Radiation and Its Effects on Components and Systems, 349-352. https://doi.org/10.1109/RADECS.2011.6131411.
24. Metelkin, I. O., Elesin, V. V., Kuznetsov, A. G., Usachev, N. A. (2019, September). Investigation of transient radiation effects in GaAs field effect transistors under pulse ionization. 2019 19th European Conference on Radiation and Its Effects on Components and Systems (RADECS), 1-5. https://doi.org/10.1109/RADECS47380.2019.9745656.
25. Moscatelli, F., Passeri, D., Morozzi, A., Mattiazzo, S., Dalla Betta, G. F., Dragicevic, M., Bilei, G.M. (2016, September). Radiation damage effects on p-type silicon detectors for high-luminosity operations: Test and modeling. 2016 16th European Conference on Radiation and Its Effects on Components and Systems (RADECS), 1-4. https://doi.org/10.1109/RADECS.2016.8093111.

26. Vologdin, E. N., Pudovikov, F. S., Sidorov, D. V., Sinkevich, V. F., "Application of Isotope Radiation Sources for Radiation Effects Simulation in Semiconductor Devices. 2015 15th European Conference on Radiation and Its Effects on Components and Systems (RADECS), 1-3. https://doi.org/10.1109/RADECS.2015.7365587.
27. Datta, S., Chau, R. (2005, October). Silicon and III-V nanoelectronics. International Conference on Indium Phosphide and Related Materials, 7-8. https://doi.org/10.1109/ICIPRM.2005.1517405.
28. Wada, O. (2013, May). Advances in III–V semiconductor photonics: Nanostructures and integrated chips. 2013 International Conference on Indium Phosphide and Related Materials (IPRM), 1-2. https://doi.org/10.1109/ICIPRM.2013.6562561.
29. Ohno, H. (2002, September). Molecular beam epitaxy and properties of ferromagnetic III-V semiconductors. International Conference on Molecular Bean Epitaxy, 9-10. https://doi.org/10.1109/MBE.2002.1037734.
30. Xu, B., Wang, Z. G., Chen, Y. H., Jin, P, Ye, X. L., Liu, H. Y., …, Liu, F. Q. (2004, September). Controlled growth of III-V compound semiconductor nano-structures and their application in quantum-devices. 13th International Conference on Semiconducting and Insulating Materials, 2004. SIMC-XIII-2004., 113-118. https://doi.org/10.1109/SIM.2005.1511398.
31. Bolshakova, I., Vasyliev, O., Kost, Y., Kuech, T., Radishevskiy, M., Shurygin, F. (2017, May). InAs/i-GaAs nano-heterostructures behavior under neu-tron irradiation. XVI International Conference Physics and Technology of Thin Films and Nanosystems (ICPTTFN XVI) Materials of International Conference, 288.
32. Bolshakova, I., Kost, Y., Shurygin, F., & Vasyliev, O. (2016, February). Sensor systems for magnetic diagnostics of fusion reactors and accelerators. 2016 13th International Conference on Modern Problems of Radio Engineering, Telecommunications and Computer Science (TCSET), 422-426. doi:10.1109/tcset.2016.7452076.
33. Bolshakova, I., Ďuran, I., Ya, K., Kovaljova, N., Kovarik, K., Makido, Viererbl, L. (2013). Effect of neutron irradiation on indium-containing III-V semiconductor micromonocrystals. Key Eng. Mater, 354, 543:273–276. https://doi.org/10.4028/www.scientific.net/KEM.543.273.
34. Bolshakova, I. A., Boiko, V. M., Brudnyi, V. N., Kamenskaya, I. V., Kolin, N. G., Makido, E. Y., Moskovets, T. A., Merkurisov, D. I. (2005). The effect of neutron irradiation on the properties of n-InSb whisker microcrystals. Semiconductors 39(7), 780–785. https://doi.org/10.1134/1.1992633.

35. Kovařнk, K., Ďuran, I., Sentkerestiov, J., Oszwaldowski, M., Viererbl, L., Boshakova, I., Holyaka, R., Erashok, V. (2012). Status of development of high temperature radiation hardened Hall sensors for energy producing fusion devices. WDS'12 Proceedings of Contributed Papers, Part II, 216–221.

References for Chapter 2

1. Hadjigeorgiou, N., Asimakopoulos, K., Papafotis, K., Sotiriadis, P. P. (2021). Vector Magnetic Field Sensors: Operating Principles, Calibration and Applications. IEEE Sensors Journal, 21(11), 12531-12544. https://doi.org/10.1109/JSEN.2020.3045660.
2. Quandt, E., Stein, S., Wuttig, M. (2005, October). Magnetic vector field sensor using magnetoelectric thin film composites. IEEE International Magnetics Conference (INTERMAG), 967-968. https://doi.org/10.1109/INTMAG.2005.1463912.
3. Zhao, X., Bai, Y., Deng, Q., Ai, C., Yang, X., Wen, D. (2017). Research of the Monolithic Integrated 3-D Magnetic Field Sensor Based on MEMS Technology. IEEE Sensors Journal, 17(18), 5849-5856, https://doi.org/10.1109/JSEN.2017.2736639.
4. Pan, H., Yao, L., He, S., Li, W., Li, L., Sha, J. (2014, June). Single-Chip Integrated 3-D Hall Sensor. Third International Conference on Instrumentation, Measurement, Computer, Communication and Control, Shenyang, 252-255, https://doi.org/10.1109/IMCCC.2013.60.
5. Lozanova, S. V., Ivanov A. J., Roumenin, C. S. (2019, October). Three-dimensional Field Sensing with Magnetotransistors. IEEE XXVIII International Scientific Conference Electronics (ET), 1-4, https://doi.org/10.1109/ET.2019.8878505.
6. Leepattarapongpan, C., Phetchakul, T., Penpondee, N., Pengpad, P., Srihapat, A., Chaowicharat, E., Hruanun, C., Poyai, A. (2011, October). The low power 3-D-magnetotransistor based on CMOS technology, SENSORS. IEEE, 500-503, https://doi.org/10.1109/ICSENS.2011.6127079.
7. Beran, P., Klöhn, M., Hohe, H. (2019). Measurement Characteristics of Different Integrated Three-Dimensional Magnetic Field Sensors. IEEE Magnetics Letters, 10, 1-5, https://doi.org/10.1109/LMAG.2019.2944581.
8. Luong, V. S. (2017). Planarization, Fabrication, and Characterization of Three-Dimensional Magnetic Field Sensors. IEEE Transactions on Nanotechnology, 17(1), 11-25. https://doi.org/10.1109/TNANO.2017.2660062.

9. Guo, C., Zhang, H., Guo, H., Chen, L., Chen, W., Yu, N. (2021). Crosstalk Analysis and Current Measurement Correction in Circular 3-D Magnetic Sensors Arrays. IEEE Sensors Journal, 21(3), 3121-3133. https://doi.org/10.1109/JSEN.2020.3028149.
10. Beran, P., Stahl-Offergeld, M., Peters, V., Krause, D., Hohe, H. (2019). Impact of Contact Misalignment on Magnetic Cross Sensitivity of Integrated Vertical Hall Sensors. IEEE Transactions on Magnetics, 55(1), 1-4. https://doi.org/10.1109/TMAG.2018.2873238.
11. Boyko, O., Holyaka, R., Hotra, Z. (2018, February). Functionally integrated sensors on magnetic and thermal methods combination basis. 2018 14th International Conference on Advanced Trends in Radioelecrtronics, Telecommunications and Computer Engineering (TCSET), 697-701. https://doi.org/10.1109/TCSET.2018.8336296.
12. Dwivedi, A., Ramakrishnan, A., Reddy, A., Patel, K. Ozel, S., Onal, C. D. (2018). Design, Modeling, and Validation of a Soft Magnetic 3-D Force Sensor. IEEE Sensors Journal, 18(9), 3852-3863. https://doi.org/10.1109/JSEN.2018.2814839.
13. Ettelt, D., Rey, P., Jourdan, G., Walther, A., Robert, P., Delamare, J. (2014). 3-D Magnetic Field Sensor Concept for Use in Inertial Measurement Units (IMUs). Journal of Microelectromechanical Systems, 23(2), 324-333. https://doi.org/10.1109/JMEMS.2013.2273362.
14. Ortner, M., Huber, C., Vollert, N., Pilz, J., Süss, D. (2017, October) Application of 3-D-printed magnets for magnetic position detection systems. 2017 IEEE SENSORS, Glasgow, UK, 1-3. https://doi.org/10.1109/ICSENS.2017.8233930.
15. Fedasyuk, D., Holyaka, R., Marusenkova, T. (2020, February). Signal Chain of Programmable System on Chip for Magnetic Tracking Sensors. 2020 IEEE 15th International Conference on Advanced Trends in Radioelectronics, Telecommunications and Computer Engineering (TCSET), 46-49, https://doi.org/10.1109/TCSET49122.2020.235387.
16. Holyaka, R., Prudyus, I., Barylo, G., Marusenkova, T., Fabirovskyy, S. (2019, September). RETwix: Labs Instrumentation For Science And Education. 2019 International Conference on Information and Telecommunication Technologies and Radio Electronics (UkrMiCo), 1-4. https://doi.org/10.1109/UkrMiCo47782.2019.9165386.
17. Kogut, I., Druzhinin, A., Holota, V. (2011) 3-D SOI Elements for System-on-Chip Applications. Advanced Materials Research, 276, 137–144, 2011, https://doi.org/10.4028/www.scientific.net/amr.276.137.
18. Kogut, I., Holota, V., Druzhinin, A., Dovhij, V. (2016). The Device-Technological Simulation of Local 3-D SOI-Structures. Journal of Nano Research, 39, 228-234. https://doi.org/10.4028/www.scientific.net/JNanoR.39.228.

19. Nazari Nejad, S., Mansour, R. (2016). A 3-D Finite-Element Analysis of Giant Magnetoimpedance Thin-Film Magnetic Sensors. IEEE Transactions on Magnetics, 52(1), 1-8. https://doi.org/10.1109/TMAG.2015.2476489.
20. Meier, P., Rohrmann, K., Sandner, M., Prochaska, M. (2019, August). A numerical methodology for a 6 DOF pose estimation with 3-D magnetic field sensors. 2019 IEEE 62nd International Midwest Symposium on Circuits and Systems (MWSCAS), 1005-1008, https://doi.org/10.1109/MWSCAS.2019.8885265.
21. Hotra, Z., Holyaka, R., Bolshakova, I., Yurchak, I., Marusenkova, T. (2011). Spatial models of splitted Hall structures. Perspective Technologies and Methods in MEMS Design, 5-8.
22. Hotra, Z., Holyaka, R., Bolshakova, I., Yurchak, I., Marusenkova, T. (2011). Arbitrary rotation method for 3-D magnetic sensors calibration. 2011 11th International Conference The Experience of Designing and Application of CAD Systems in Microelectronics (CADSM), 413-416.
23. Barylo, G. I., Holyka, R. L., Helzhynskyi, I. I., Hotra, Z. Y., Ivakh, M. S., Politanskyi, R. L. (2020). Modeling of organic light emitting structures. Physics and Chemistry of Solid State, 21(3), 519-524. https://doi.org/10.15330/pcss.21.3.519-524.
24. Aziz, A., Ghosh, S., Datta, S., Gupta, S. K. (2016). Physics-Based Circuit-Compatible SPICE Model for Ferroelectric Transistors. IEEE Electron Device Letters, 37(6), 805-808. https://doi.org/10.1109/LED.2016.2558149.
25. Moumouni, Y., Jacob Baker, R. (2015, August). Improved SPICE modeling and analysis of a thermoelectric module. 2015 IEEE 58th International Midwest Symposium on Circuits and Systems (MWSCAS), 1-4. https://doi.org/10.1109/MWSCAS.2015.7282015.
26. Crescentini, M., Romani, A., Sangiorgi, E. (2014, April). Physical simulations of response time in Hall sensor devices. 2014 15th International Conference on Ultimate Integration on Silicon (ULIS), 89-92. https://doi.org/10.1109/ULIS.2014.6813923.
27. Rossini, A., Borghetti, F., Malcovati, P., Maloberti, F. (2005, December). Behavioral model of magnetic sensors for SPICE simulations. 2005 12th IEEE International Conference on Electronics, Circuits and Systems, 1-4. https://doi.org/10.1109/ICECS.2005.4633482.
28. Sung, G., Wang, W., Yu, C. (2017). Analysis and Modeling of One-Dimensional Folded Vertical Hall Sensor With Readout Circuit. IEEE Sensors Journal, 17(21), 6880-6887. https://doi.org/10.1109/JSEN.2017.2754295.

29. Holyaka, R, Tetyana, M. (2018) Split Hall Structures: Parametric Analysis and Data Processing. LAP Lambert Academic Publishing – 2018, 124, ISBN-13: 978-3-659-86243-4. Retrieved from https://www.amazon.co.uk/Split-Hall-Structures-Parametric-Processing/dp/3659862436.
30. Holyaka, R., Hotra, Z., Weglarski, M., Marusenkova, T. (2012). Field characteristic of magnetic sensors on the splitted hall structures. Electronika, 5, 50 – 55.
31. Bolshakova, I., Holyaka. R. (2006). Magnetic field measuring sensor. Patent application WO200602842. Retrieved from https://patentscope.wipo.int/search/en/detail.jsf?docId=WO2006028426.

References for Chapter 3

1. Heymann, P., Matthias, R. (2021). Measurement Accuracy and Sources of Error. Heymann, P., Matthias, R. A Guide to Noise in Microwave Circuits: Devices, Circuits, and Measurement (pp. 345-357). IEEE, 2022. https://doi.org/10.1002/9781119859390.ch19.
2. Rumiantsev, A. (2019). 9 Selected Aspects of Measurement and Calibration Assurance. Rumiantsev, A. On-Wafer Calibration Techniques Enabling Accurate Characterization of High-Performance Silicon Devices at the mm-Wave Range and Beyond (pp.119-130). River Publishers, 2019.
3. Rumiantsev, A., (2019). 7 Advantages of in-situ Calibration. Rumiantsev, A. On-Wafer Calibration Techniques Enabling Accurate Characterization of High-Performance Silicon Devices at the mm-Wave Range and Beyond (pp.97-108). River Publishers, 2019.
4. Nadig, S., Pinrod, V., Ardanuç, S., Lal, A. (2015, March) Multi-modal mechanical stimuli stage for in-situ calibration of MEMS gyroscopes. 2015 IEEE International Symposium on Inertial Sensors and Systems (ISISS) Proceedings, 1-2. https://doi.org/10.1109/ISISS.2015.7102393.
5. Tan, C., Ding, K., Yang, W., Seyfried, W. E. (2016, April). Accurate pH measurement and determination in deep-sea environments by an in-situ pH sensor calibration device. OCEANS 2016 - Shanghai, 1-5. https://doi.org/10.1109/OCEANSAP.2016.7485352.
6. Hanatani, K., Fujii, T., Fukuba, T. (2015, February). Development of in situ microbial ATP analyzer and internal standard calibration method. 2015 IEEE Underwater Technology (UT), 1-4. https://doi.org/10.1109/UT.2015.7108276.

7. Nadeau, A., Dinesh, K., Sharma, G. Xiong, M. (2017, March). In-situ calibration of accelerometers in body-worn sensors using quiescent gravity. 2017 IEEE International Conference on Acoustics, Speech and Signal Processing (ICASSP), 2192-2196. https://doi.org/10.1109/ICASSP.2017.7952545.
8. Ni, B., Zhao, J., Li, H., Su, Y., Luo, X., Wu, H. (2018, August). Research on in-Situ Calibration Technology of Six-dimension Force Sensor for the LIDM Docking Performance Test-bed. 2018 IEEE International Conference on Mechatronics and Automation (ICMA), 1366-1370. https://doi.org/10.1109/ICMA.2018.8484598.
9. Nguyen, T., Tam, A., Oelze, M. L. (2018, October). In Situ Calibration to Account for Transmission Losses in Backscatter Coefficient Estimation. 2018 IEEE International Ultrasonics Symposium (IUS), 1-4. https://doi.org/10.1109/ULTSYM.2018.8580156.
10. Lagerloef, G., Carey, D., Kao, H. (2018, March). Verifying Aquarius Radiometer Calibration Drift Using in Situ Data. 2018 IEEE 15th Specialist Meeting on Microwave Radiometry and Remote Sensing of the Environment (MicroRad), 1-4. https://doi.org/10.1109/MICRORAD.2018.8430700.
11. Mitishita, E. A., Martins, M., Costa, F. A. L., Centeno, J. (2017, July). Improvements in the integration of lidar and photogrammetric datasets by in situ camera calibration. 2017 IEEE International Geoscience and Remote Sensing Symposium (IGARSS), 3023-3026. https://doi.org/10.1109/IGARSS.2017.8127635.
12. Yu, R., Proietti, R., Kurumida, J., Karalar, A., Guan, B., Yoo, S. J. B. (2011). Rapid automatic high-precision in-situ wavelength calibration for tunable lasers using an athermal AWG. CLEO: 2011 - Laser Science to Photonic Applications, 1-2.
13. Chen, M., Chen, C. (2013). Improved Permittivity Calibration Method for Wideband In Situ Permittivity Probe. IEEE Geoscience and Remote Sensing Letters, 10(2), 323-327. https://doi.org/10.1109/LGRS.2012.2205366.
14. Dillonб J., Steele, S. -M. (2020, October). In Situ Array Calibration for Synthetic Aperture Sonar. Global Oceans 2020: Singapore – U.S. Gulf Coast, 1-5, https://doi.org/10.1109/IEEECONF38699.2020.9389233.
15. (Anonymous, 2004). American National Standard Calibration of Germanium Detectors for In-Situ Gamma-Ray Measurements. ANSI N42.28-2002, 1-60. https://doi.org/10.1109/IEEESTD.2004.94433.
16. Saha, A. K., Sridhar, S. (2012, August). In-situ Cross Calibration of In-Core Thermocouples in Fast Breeder Test Reactor. 2012 International Conference on Advances in Computing and Communications, 247-250. https://doi.org/10.1109/ICACC.2012.56.

17. Wang, Z., Zhang, F., Gao, H., Franek, O., Pedersen, G. F., Fan, W. (2021). Over-the-Air Array Calibration of mmWave Phased Array in Beam-Steering Mode Based on Measured Complex Signals. IEEE Transactions on Antennas and Propagation, 69(11), 7876-7888. https://doi.org/10.1109/TAP.2021.3076349.
18. Bronselaer, A., Van Britsom, D., De Tré, G. (2015). Propagation of Data Fusion. IEEE Transactions on knowledge and data engineering, 27(5), 1330 – 1342. http://dx.doi.org/10.1109/TKDE.2014.2365807.
19. Fisseler, J., Fehér, I. (2010). Data fusion with probabilistic conditional logic. Logic Journal of the IGPL, 18(4), 488 – 507. https://doi.org/10.1093/jigpal/jzp035.
20. Liu, K., Huang, S. (2016). Integration of data fusion methodology and degradation modeling process to improve prognostics. IEEE Transactions on Automation Science and Engineering, 13(1), 344 – 354. https://doi.org/10.1109/TASE.2014.2349733.
21. Alam, F., Mehmood, R., Katib, I., Nasser, N., Albogami, A. A. (2017). Data fusion and IOT for smart ubiquitous environments: a survey. IEEE Access, 5, 9533 – 9554. https://doi.org/10.1109/ACCESS.2017.2697839.
22. Zhao, J., Gao, Y., Qu, Y., Yin, H., Liu, Y., Sun, S. (2018). Travel time prediction: based on gated recurrent unit method and data fusion. IEEE Access, 6, 70463 – 70472. https://doi.org/10.1109/ACCESS.2018.2878799.
23. Adali, T., Levin-Schwartz , Y., Calhoun, V. D. (2015). Multimodal data fusion using source separation: application to medical imaging. Proceedings of the IEEE, 103(9), 1494 – 1506. http://dx.doi.org/10.1109/JPROC.2015.2413993
24. Fazli, s., Dähne, S., Samek, W., Bießmann, F., Müller, K-R. (2015). Learning from more than one data source: data fusion techniques for sensorimotor rhythm-based brain computer interfaces. Proceedings of the IEEE, 103(6), 891 – 906.
25. Liu, Z., Zhang, W., Lin, S., Quek, T. Q. S. (2017). Heterogeneous sensor data fusion by deep multimodal encoding. IEEE Journal of Selected Topics in Signal Processing, 11(3), 479 – 491. https://doi.org/10.1109/JSTSP.2017.2679538.
26. Gao, S., Zhong, Y., Li, W. (2011). Random weighting method for multisensor data fusion. IEEE Sensors Journal, 11(9), 1955 – 1961. https://doi.org/10.1109/JSEN.2011.2107896.
27. Kumar, M., Devendra, P., G., Randy A. Z. (2007). A method for judicious fusion of inconsistent multiple sensor data. IEEE Sensors Journal, 7(5), 723 – 733. https://doi.org/10.1109/JSEN.2007.894905.
28. Tsai, P.-H., Lin, Y-J., Ou, Y.-Z., Edward, T.-H., Chu, J. W., Liu, S. (2014). A framework for fusion of human sensor and physical sensor data. IEEE Transactions on Systems, Man,

and Cybernetics: Systems, 44(9), 1248 – 1261. https://doi.org/10.1109/TSMC.2014.2309090.

29. Grejner-Brzezinska, D. A., Toth, C. K., Moore, T., Raquet, J. F., Miller, M. M., Kealy, A. (2016), Multisensor navigation systems: a remedy for GNSS vulnerabilities. Proceedings of the IEEE, 104(6), 1339 – 1353. https://doi.org/10.1109/JPROC.2016.2528538.
30. Wang, Y., Cang, S., Yu, H. (2018). A data fusion-based hybrid sensory system for older people's daily activity and daily routine recognition. IEEE Sensors Journal, 18(16), 6874 – 6888. http://dx.doi.org/10.1109/JSEN.2018.2833745.
31. Barni, S., Fort, A., Becatti, M., Fiorillo, C., Mugnaini, M., Vignoli, V., … Novembre, E. (2017), Detection of allergen-ige interaction in allergic children through combined impedance and ros measurements. IEEE Transactions on Instrumentation and Measurement, 66(4), 616 – 623. https://doi.org/10.1109/TIM.2016.2640478.
32. Chen, Z., Zhou, S., Jiang, A. (2011, August). Miniaturization design on magnetic induction sensors. Proceedings of 2011 International Conference on Electronic & Mechanical Engineering and Information Technology, 4626-4629. https://doi.org/10.1109/EMEIT.2011.6024006.
33. Xie, S., Zhang, Y., Jin, M., Li, C., Meng, Q. (2021). High Sensitivity and Wide Range Soft Magnetic Tactile Sensor Based on Electromagnetic Induction. IEEE Sensors Journal, 21(3), 2757-2766. https://doi.org/10.1109/JSEN.2020.3025830.
34. Scott, W. R. (2020, October). Differential Electromagnetic Induction Sensor using a Spinning Magnet Excitation. IGARSS 2020 - 2020 IEEE International Geoscience and Remote Sensing Symposium, 1401-1404. https://doi.org/10.1109/IGARSS39084.2020.9323935.
35. Sriratana, W., Khwankityotha, Y., Satthamsakul, S. (2018, October). Development of Compatible Induction coil with Pure AC for Hall Effect Sensor: A Study on Metal Materials Thickness. 2018 18th International Conference on Control, Automation and Systems (ICCAS), 575-579.
36. Ambruš, D., Šimić, M., Vasić, D., Bilas, V. (2021). Close-Range Electromagnetic Tracking of Pulse Induction Search Coils for Subsurface Sensing. IEEE Transactions on Instrumentation and Measurement, 70, 1-13, 2021, Art no. 9505613, https://doi.org/10.1109/TIM.2021.3054011.
37. Bolshakova, I.; Quercia, A.; Coccorese, V.; Murari, A.; Holyaka, R.; Duran, I.; Viererbl, L.; Konopleva, R.; Yerashok, V. (2012). Magnetic Measuring Instrumentation with Radia-

tion-Resistant Hall Sensors for Fusion Reactors: Experience of Testing at JET. JET Preprints and Reports – EFDA–JET–PR, (11)54. Retrieved from http://www.iop.org/Jet/fulltext/EFDP11054.pdf.

38. Biel, W., Albanese, R., Ambrosino, R., Ariola, M., Berkel, M. V., Bolshakova, I., Zohm, H. (2019). Diagnostics for plasma control – From ITER to DEMO. Fusion Engi-neering and Design, 146(Part A), 465—472. https://doi.org/10.1016/j.fusengdes.2018.12.092.
39. Bolshakova, I., Holyaka, R. (2013). Method for measuring magnetic field (European patent EP2630511). https://register.epo.org/application?number= EP10858732&lng=en&tab=main.
40. Bolshakova, I., Holyaka, R. (2006). Capteur de mesure de champ magnetique (International patent application WO2006028427A1). https://patents.google.com/patent/WO2006028427A1/ru.

References for Chapter 4

1. Fiorentin, P., Pomaro, N. (2000, May). Comparison of two different techniques for long term magnetic measurements in nuclear fusion research. Proceedings of the 17th IEEE Instrumentation and Measurement Technology Conference [Cat. No. 00CH37066], 493-496. https://doi.org/10.1109/IMTC.2000.846914
2. Chiariello, A. G., Formisano, A., Martone, R. (2018, March). Approaches for magnetic sources reconstruction in controlled thermo-nuclear fusion technology. 2018 International Applied Computational Electromagnetics Society Symposium (ACES), 1-3. https://doi.org/10.23919/ROPACES.2018.8364170.
3. Pais, S. C. (2011). The Plasma Compression Fusion Device—Enabling Nuclear Fusion Ignition. IEEE Transactions on Plasma Science, 47(11), 5119-5124. https://doi.org/10.1109/TPS.2019.2942997.
4. Wang, T., Ueda, H., Agatsuma, K., Ishiyama, A. (2011). Evaluation of Positional Stability in Active Magnetic Levitation Using Spherical HTS Bulk for Inertial Nuclear Fusion. IEEE Transactions on Applied Superconductivity, 21(3), 1579-1583. https://doi.org/10.1109/TASC.2010.2098383.
5. Chiariello, A. G., Ledda, F., Martone, R., Pizzo, F. (2016, November). Fast identification problems in 3D iron core fusion devices. 2016 IEEE Conference on Electromagnetic Field Computation (CEFC), 1-1, https://doi.org/10.1109/CEFC.2016.7816339.

6. De Tommasi, G., Alves, D, Bellizio, T., Felton, R., Neto, A., Sartori, F., … Lomas, P. (2011). Real-Time Systems in Tokamak Devices. A Case Study: The JET Tokamak. IEEE Transactions on Nuclear Science, 58(4), 1420-1426. https://doi.org/10.1109/TNS.2011.2147332.
7. Alves, D., Coelho, R., Neto, A. C., Smith, P., Valcarcel, D. F., Card, P., … McCullen, P. (2015). A Flexible System for the Control of External Magnetic Perturbations in the JET Tokamak. IEEE Transactions on Plasma Science, 43(2), 650-664. https://doi.org/10.1109/TPS.2015.2388674.
8. Albanese, R., Rubinacci, G., Villone, F. (2004). "Electromagnetic analysis of the 3-D effects of the metallic structures in JET tokamak. IEEE Transactions on Magnetics, 40(2), 589-592. https://doi.org/10.1109/TMAG.2004.824558.
9. Entler, S., Kocan, M., Duran, I., Vayakis, G., Lucca, F., Vigano, F., Cantu, R. (2018). Recent Improvement of the Design of the ITER Steady-State Magnetic Sensors. IEEE Transactions on Plasma Science, 46(5), 1276-1280. https://doi.org/10.1109/TPS.2018.2795243.
10. Peruzzo, S., Brombin, M., Palumbo, M. F., Gonzalez, W., Marconato, N., Rizzolo, A., … Lahodová, Z. (2016). Progress in the Design and Testing of In-Vessel Magnetic Pickup Coils for ITER. IEEE Transactions on Plasma Science, 44(9), 1704-1710. https://doi.org/10.1109/TPS.2016.2580380.
11. Zabeo, L., Ambrosino, G., Cavinato, M., Gribov, Y., Humphreys, D., Snipes, J. A., … Vayakis, G. (2012, June). Axisymmetric magnetic control in ITER. 2012 18th IEEE-NPSS Real Time Conference, 1-7. https://doi.org/10.1109/RTC.2012.6418098.
12. Huang, L., Lee, S. (2016). Study on Magnetic Field Mapping Method in the Center Volume of the Air-Core Solenoid. IEEE Transactions on Applied Superconductivity, 26(4), 1-4. https://doi.org/10.1109/TASC.2015.2512238.
13. Nam, J., Lee, W., Jung, E., Jang, G. (2018). Magnetic Navigation System Utilizing a Closed Magnetic Circuit to Maximize Magnetic Field and a Mapping Method to Precisely Control Magnetic Field in Real Time. IEEE Transactions on Industrial Electronics, 65(7), 5673-5681. https://doi.org/10.1109/TIE.2017.2782220.
14. Alves, H., Carvalho, D., Pereira, T., Fernandes, H. (2017, June). Design and instrumentation of a magnetic field micro-probe mapper: An e-lab aparatus to map a coil's magnetic field. 2017 4th Experiment@International Conference (exp.at'17), 113-114. https://doi.org/10.1109/EXPAT.2017.7984379.

15. Ahn, M. C., Hahn, S., Lee, H. (2013) 3-D Field Mapping and Active Shimming of a Screening-Current-Induced Field in an HTS Coil Using Harmonic Analysis for High-Resolution NMR Magnets. IEEE Transactions on Applied Superconductivity, 23(3), 4400804-4400804. https://doi.org/10.1109/TASC.2012.2237491.
16. Wu, Z., Ding, K., Feng, C., Song, Y. (2020, October). Radial Magnetic Field Optimization of the 5 T Superconducting Cyclotron for Medical Application. 2020 IEEE International Conference on Applied Superconductivity and Electromagnetic Devices (ASEMD), 1-2. https://doi.org/10.1109/ASEMD49065.2020.9276125.
17. Wu, Z., Ding, K., Song, Y., Li, J., Jiang, F., Ge, J. (2021). Magnetic Field Optimization and Tolerance Study of a Medical Superconducting Cyclotron. IEEE Transactions on Applied Superconductivity, 31(8), 1-4. https://doi.org/10.1109/TASC.2021.3101763.
18. Yao, Q. G., Ma, L. Z., Hao, H. F., Zhang, X. Y., Han, S. F., Wang, B, Yuan, P. (2012). The Magnetic Field Design of HITFiL Cyclotron. IEEE Transactions on Applied Superconductivity, 22(3), 4401004-4401004. https://doi.org/10.1109/TASC.2011.2175190.
19. Barrett, T. R., Carrelli, C., Grant, T., Kovari, M., Mantel, N., Muir, A., Surrey, E. (2020). A New Facility for Combined-Load Testing of Fusion Reactor In-Vessel Components. IEEE Transactions on Plasma Science, 48(6), 1432-1438. https://doi.org/10.1109/TPS.2020.2968405.
20. Zhang, X., Gao, Y., Zhang, Y., Xue, J. (2021, May). Construction of an in-situ radiation test system for semiconductor materials and devices based on a 4.5 MV accelerator. 2021 4th International Conference on Radiation Effects of Electronic Devices (ICREED), 1-5. https://doi.org/10.1109/ICREED52909.2021.9588711.
21. Fernandez, A. F., Brichard, B., Ooms, H., Berghmans, F. (2006). High-Vacuum Gamma Irradiation Facilities for Synergistic Effects Testing on Optoelectronic Components and Materials. IEEE Transactions on Nuclear Science, 53(6), 3726-3730. https://doi.org/10.1109/TNS.2006.884248.
22. Fernandez-Hernando, J. L., Blair, G. A., Boogert, S. T., Ellwood, G. E., Greenhalgh, J., Keller,L., Watson, N. K. (2007, June). Material damage test for ILC collimators. 2007 IEEE Particle Accelerator Conference (PAC), 2868-2870. https://doi.org/10.1109/PAC.2007.4440603.
23. Holyaka, R., Marusenkova, T., Fedasyuk, D. (2020). Signal model for spatial position sensors in magnetic tracking systems. Innovative Technologies and Scientific Solutions for Industries, 1 (11), 5–18. https://doi.org/10.30837/2522-9818.2020.11.005.

24. Barylo, G., Boyko, O., Gelzynskyy, I., Holyaka, R., Hotra, Z., Marusenkova, T., Khilchuk, M., Michalska, M. (2020). Hardware and software means for electronic components and sensors research, IAPGOŚ Informatyka, Automatyka, Pomiary W Gospodarce I Ochronie Środowiska, 10(1), 66-71. http://doi.org/10.35784/iapgos.1513.
25. Holyaka, R., Marusenkova, T., Fedasyuk, D. (2020). Measuring logarithmic signal converter for magnetic tracking systems, ISTCMTM. Measuring Equipment and Metrology, 81(1), 16-21. https://doi.org/10.23939/istcmtm2020.01.016.
26. Bolshakova, I., Quercia, A., Coccorese, V., Murari, A., Holyaka, R., Duran, I., … Yerashok, V. (2012). Magnetic Measuring Instrumentation With Radiation-Resistant Hall Sensors for Fusion Reactors: Experience of Testing at JET. IEEE Transactions on Nuclear Science, 59(4), 1224 – 1231. https://doi.org/10.1109/TNS.2012.2188816.
27. Bolshakova, I. (2016). Sensors for Magnetic Fields Measurement in High Level of Penetrating Radiation in Accelerators and New Generation Fusion Reactors. Nuclear Radiation Nanosensors and Nanosensory Systems, 19-32. https://doi.org/10.1007/978-94-017-7468-0_3.
28. Bolshakova, I., Belyaev, S., Bulavin, M., Brudnyi, V., Chekanov, V., Coccorese, V., Vinichenko, A. (2015). Experimental evaluation of stable long term operation of semiconductor magnetic sensors at ITER relevant environment. Nucl Fusion 55(8), 083006.
29. Bolshakova, I. A., Kulikov, S. A., Konopleva, R. F., Chekanov, V. A., Vasilevskii, I. S., Shurygin, F. M.,… Shtabalyuk, A. P. (2014). Application of reactor neutrons to the investigation of the radiation resistance of semiconductor materials of Group III-V and sensors. Physics of the Solid State, 56(1), 157-160. https://doi.org/10.1134/S1063783414010089
30. Bolshakova, I., Vasilevskii, I., Viererbl, L., Ďuran, I., Kovalyova, N., Kovarik, Shurygin, F. (2013). Prospects of using In-containing semiconductor materials in magnetic field sensors for thermonuclear reactor magnetic diagnostics. IEEE Trans Magn 49(1), 50–53. https://doi.org/10.1109/TMAG.2012.2217482.

SCIENTIFIC PUBLICATION

Inessa Bolshakova, Roman Holyaka, Tetyana Marusenkova, Fedir Shurygin

RADIATION-RESISTANT HALL MAGNETIC FIELD SENSORS AND INSTRUMENTATIONS

Monograph

Published (PDF): 14.09.2022. Signed for printing: 16.09.2022.
Format 60×84/16. Offset Paper. Digital printing.
The headset is Times New Roman. Conventionally printed sheets 8,60.
Circulation: 100 copies. Order № 332.

Printed from the finished original layout.

Publisher [ISBN]: Primedia eLaunch LLC
TX 75001, United States, Texas, Dallas
E-mail: info@primediaelaunch.com | URL: www.primediaelaunch.com

Publisher [printed copies]: NGO European Scientific Platform
21037, Ukraine, Vinnytsia, Zodchykh str. 18, office 81. E-mail: info@ukrlogos.in.ua
Certificate of the subject of the publishing business: ДК № 7172 of 21.10.2020.

9 798887 968025